The Role of Deformation and Microchemistry in the Corrosion Processes of Type 304 Stainless Steel in Simulated Pressurized Water Reactor Environments

by

Kevin B. Fisher

A dissertation submitted in partial fulfillment
of the requirements for the degree of
Doctor of Philosophy
(Materials Science and Engineering)
in the University of Michigan
2017

Doctoral Committee:

Associate Professor Emmanuelle Marquis, Chair
Assistant Professor Matthew Collette
Dr. Earl Johns, Naval Nuclear Laboratory
Professor J. Wayne Jones
Dr. Bryan Miller, Naval Nuclear Laboratory

Kevin B. Fisher
kbfisher@umich.edu
ORCID iD: 0000-0002-2742-2401

ACKNOWLEDGEMENTS

My success throughout this process would not have been possible without the support of a great many individuals. First and foremost, my advisor, Associate Professor Emmanuelle Marquis, has provided unparalleled support in the form of scientific and academic advising and development of my written and oral skills. For this I will be forever grateful, as it has made me into the person and researcher I am today.

My advisors and mentors at Bettis Atomic Power Laboratory, Dr. Earl Johns, Dr. Bryan Miller, and Dr. Tom Webb, who convinced me to endeavor on this journey, have provided similar guidance throughout the years, and deserve equal recognition.

My former and current committee members, Professor J. Wayne Jones, Professor Michael Atzmon, and Assistant Professor Matthew Collette have also been incredibly helpful teachers, either in the classroom or through my candidacy and data meeting exams, and without their guidance I would not be at this point.

A great many people at Bettis Atomic Power Laboratory made this research possible. Dr. Bob Hermer laid the groundwork for this study, and Cathy Brown picked it up where he left off and provided me with the stress corrosion cracking samples. Dr. Denise Paraventi did the same with regards to the corrosion fatigue samples. Chuck Austin and Jared Malys were instrumental in helping to design and run the surface corrosion tests.

A similarly long list of people at the University of Michigan were also extremely important to my experimental and personal development. From my first mentors in the lab Dr. Allen Hunter, Dr. Yimeng Chen, and Dr. Mukesh Bachhav, and Dr. Yan Dong, to the rest of the Marquis group over my stay, every single person had an impact on my research. The staff at the Michigan Center for Materials Characterization, Dr. Kai Sun, Dr. Haiping Sun, Dr. John Mansfield, and Bobby Kearns were most helpful in equipment training, problem solving, sample preparation, etc.

And finally, this journey would not have been possible without the support of my family and friends. My wife Sydney, especially, helped me get through the difficult times that are inevitable while pursuing a Ph.D. My parents always offered their support, even when they

didn’t understand why on earth I would be spending another 5 years in school. For all of these people, and many more who helped me on my way, I am incredibly grateful.

TABLE OF CONTENTS

LIST OF TABLES

LIST OF FIGURES

LIST OF APPENDICES

LIST OF ABBREVIATIONS AND ACRONYMS

α: Shank angle

APT: Atom probe tomography

ASTM: American society for testing and materials, international

BWR: Boiling water reactor

CFC: Corrosion fatigue cracking

CGR: Crack growth rate

CPZ: cyclic plastic zone

C(T): Compact Tension

CW: Cold work

D: diffusion coefficient (cm^2/s)

EAC: Environmental assisted cracking

EBSD: Electron backscatter diffraction

ECP: Electrochemical potential

EDM: Electric discharge machining

EDS: Energy dispersive x-ray spectroscopy

EELS: Electron energy loss spectroscopy

EPD: Electric potential drop

F: Field (V/nm)

FIB: Focused ion beam

GB: Grain boundary

HE: Hydrogen embrittlement

HELP: Hydrogen enhanced localized plasticity

ICF: Image compression factor

IG: Intergranular

IVAS: Integrated visualization and analysis software

k: geometric factor (unitless)

k_p: rate constant

K: Stress intensity factor

L: L-grade, Low carbon

LEAP: Local electrode atom probe

M: Metal

MA: Mill annealed

$(MC)^2$: Michigan center for materials characterization

P: Plasma

PWR: Pressurized water reactor

R: Radius (nm)

R: Stress ratio

SCC: Stress corrosion cracking

SEM: Scanning electron microscopy

SHE: Standard hydrogen electrode

SRIM: Stopping range of ions in matter

SS: Stainless steel

STEM: Scanning transmission electron microscopy

t: time (hr)

TEM: Transmission electron microscopy

TG: Transgranular

TKD: Transmission Kikuchi diffraction

UV: Ultraviolet

V: Voltage

x: thickness (nm)

Z: depth (nm)

ABSTRACT

Degradation of structural components in nuclear environments is a limiting factor in the lifetime of nuclear power plants. Despite decades of research on the topic, there are still aspects of the degradation phenomena that are not well understood, leading to premature failure of components that can be both expensive to repair and potentially dangerous. The current work addresses the role of material deformation on the corrosion phenomena of 304 SS in a simulated nuclear reactor environment by studying the relationship of the material microstructure and microchemistry with the resulting corrosion products using a multiscale analysis approach.

The general corrosion phenomenon was studied in relation to the surface deformation of the material, and it was determined that surface deformation not only increases the rate of oxidation, but also has a pronounced impact on the microchemical structure of the oxide film when compared to undeformed material. These findings were applied to understanding the role of deformation in the more complex corrosion phenomena of stress corrosion cracking (SCC) and corrosion fatigue cracking (CFC).

In SCC experiments, material deformation in the form of cold work played a synergistic role with unique microchemical features of the materials studied to promote the cracking process under certain environmental and material heat treatment conditions. Despite the fact that the materials studied were low carbon heats of 304L SS thought to be immune to the sensitization and therefore resistant to SCC, elevated boron and delta ferrites in the material were implicated in the SCC susceptibility after heat treatment. On the other hand, low levels of residual deformation played only a minor role in the corrosion processes occurring during CFC experiments over a wide range of rise times. Instead, deformation was suspected to play a larger role in the mechanical cracking response of the material.

By studying multiple corrosion processes of 304 SS a greater understanding of the role of deformation and microchemical factors in the related corrosion phenomena has been achieved, and provides evidence that material and component fabrication, in terms of surface and bulk deformation, material microchemistry, and heat treatment must be considered to avoid degradation issues.

CHAPTER 1:
Introduction

1.1 Background

Type 304 stainless steel (SS) has been widely used for nuclear reactor components for decades. However, through a combination of aggressive environments and loading conditions, it has proven to be susceptible to stress corrosion cracking (SCC) and other degradation phenomena, which can lead to reactor down time and performance issues, or worse, catastrophic failure. Significant effort has been placed on understanding these degradation phenomena, and mitigating them through environmental and material modifications. As the material systems undergo modifications and are incorporated into replacement components, their ability to counteract the associated degradation must be continually addressed before failure occurs.

1.2 Current work

This work was supported by the Rickover Fellowship in Nuclear Engineering in collaboration with the Bettis site of the Naval Nuclear Laboratory. The goal of this project was to evaluate the degradation performance of deformed Type 304 SS and contribute to the understanding of the associated degradation mechanisms. Three forms of degradation in simulated pressurized water reactor environments were addressed: surface corrosion, SCC, and corrosion fatigue cracking (CFC). In order to address these issues, high resolution imaging and chemical measurement techniques were employed.

1.3 Thesis structure

Chapter 2 provides a review of the relevant literature in the topic of corrosion of austenitic stainless steels in nuclear reactor environments, and the open questions that remain in that field. In order to effectively answer some of these questions, high resolution microscopy techniques such as atom probe tomography were employed in this work. An overview of this analysis technique in regards to its use for studying oxide materials, along with its limitations pertaining to its application to the remainder of this work, is presented in Chapter 3. Chapter 4

focuses on developing an understanding of the role of surface deformation on surface corrosion of 304 SS in simulated pressurized water reactor environments, and provides a foundation for chapters 5 and 6. Chapter 5 discusses the roles of bulk deformation, and minor element impurities in the SCC of dual certified Type 304/304L SS in high temperature water, and Chapter 6 discuss the role of bulk deformation in the corrosion response during CFC of 304 SS. Finally, Chapter 7 summarizes the findings and provides conclusions and suggestions for future work on the topic.

CHAPTER 2:

Type 304 SS in Aqueous Environments: Literature Review

2.1 Type 304 SS in nuclear reactors

Type 304 stainless steel (SS) is an austenitic Fe-Cr-Ni alloy that is extensively used in a wide variety of applications. The chemical and strength specifications for Type 304 SS and Type 304L SS are shown in Table 1. Notably, 304 SS has additions of approximately 18 wt% Cr and 9 wt% Ni, maximum carbon content of 0.07 wt%, and tensile and yield strength minimums of 75 ksi and 30 ksi, respectively, and maintains relatively high strength even at elevated temperatures [1]. 304L SS is a low carbon grade with similar compositions, but a maximum carbon content of 0.03 wt%, and less strict tensile and yield strength requirements of 70 ksi and 25 ksi, respectively. Manufacturers often produce a dual certified 304/304L SS which meets the stricter strength requirements of 304 SS, and the stricter carbon requirements of 304L, in order to decrease manufacturing costs associated with producing multiple materials.

304 SS is of particular interest for high temperature applications due to its strength properties as well as its good corrosion resistance and weldability, which has resulted in its extensive use throughout boiling water nuclear reactors (BWRs) and pressurized water nuclear reactors (PWRs), both in the primary (radiation) and secondary (no radiation) sides. Type 316 SS is similarly used in nuclear reactors, and has thus been studied extensively for its corrosion properties in similar environments. The strength requirements are the same as in 304 SS. However, 316 SS has increased Ni content and added Mo, both of which are meant to improve the corrosion resistance in certain conditions [1]. The corrosion products observed on 304 and 316 SS are generally comparable. Type 316 SS is mentioned here because many of the results discussed in the future sections were obtained on 316 SS, although this may not be explicitly stated.

2.2 Commercial nuclear reactor environments

In the secondary side of a PWR, materials are exposed to high temperature water, but neither the water nor the material is exposed to radiation. On the other hand, in BWRs, and on the primary side of PWRs, radiation effects become important both within the material and in terms of water radiolysis. The current work focuses on a simulated, secondary side, PWR environment, but prior research into the corrosion phenomenon of 304 SS spans a wide range of water chemistries and temperatures matching conditions found in both types of reactors, and is included in this review.

The typical operating temperature for both reactor types is 288 °C, with temperature transients and 'normal' conditions fluctuating depending on location in the reactor and the specific reactor setup. As such, corrosion research regularly spans temperatures from ~250 °C to 350 °C depending on the intended application.

The main difference between BWR and PWR research is often in the oxygen content of the water and water additions. On the primary side of PWRs hydrogen is added at levels up to 50 cc H_2/kg H_2O to reduce the oxygen content in the water and thereby decrease corrosion processes. Boric acid is added to help control the reactor power by limiting the fission reaction, while lithium hydroxide is added to raise the pH back towards neutral, thereby mitigating some of the corrosion risks [2]. On the secondary side of PWRs hydrogen is also added to control the oxygen content with a goal of keeping it below 20 ppb [2]. Additional oxygen can accumulate in occluded areas, resulting in unintended localized water chemistry that has been linked to corrosion problems [3].

In BWRs oxygen can be present due to water radiolysis or during reactor start up procedures. Radiolysis results in the breakdown and recombination of water molecules into oxygen and hydrogen peroxide, resulting in normal operating conditions up to 400 ppb O_2 [4]. During start up water may be air-saturated up to levels of 8 ppm [5]. Hydrogen is added to the water to scavenge oxygen by reacting with oxygen and hydrogen peroxide to form water, reducing the oxygen content back to approximately 10 ppb [4].

Additional water chemistry considerations include the presence of anions such as sulfates and chloride ions that exist as contaminants and have a detrimental effect on 304 SS by increasing the rate of corrosion processes, and ultimately failure [6, 7].

2.3 Surface corrosion in high temperature aqueous environments

Understanding the properties of the corrosion films that form on the surface of 304 SS in reactor environments is the first step in understanding other corrosion processes such as stress corrosion cracking (SCC) and corrosion fatigue cracking (CFC). Much work has been done to understand how material and environmental conditions affect the corrosion of 304 SS, but some important factors are still not well understood.

2.3.1 Methods of identifying corrosion products

There are a number of methods typically used to characterize corrosion products phases and/or chemistry. Chemical techniques usually include energy dispersive x-ray spectroscopy (EDS), electron energy loss spectroscopy (EELS), x-ray photoelectron spectroscopy (XPS), and atom probe tomography (APT). Structural techniques include x-ray diffraction (XRD), Raman spectroscopy, electron diffraction, XPS, and electrochemical techniques. None of these techniques can unambiguously distinguish both the phase/structure and the microchemical contributions of different elements, which is particularly important in studying a multi-component alloy such as 304 SS. Combinations of these techniques have been used to gain a general understanding of the corrosion products, as discussed in the next sections.

2.3.2 Corrosion in oxygenated water

In oxygenated water several authors have reported the formation of two distinct oxide layers. The outer oxide layer is composed of discrete crystals of varying sizes, and has been identified as maghemite (γ-Fe_2O_3) [8, 9], hematite/corundum (α-$(Fe,Cr)_2O_3$) [3, 8, 10-14] and Fe-rich mixed M_3O_4 spinel (magnetite/nickel ferrite) [3, 13, 14]. Some Ni is incorporated into the outer oxide particles [3, 8, 12, 15] while relatively less Cr is reported [3, 8].

The inner layer oxide formed in oxygenated water is nanocrystalline, as indicated by a ring electron diffraction pattern [3, 8]. It is rich in Cr and deficient in Fe compared to the matrix, and most often identified as a mixed Fe-Cr spinel (AB_2O_4) [3, 8, 11, 15].

Differences in the reported phase structure and chemistry may be a result of different measurement techniques, as discussed, but also result from variations in the environmental factors. For instance, different levels of dissolved oxygen in the water have been shown to effect the ratio of hematite to magnetite formation [12], while pH level changes the incorporation of elemental species [15]. It has also been concluded that injection of metal ions from the test vessel can affect the chemistry of the outer oxide film [16].

2.3.3 Corrosion in deoxygenated water

The oxide product formed in deaerated water bears some similarities and some differences to that formed in oxygenated water. A dual layer oxide structure is still observed, with an outer oxide layer formed of discrete crystals [8, 17-22] and a nanocrystalline inner oxide layer [8, 19, 22]. However, in deaerated water the outer layer is consistently identified as the more oxygen deficient magnetite or nickel ferrite phase [8, 17-21, 23, 24], and not hematite. Similar to in oxygenated water, the inner oxide is Fe-deficient (or Cr-rich) and is identified as a spinel [8, 18, 20, 22, 23, 25] or a corundum (M_2O_3) [8, 19, 24, 26-28].

2.3.4 Oxide phase stability and chemistry

Predicted Pourbaix (potential vs. pH) diagrams can be used to gain a general understanding of the thermodynamic stability of oxide phases in aqueous environments. A Poubaix diagram generated using OLI thermodynamic prediction software for the Fe-Cr-Ni system is shown in Figure 1. The oxygen content of the water plays a role in the oxidation potential where higher potentials are associated with higher oxygen contents, while water additions as discussed previously determine the pH. At neutral pH the spinel phases $FeCr_2O_4$ and $NiFe_2O_4$ are clearly favored at low potentials, while the hematite/corundum phases are favored at lower pH and higher potentials. These results are consistent with observations of the phases reported in oxygenated and deoxygenated environments discussed in the previous two sections.

Some authors have reported a complete solid solution of Fe_3O_4 and $FeCr_2O_4$ [29] allowing for stable inner oxide compositions with Cr contents ranging from 0-29 at% Cr. However, Fe_3O_4 is a cubic inverse spinel, while $FeCr_2O_4$ is a normal spinel, indicating complete miscibility is not accurate at temperatures below 880°C [17]. Ziemniak et al. reported the thermodynamically stable chemistries of the immiscible phases at 260°C to be $Fe(Fe_{0.85}Cr_{0.15})_2O_4$ and $Fe(Fe_{0.35}Cr_{0.65})O_4$ [17, 30].

2.3.5 Mechanisms and growth rates

Two mechanisms are discussed for oxide growth in aqueous environments. The first mechanism is metal-dissolution oxide-precipitation, in which metal ions first dissolve forming a supersaturated layer in the fluid, causing them to re-precipitate on the surface in oxide form. The second mechanism is a solid state growth process, which can manifest in inward growth at the oxide/metal interface by oxygen ingress, or outward growth at the solution/surface interface by metal egress. Solid state growth can occur either selectively or non-selectively. In selective

oxidation the least noble element (Cr in an Fe-Cr-Ni alloy) is preferentially oxidized. In an outward growth model this would result in depletion of the metal below the oxide/metal interface [29], while for inward growth rejection of other metal components would occur. On the other hand, in non-selective oxidation the overall composition of metal in the oxide matches that of the original matrix, necessitating a volume expansion [29]. The term 'non-selective' oxidation has also been used to describe the growth of a dual layer structure where all of the the metal components are incorporated into both oxide layers, and the distribution is determined by cation diffusion rate in the oxide [17]. In spinel oxides Fe^{2+} is the fastest diffusing species in the oxide lattice, followed by Ni^{2+}, both of which are much greater than Cr^{3+}[29].

A double layer oxide could result from either (1) both layers forming by dissolution-precipitation [31], (2) both by solid state reactions [29], or (3) the outer layer by precipitation and the inner layer by solid state growth [32]. In recent literature, the inner layer is universally concluded to form by inward, solid state growth. The outer oxide is often reported to form by a dissolution-precipitation reaction [14, 25, 32], while some favor a solid state, outward growth mechanism [3, 11, 17, 18].

The growth rate taking into account both oxide films can be fit with a parabolic rate law of the form

$$x = k_p t^{0.5} \quad (1)$$

where x is the thickness, k_p is the rate constant, and t is the exposure time [17, 18, 21, 22, 28]. This type of rate law is consistent with growth governed by diffusion through the oxide film. Slower kinetics, such has cubic or logarithmic, have been measured in certain cases, and are likely the result of diffusion being impeded by additional factors, such as a charge build up in the oxide [20, 33]. The presence of deformation potentially affects the measured oxidation rate due to the possibility of short-circuit diffusion pathways along dislocation networks that enhance the diffusion rate compared to oxide lattice diffusion [18, 29, 34].

2.3.6 Role of deformation

The role of surface or bulk deformation is complicated by the fact that the amount of deformation is often not known, or the material conditions are not fully reported. Deformation is important from an applications perspective, as materials used for components in reactor systems are likely to exhibit bulk deformation or surface abrasion or deformation from machining or

fabrication procedures. A few authors have explicitly studied the role of deformation on the oxidation process of 304 SS in high temperature water.

Early work by Maekawa et al. identified that in deaerated water pickled surfaces corroded at a lower rate than abraded surfaces below 300 °C, while no surface finish affect was observed in aerated water [9]. Furthermore, slight differences in the oxide phases on abraded and pickled surfaces have been suggested in deaerated water [9, 28] which may be a result of Cr enrichment at the surface during the pickling treatment. More recent work by Zeimniak et al. suggested that electropolished surfaces exhibited a factor of three decrease in corrosion rate compared to machined surfaces [18]. While no differences in the oxide layer chemistry were observed, the size of outer oxide particles were smaller on electropolished surfaces. This was attributed to the formation of a more uniform, protective inner oxide layer on electropolished surfaces that suppressed the flux of Fe to the surface, whereas on machined surfaces nucleation of the inner oxide occurred preferentially at high energy surface sites imparted by machining, resulting in a more porous and less protective inner oxide layer [18]. Morrison et al. also observed lower corrosion rate on specimens hand polished to a mirror finish compared to ground [21]. On the other hand, Ming et al. suggested that cold working the surface layer by grinding allowed for easier Cr diffusion to form a protective oxide scale, lowering the overall corrosion rate compared to smooth surfaces [14]. It was concluded that the surface roughness induced by grinding resulted in higher corrosion rate of ‘peaks’ and lower corrosion rate of ‘valleys’ resulting in a non-uniform oxide product distribution. Using APT, Lozano-Perez et al. first highlighted the role of bulk cold work on the nanoscale corrosion processes of 304 SS after long term exposure in high temperature deaerated water by showing oxide precursors formed along deformed pathways [34].

2.3.7 Unknowns

Despite significant research on the macroscopic properties of the oxide products resulting from corrosion in high temperature aqueous environments, little emphasis has been placed on understanding the microscopic processes happening within the inner oxide layer and at the oxide/metal interface, where the corrosion process is thought to be actively occurring. Furthermore, there exists contradictory reports on the role of bulk and surface deformation on the corrosion rate and resulting corrosion products. Historically the nano-scale processes occurring at the interface were nearly impossible to observe first hand, but recent work utilizing APT and

TEM has identified possible interactions of the oxide with the deformed microstructure [34, 35]. Similar high resolution observations at the oxide/metal interface of stress corrosion crack tips have identified a relationship between the oxidation process and microstructural features in highly deformed materials [36-39]. In both cases, no comparisons were made to undeformed material, making the actual role of the deformed microstructure unclear. Furthermore, the explicit mechanisms of oxidation in relation to the deformation structure were not determined.

2.4 Stress corrosion cracking in high temperature aqueous environments

SCC is a cracking phenomenon that results from three coinciding factors – a susceptible material, a corrosive environment in which that material is susceptible, and an applied (tensile) stress state that acts to initiate or accelerate the cracking mechanism [40]. A variety of components in both BWRs and PWRs have been found to be susceptible to SCC, a detailed review of which can be found in Ref. [40]. The following review focuses on the material and environmental factors leading to SCC susceptibility for 300 series stainless steels. SCC can additionally be found in nickel alloys and as a result of irradiation (known as irradiation assisted SCC), but in these cases is typically a result of different material factors, and thus not reviewed in detail here.

2.4.1 Environment

The main environmental considerations for SCC are the oxygen content of the water, temperature, and impurity ions in the water.

2.4.1.1 Oxygen content

A material's propensity for SCC has been directly linked to the electrochemical corrosion potential (ECP) of the water environment; reducing the ECP to less than -230 mV_{SHE} drastically decreases SCC susceptibility [4, 41, 42]. The ECP of the system, in turn, is directly linked to the oxidizing species in the water, including oxygen. SCC suppression has necessitated the addition of oxygen scavengers, such as hydrogen, as discussed previously. Oxygen is especially detrimental to SCC in sensitized materials [43], which will be discussed later. Oxygen content is thus strictly controlled during testing in order reproduce the desired environment to test for SCC susceptibility.

2.4.1.2 Temperature

Typical operating temperatures for BWRs and PWRs is ~250-290 °C depending on the location of interest, but due to potential temperature transients during reactor operation, SCC has been studied over a wider range of temperatures. It is generally agreed upon that the crack growth rate (CGR) increases with temperature up to a point and then starts decreasing [39, 44-47]. The temperature at which the fastest CGR is observed, however, depends on a variety of other factors including material and environmental conditions [44, 45]. In deaerated water, the peak in CGR is around 320 °C and is attributed to a difference in the factors controlling CGR in the different temperature regimes – diffusion at high temperatures versus mechanical strain concentration at lower temperatures [45]. In aerated water, the maximum CGR occurred at a lower temperature, around 200 °C, and is attributed to temperature induced changes in the ECP and pH of the environment [44]. Temperature is generally controlled according to the conditions of interest for the material being studied.

2.4.1.3 Impurity ions

Impurity ions have an accelerating effect on SCC initiation and propagation, especially in oxygenated water and at higher temperatures [6, 7]. Specific impurities of interest include sulfate and chloride ions, which may be present from demineralizer resin degradation or seawater intrusion, respectively [6, 7, 48]. The role of ions in the SCC initiation and propagation has been linked to their effect on the passivating properties of the oxide film [48]. For instance, sulfate ions breakdown the protective oxide that forms on 304 SS, accelerating the dissolution process that occurs at Cr-depleted grain boundaries [48]. Thus, sulfate ions are often included in SCC testing either when they might be present in the actual environment of interest, or to purposely accelerate the SCC response of potentially susceptible materials.

2.4.2 Material

Material susceptibility is perhaps the most important factor in SCC, with cold work or sensitization being directly linked to most instances of SCC [40].

2.4.2.1 Sensitization

Sensitization of 304 SS occurs when intergranular Cr-rich $M_{23}C_6$ carbides form during heat treatment, resulting in Cr depletion of the surrounding grain boundary (GB) and rendering it susceptible to intergranular corrosion. Sensitization is of practical importance in nuclear reactor

components because the heat treatment times (<10 hours) and temperatures (500-900°C) that promote carbide precipitation are easily achieved in the heat affected zones of welded components, or at conditions that are used for healing the microstructure of cold worked material or stress relief heat treatments [40, 49]. Susceptibility to intergranular corrosion is expected when the Cr level at the GB is depleted to levels below 12% (from approximately 20% in the original matrix), as a protective, passive oxide film can no longer form at such low Cr levels [50]. Intergranular corrosion is then a pretense for intergranular (IG) SCC.

Cr depleted grain boundaries oxidize readily, and have been directly linked to propensity for SCC in 300 series SSs in aerated water [43, 44, 51, 52]. The enhanced SCC response is due to easy rupture of a thicker, less protective oxide film, coupled with enhanced dissolution of the Cr depleted GBs [48].

A continuous network of carbides, even in the absence of Cr depletion, also has a detrimental effect on SCC response in aerated water [51]. This has been attributed to a mechanical embrittlement mechanism or an electrochemical galvanic corrosion mechanism [51]. On the other hand, in deaerated water carbides have been shown to have a beneficial effect in decreasing SCC by inhibiting GB sliding, even in the presence of Cr depletion [53, 54].

Since sensitization has been proven to be a direct factor to SCC in oxygenating environments, a number of methods have been employed to quickly measure the potential for sensitization of a material. ASTM A262 describes several destructive acid etch tests that can be used to screen a material for potential susceptibility to SCC [55]. Double loop electrochemical potentiokinetic reactivation (DL-EPR) has also been employed to measure an actual ‘degree of sensitization’ [56]. Finally, analytical techniques have been used to measure the actual amount and width of Cr depletion at the sensitized GBs [57]. All of these techniques have been instrumental in understanding the role of sensitization in SCC.

2.4.2.2 Other minor elements

In an attempt to reduce the effects of corrosion and sensitization by carbide precipitation in 304 SS, alternative 300 series stainless steels have been used. As noted previously, 316 SS has very similar properties to 304 SS, with the major difference being the addition of Mo. Mo improves the corrosion resistance of 316 SS compared to 304 SS, particularly by reducing pitting corrosion. It also decreases the segregation kinetics of other impurity elements such as P. However, it has been found to have no effect on the IGSCC susceptibility of 300 series stainless

steels [54]. 321 SS incorporates Ti additions to preferentially form titanium carbides during heat treatment, thereby reducing Cr carbide precipitation at grain boundaries and the related Cr depletion [58]. 347 SS incorporates Nb for the same reason [52], and has been found to be more effective than Ti [40]. However, SCC has still been observed in these materials [40, 58].

Another option is to reduce the carbon level in the material, which is the basis for L-grade 304L and 316L stainless steels, as discussed previously. However, in these low carbon materials other minor element additions are sometimes necessary to maintain the desired material properties. Boron, for instance, can be added in low carbon steels to restore hot workability and improve ductility [59], while nitrogen is added to maintain strength in the absence of carbon [58, 60]. Both of these elements have the potential to form Cr-rich precipitates if present in sufficient quantities and under the right heat treatments [59, 60].

Still other impurity elements are present in 300 series stainless steels to varying degrees and have been noted to affect SCC propensity. Phosphorous, for instance, is insoluble and segregates at grain boundaries [60], and has been linked to SCC in annealed, cold worked 304 SS [61]. GB metalloids (like P and S) have been hypothesized to promote hydrogen embrittlement by serving as recombination poisons, allowing for increased H atom absorption into the metal lattice [61, 62], providing one possible explanation for their role in SCC. Sulfur can additionally be found in manganese sulfides within the steel matrix [60] and once dissolved has been implicated in the decrease in passivation of 304 SS, leading to increased corrosion response [63, 64].

While specifications for 304 and 304L SS indicate maximum allowable levels of some of these impurities (such as P and S), others, like B, are not included in the specifications [1] and thus have the potential to have unexpected consequences in regards to SCC.

2.4.2.3 Delta ferrite

The delta ferrite phase is of practical importance in studying the SCC response of 304 SS, as it can be present as a second phase in the matrix depending on the steel composition and cooling rate [65]. Furthermore, delta ferrite can have a beneficial effect in the solidification characteristics of weld metal by reducing microfissuring, and is thus purposefully incorporated into welds [66]. Ni, Mn, C, and N all serve as austenite stabilizers, while Cr, Si, and Mo are ferrite stabilizers [67], so the Ni/Cr ratio in 304 SS can influence the likelihood of ferrite

formation. In cold worked stainless steels, the delta ferrite is oriented along the rolling direction in the form of stringers [68].

The delta ferrite/austenite interface is also a preferential nucleation site for Cr carbides during sensitization heat treatment [68-70], which can be attributed to the faster diffusion of Cr in ferrite than austenite [70, 71]. This diminishes the potential for GB carbide precipitation and Cr depletion at austenite grain boundaries, which has been attributed to increased resistance to intergranular corrosion [70, 72] and SCC [73, 74], although enhanced corrosion [70] and cracking [74] of the austenite/ferrite interface can occur.

2.4.2.4 Cold work

Cold work (CW) is the second factor (in addition to sensitization) that has been inextricably linked to propensity for SCC [39, 40, 47, 61, 75, 76]. It can be present uniformly in a material, or primarily at the surface as a result of grinding or machining of a component [40]. In studies on SCC, cold working is usually applied by uni- or multi-directional cold rolling or pulling to a percentage reduction in thickness, which is then termed as X% CW. The direction of rolling with respect to the crack path can have a pronounced effect on SCC susceptibility [39]. CW serves to increase the yield strength of the material, decreasing the plastic zone size and enhancing strain gradients near the crack tip [77]. Increasing levels of deformation increase the yield strength and the deformation microstructure, as well as induce martensite formation, but deformation levels as low as 5% CW have been noted to increase the SCC response compared to undeformed material [39, 75, 78].

CW can also enhance the role of sensitization by increasing the short range diffusion rate of carbon and chromium in the time and temperature ranges in which sensitization occurs. However, at very high levels of deformation desensitization occurs by increasing the rate of longer range diffusion of Cr allowing for the replenishment of Cr in relatively short time frames [79, 80]. Sensitization [79] and oxidizing [75] conditions in conjunction with CW tend to increase the crack response compared to undeformed material tested under the same conditions.

2.4.3 Stress

Stress is the final integral factor in SCC, and in most cases is the hardest to control in actual reactor components. The most common sources of stress include residual stresses due to weld shrinkage upon cooling, but other factors such surface residual stress from machining can

also play a role in SCC [40]. SCC testing is performed in a wide variety of ways which induce stress differently. U-bend specimens have only residual stress from bending and can be used to see if SCC occurs, but the time to induce cracking or CGR cannot be measured [81]. 'Slow strain rate' and 'constant extension rate' tests continually increase the strain on the material which helps to drive crack growth [81], but may not be indicative of real SCC crack growth behavior in the reactor environment. Other tests use feedback to maintain a constant stress intensity factor (K) [77] or fully static constant load [53] (decreasing K). Sometimes partial periodic unloading is employed to maintain a straight crack front [82]. Therefore, it is important to note the type of test and test parameters used when studying SCC.

2.4.4 Crack growth mechanisms

It is likely that no single model will ever describe SCC crack growth under all of the applicable material, environment, and stress conditions that could occur. However, two main mechanisms are typically referred to in the discussion of SCC of 300 series stainless steels in reactor environments: film rupture (also referred to as slip-dissolution) and hydrogen assisted cracking (which encompasses a number of mechanisms). While other models for SCC certainly exist, they tend to be applicable to other material systems (for instance, internal oxidation for SCC in nickel alloys), or have not garnered support in the literature.

The main premise of the film rupture model is that the passive surface oxide ruptures, revealing bare metal. This bare metal eventually oxidizes or repassivates, forming a new oxide film on the surface. This oxide film is brittle and cracks under stress, exposing new bare metal at the crack tip, repeating the process [83, 84]. Additional procedures, such as the dissolution of bare metal before repassivation to advance the crack into the plastic strain field of the crack tip, have been proposed as modifications to this mechanism [85]. This mechanism is thought to be highly applicable to IGSCC of sensitized 304 and 316 SS in oxygenating conditions, as the Cr depleted GBs provide a pathway for enhanced anodic dissolution and a thicker, less protective oxide film due to the low Cr content [43, 48]. Even if this model is not perfectly correct, it has been used to adequately predict laboratory SCC crack growth rates, and is the basis for the 'plant life extension diagnosis by GE' (PLEDGE) model used in industry [58, 86, 87].

Hydrogen assisted cracking models are also often discussed in terms of SCC, and indeed may not be independent from the film rupture model discussed previously. Hydrogen may be present as a water addition in PWRs, but it also may exist in the crack enclave as a corrosion

product [38]. In this capacity, it serves to acidify the water changing the structure and protectiveness of the oxide film [43], and it may also diffuse through the metal microstructure and accumulate ahead of the crack. Hydrogen is known to embrittle metals [88], but austenitic stainless steel is thought to be relatively immune to such embrittlement due to the low diffusion rate in austenite [78]. By cold working the material trapping sites for hydrogen are made available, and hydrogen embrittlement has been used to explain the increased crack response of such materials [78]. The diffusion of hydrogen into the deformed region ahead of the crack tip is thought to aid in the deformation process, which is the basis for the hydrogen enhanced local plasticity (HELP) model [89, 90]. However, Andresen has argued that SCC crack growth is inconsistent with hydrogen controlled mechanism based on studies varying hydrogen content in the environment [91]. Additionally, one would expect to observe the formation of hydrogen filled voids in the crack tip vicinity [92], which have not been observed.

2.4.5 Oxide properties

Advances in microscopy techniques have recently allowed for direct characterization of crack tips and their oxides and surrounding microstructure. The oxide properties parallel those that are observed on oxidized surfaces in similar environments: a dual layer structure composed of a Cr-rich nanograined inner layer and an outer layer of discrete Fe-rich oxide particles [37, 38, 93-97]. In aerated water there has been a noted difference in the oxide structure on the surface versus in the crack trip, suggesting a difference in the oxygen content in the crack enclave [38]. On the other hand, in deaerated water, no difference was observed and the oxide structure was magnetite particles on top of a Cr-rich spinel [38]. A similar oxide structure has been observed within deformation bands along the crack flanks in highly cold worked materials [94, 98].

Ni enrichment has been observed at the oxide/metal interface and at the GB ahead of the propagating crack [37, 38, 92, 95, 96]. This enrichment is attributed to Ni being the most noble element and being pushed out of the oxide to accumulate at the interface [92, 95, 96]. While there is no conclusive evidence that the Ni enrichment serves to change the cracking mechanics, it has been pointed out that as an austenite stabilizer it may prevent a stress-induced martensite transformation at the crack tip [96].

2.4.6 Unknowns

Much work has been performed on understanding the material and environmental factors that lead to SCC. This work has led to predictive models to estimate a materials lifespan, and to

changes in reactor environments and material parameters in an attempt to mitigate SCC, or at least ensure damage by SCC is not catastrophic. More recently, a wide variety of microscopy techniques have been employed to study the processes occurring at the crack tip, leading to new methods of studying SCC.

Due to this wide variety of factors that can promote SCC, as discussed above, and the large range in scale over which it can be studied, there is still work to be done in understanding SCC. As noted, 304L has been adopted for use in reactor component applications to mitigate the risk of SCC resulting from GB Cr depletion. However, it has not been extensively evaluated for SCC resistance, especially under the range of material and environmental conditions noted to affect SCC susceptibility. The current work utilizes APT and transmission electron microscopy (TEM) to study the oxide and GB chemistry in dual certified 304/304L stainless steel, to elucidate the synergistic roles of CW and minor elements (boron and carbon) in this material on the SCC growth under different heat treatment and environmental conditions. Findings are discussed in terms of the surface oxides on deformed and electropolished surfaces as well.

2.5 Corrosion fatigue cracking in high temperature aqueous environments

Corrosion fatigue of 300 series stainless steels in high temperature aqueous environments is a comparatively newer field of study, with significantly less literature and understanding of the cracking properties. Fatigue cracking refers to cracking induced by a cyclic load form, and is typically transgranular in nature. In the case of CFC, the CGR is typically enhanced in a corrosive environment above the baseline fatigue CGR under ‘normal’ conditions – in this case, air [64, 99-101]. Fatigue in nuclear reactors components can result from either mechanical or thermal loading changes, but the fatigue process is not typically due to purposeful cyclic loading as in rotating machinery (e.g. aircraft impellers) [102]. Historically, fatigue life of such components has been based on applying correction factors to fatigue curves generated using sample specimens in air, but there is an increasing body of evidence suggesting that such corrections are inadequate for applications in high temperature water [101]. More recently, additional correction factors have been adopted, which may lead to over-conservatism. As such, there is increasing work on understanding the mechanisms of corrosion fatigue crack growth in high temperature aqueous environments.

In air fatigue the CGR is relatively independent of rise time. However in environmentally enhanced corrosion fatigue there is an increase in CGR with respect to rise time [99, 103]. Thus

a baseline for corrosion fatigue CGR is determined at a short rise time. This baseline is consistently higher than CGR in air fatigue under the same loading conditions. Retardation typically refers to suppression of the CGR below the low rise time baseline, and the CGR has even been observed to be suppressed to levels similar to or below those observed in air fatigue [64]. Factors leading to enhanced and retarded corrosion fatigue are reviewed below, along with associated mechanisms leading to each.

2.5.1 Factors that enhanced corrosion fatigue crack growth rate

Recent work has identified that corrosion fatigue CGR in high temperature water can be enhanced 10-100 times measured CGRs in air [64]. This enhancement is observed with increasing rise times, and is associated with 'normal' corrosion that occurs in environment. For instance, large rise times allow for increased time for corrosion and degradation, and thus continues to enhance CGR. Enhanced CGR is therefore considered 'normal' in corrosion fatigue, and exists under a wide range of variables including temperatures, ΔK's, R's, rise times, hold times, load forms, water chemistry, etc. [100, 102]. Some conditions that are expected to always result in enhanced CGR include high ΔK values (>15 MPa√m), short rise times, and very high R's.

2.5.1.1 Mechanisms of enhancement

A number of mechanisms leading to environmental enhancement of CFC have been discussed in the literature. Some authors have tried to describe CFC using a slip dissolution model similar to that proposed for SCC with additional parameters added for the cyclic loading components in air [100, 104]. However, the model has proven to underestimate crack growth under some conditions, suggesting additional mechanisms are at play. Hydrogen effects have also been discussed in relation to environmental enhancement of CFC. Based on fracture surface examination revealing cleavage-like facets, hydrogen was thought to be absorbed and promote enhanced planar slip, leading to enhanced CGR [64]. This mechanism has since been questioned after microstructural examination of the crack tip region after environmentally enhanced cracking failed to identify planar slip [105]. Corrosion along planar slip bands has also been suggested to accelerate cracking by impeding reverse planar slip during unloading, but this mechanism was considered secondary to hydrogen effects [64].

2.5.2 Factors that retard corrosion fatigue crack growth rate

Interestingly, CFC can be retarded under certain environmental, material, and loading conditions. From a design standpoint, it is very important to understand the conditions that lead to crack growth retardation, as it could lead to removal of unnecessary conservatism in fatigue design. Moderate retardation, or less enhanced crack growth refers to conditions that result in a plateau of the CGR with increasing rise time. In this condition, the CGR is still higher than that observed in air, but retarded with respect to full enhancement observed under normal cracking conditions. Full retardation, however, refers to materials that actually exhibit a decrease in corrosion fatigue crack growth with respect to the short rise time baseline, and in some cases has been observed to result in CGRs that approach the air rates. Retarded crack growth in most cases has been linked to accelerated corrosion effects [64, 99, 103, 106, 107].

2.5.2.1 Low R

Crack growth retardation is observed at low R, in the range of 0.1-0.3. In these loading conditions, corrosion products prevent the full cycle load from being effective at the crack tip, thereby reducing the CGR [64].

2.5.2.2 Elevated sulfur

Sulfur content of the material, or injected sulfur into the environment, have been implicated in the retardation of CGR under a wide variety of loading conditions, and result in some of the most extensive retardation observed [64, 103, 107]. Sulfur may be naturally present due to the dissolution of manganese sulfides present in some 304 SS heats, and is known to destabilize the protective nature of the passive oxide film, resulting in increased corrosion and excessive oxide product. Indeed, increased corrosion products have been observed in high sulfur materials compared to low sulfur materials tested under the same conditions [99]. Such retardation has been observed in materials with bulk sulfur contents as low as 0.006%, but is pronounced in higher sulfur materials with sulfur content up to 0.03% [64].

2.5.2.3 High water flow rate

Flow rate serves to increase the corrosion rate by flow induced convection that increases the cathode corrosion reaction at the crack tip [106]. Heavy oxide films have been observed in materials tested under high flow rate conditions [106].

2.5.2.4 Long rise or hold times

During long rise time and long hold time tests an active load is present for an extended period of time. This has been hypothesized to result in increased corrosion of the actively strained crack tip region which disrupts the action of planar slip associated with enhanced CGRs [64]. Such conditions have been observed to moderately retard the CGR in high R conditions [64].

2.5.2.5 High temperatures

Increasing the temperature from ~240 °C to ~340 °C has been shown to decrease the rise time at which CGR starts to exhibit retardation [64]. This has been attributed to increased corrosion kinetics resulting in thicker oxide films at higher temperatures.

2.5.3 Mechanisms of retardation

While enhanced corrosion has been implicated in the retardation of CGRs under certain conditions, the mechanisms of retardation are still unclear. There have been several attempts at explaining the role of corrosion in the retardation mechanism and the conditions under which that mechanism may apply.

Corrosion-induced crack closure refers to the buildup of oxide to an extent such that upon unloading the corrosion product wedges the crack tip area, resulting in the effective full cycle load not being applied to the crack tip region [64]. This mechanism is most likely applicable in the low R and ultra-low ΔK regimes. Furthermore, it should be easily recognizable as the corrosion product should appear damage or abraded from rubbing during unloading [64].

Injected vacancy enhanced creep (IVEC) is a model that attempts to explain the role of accelerated corrosion in higher R conditions. In the IVEC mechanism it is proposed that vacancies are injected ahead of the crack tip during corrosion by the simultaneous outward diffusion of cations [64]. These vacancies promote solute diffusion ahead of the crack tip and creep via dislocation climb, blunting the crack tip and disrupting planar slip associated with enhanced CGRs [64]. Recently, however, high resolution microscopy has called into question the role of planar slip in the role of enhanced corrosion fatigue crack growth [105].

Hydrogen effects may also play a role in the retardation mechanism. Hydrogen is likely present as a corrosion product, due to hydrogen deaeration of the water, or from the material itself. While hydrogen effects have been suggested for playing a role in enhancement of

corrosion fatigue by promoting planar slip [64], they may play a different role in the retardation of CFC by interaction with the deformation structure at the crack tip. It has been suggested that long rise time allow for increased hydrogen accumulation at the crack tip, reducing the necessary stress for planar slip, thereby reducing the effective ΔK, and resulting in crack tip blunting that retards crack growth [105].

Finally chemical blunting has also been associated with fatigue crack growth retardation by dissolution of the crack tip in mild steels [108]. Each successive cycle results in a slight increase in the crack tip radius by continued dissolution, reducing the effective ΔK, and eventually crack arrest occurs under moderate to low ΔK conditions [108]. Such a mechanism is not prevalent in the corrosion fatigue crack literature of 304 SS in high temperature water environments.

2.5.3 Unknowns

As a relatively young field, the mechanisms of enhancement and retardation of corrosion fatigue crack growth, and the factors that affect them, are still far from understood. However, it is generally believed that enhanced corrosion response, in some way or another, is directly related to the observed retardation phenomenon. Notably absent from the literature, until very recently, is the characterization of the crack in terms of the oxide morphology and deformation structure in the crack tip region. Instead, nearly all conclusions on corrosion fatigue have been made by examining only the fatigued apart fracture surface. Thus, it is not well understood how rise time, a factor known to promote retardation, may affect the corrosion response at the crack tip, particularly in the presence of material deformation.

2.6 Summary

There are a number of corrosion related phenomenon that prove to be limiting factors in the use of 304 SS in nuclear reactor environments. While many studies have been done characterizing corrosion products under various conditions, there are still open questions particularly pertaining to the role of deformation in the corrosion processes, and the relationship between the corrosion processes observed under different corrosion and cracking mechanisms. In the surface corrosion of 304 SS a general understanding of the two layer structure of the resulting oxide is well established. However, there has been little focus on deformation induced differences in the corrosion product and at the corrosion front, despite the fact that it ultimately controls the corrosion process. Chapter 4 seeks to address this question.

CW has also been implicated in enhanced propensity for SCC, along with other material factors such as sensitization. While 304L SS has been recommended as a replacement material to avoid the issues of sensitization, it has not been properly evaluated to ensure it is resistant to SCC. In chapter 5 the SCC response of 304L SS is addressed, with special attention paid to the role of microchemical factors. Additional analysis relating the oxide product from within the crack to that observed on electropolished and deformed surfaces is also provided, in an attempt to further clarify the role of CW in SCC.

Finally, CFC in high temperature water is an additional corrosion phenomenon that is a relatively young field compared to surface corrosion and SCC. However, it has been noted that certain conditions can result in retardation of the CFC response, and these conditions have largely been linked to acceleration corrosion phenomenon. Based on the results presented on surface corrosion and SCC of deformed materials, it may be expected that deformation would also be an acceleration factor for corrosion in corrosion fatigue, resulting in retarded crack growth. The corrosion fatigue crack growth response in terms of CGR and oxidation under different rise time conditions is addressed in Chapter 6.

Table 1: Chemical (wt%) and strength specifications for 304 and 304L SS

	Carbon (max)	Mn (max)	P (max)	S (max)	Si (max)	Cr	Ni	N (max)	Tensile min (ksi)	Yield min (ksi)
304	0.07	2	0.045	0.03	0.75	17.5-19.5	8-10.5	0.1	75	30
304L	0.03	2	0.045	0.03	0.75	17.5-19.5	8-12	0.1	70	25

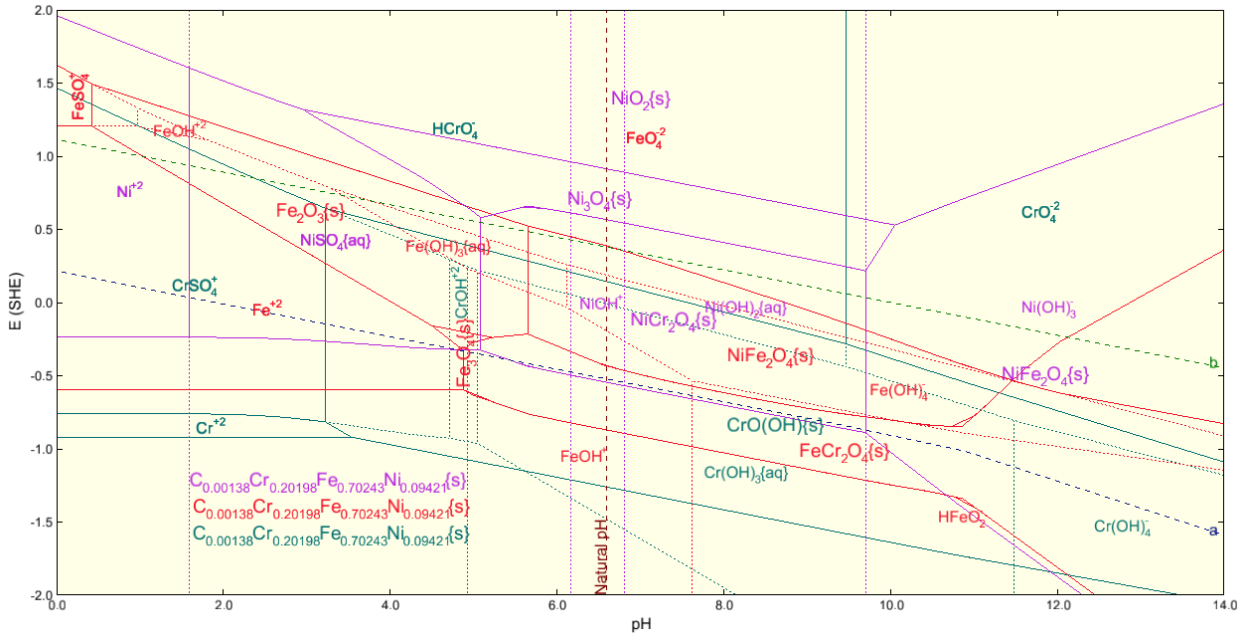

Figure 1: Pourbaix diagram for the Fe-Cr-Ni-O system at 550 °C and 1200 psi generated using OLI software.

CHAPTER 3:
Atom Probe Tomography Characterization of Oxides

3. 1 Background

3.1.1 The technique

In APT, a sharp, needle shaped specimen with an end radius of 50-200 nm is subjected to high fields in order to induce atom desorption or field evaporation. The desorbed atoms are accelerated by the field towards a position sensitive detector. The time of flight of the atom between desorption and detection is directly related to the mass-to-charge ratio due to the kinetic energy of the ionized atom, allowing for the generation of a mass spectrum. After labeling the peaks in the mass spectrum, a volumetric reconstruction of the original specimen is generated, indicating the original position and identity of each atom. This reconstruction can be analyzed to understand the chemistry of the original sample at the atomic scale.

3.1.2 Reconstruction parameters

APT reconstructions are performed using commercially available software called the Integrated Visualization and Analysis Software (IVAS), which relies on a number of assumed parameters about the specimen and the experimental conditions used to collect the data. The specimen geometry is assumed to be that of a cone with a hemispherical cap. The radius of the sphere, R, at the beginning of analysis defines the starting point for the reconstruction, and the geometrical factor, k, is used to account for the fact that the specimen is not a sphere, but a sphere on a cone. R is can be input manually or calculated, while the default k-factor in IVAS is 3.3. The shank angle, α, or angle of the cones sides can also be taken into consideration in the reconstruction. Each of these parameters is specimen dependent, even for the same material. Material parameters are considered in the form of the evaporation field, F, which is defined as the electric field at which the barrier for ionization of an atom is reduced to zero [109]. Values of the evaporation fields have been measured or calculated for most pure metal species [109, 110] and incorporated into IVAS. In reality, however, F further depends on the local surroundings, including properties of neighboring atoms of the same or different species, the local

crystallography, the dielectric constant of the material, in addition to the specimen geometry factors discussed above, and likely changes as the specimen evaporates. These dependencies are the subject of recent research [111], but are not adequately incorporated into the primitive reconstruction methods described here. Experimental conditions are also used in the reconstruction algorithm, including the voltage at which evaporation occurs, V. Finally, the image compression factor (ICF) is used to define the point from which projection of the atom off the surface towards the detector occurs [109]. For an ICF of 1, the reconstruction would assume a radial projection geometry, while for an ICF of 2 it would be a stereographic projection. In other words, the image compression factor changes the magnification factor used to relate the positions of atoms in original specimen to where they hit the detector. The default ICF used by IVAS is 1.6.

3.1.3 Reconstruction methods

The default reconstruction method in IVAS is performed using the voltage evolution according to [109, 112]:

$$F = \frac{V}{kR} \tag{2}$$

As a specimen evaporates the voltage is increased in order to maintain a constant evaporation rate of the specimen. The voltage evolution method uses the instantaneous voltage, along with a defined field and k-factor to calculate an instantaneous radius for the specimen apex. The default field is that of the most abundant element in the mass spectrum. The x and y positions of the atom in the reconstruction determined based on the instantaneous radius and the ICF according to the equations:

$$x = \frac{X_D * ICF * R}{L}, y = \frac{Y_D * ICF * R}{L} \tag{3}$$

where X_D and Y_D are locations of a detection event on the detector, R is the radius, and L is the effective distance between the specimen and the detector. The z position is determined based on the sequence of the detection event using an incremental value [109, 112].

This method has been used extensively in the literature. However, despite its widespread use, it must be accepted that the reconstructions generated using this method may be physically inaccurate due to use of an estimated field value, changes of field throughout data acquisition or within regions of the specimen, and unknowns in determining the actual geometric factor and

ICF. These factors can be readily apparent when reconstructions are performed using this method for specimens that cross regions of drastically different evaporation fields [113, 114]. For instance, an increase in the necessary evaporation field will necessitate an increase in voltage to maintain the desired evaporation rate, causing a jump in the voltage curve. If reconstructed using a constant field method, the resulting reconstruction will show a physically inaccurate increase in radius related to the increase in voltage. However, chemical data within each region should be largely unaffected, while interfacial information may be skewed.

In order to avoid this type of artifact induced by a field change within a single specimen, or to reduce assumptions on specimen geometry, an alternative method known as a shank angle reconstruction can be performed [109]. In this method, the software forces the reconstructed volume into a cone shape with a specified shank angle and starting radius. Instead of calculating an instantaneous radius, the radius is chosen based on the definition of the shank angle. Ideally, the shank angle is measured based on scanning electron microscopy (SEM) or TEM before evaporation, to incorporate some level of physical meaning. However, it is well accepted that the actual analyzed volume is only a subset of the original tip volume due to field of view limitations within the atom probe. Thus, forcing the shank angle to match that of the original specimen likely over-represents the analyzed volume, introducing a different form of physical inaccuracy. Forcing the shank angle also has the potential to obscure chemical information at the interface by artificially stretching or compacting it. However, this can be the most appropriate method for layered materials where the layers have different evaporation fields, and additional information about the field, specimen, or material properties is unknown.

Other reconstruction methods may be used based on additional data that may be available in order to increase the physical accuracy of reconstructed volume. For instance, in well behaved materials such as some pure metals the detection histogram reveals the pole pattern and zone lines due to trajectory aberrations induced by the evaporation characteristics related to the original crystallographic structure of the specimen [115]. The reconstruction can be performed according to Equation (2) and Equation (3), but with additional adjustment of the k-factor and ICF to ensure that the plane spacing and angle between poles in the desorption map matches the physical characteristics of the crystal. This can be performed if at least 3 poles are present in the map, and results in a reconstruction that is more physically accurate [115]. Unfortunately, such high resolution information is typically lost in alloys or oxides.

Other forms of additional information may also be obtained to help in determining adequate reconstruction parameters in the absence of such high resolution information. For instance, TEM imaging of the specimen before and after the experiment allows for accurate measurement of the initial and final voltages and the shank angle. Such imaging can also reveal features, such as grain boundaries, phase boundaries, or precipitates, that can be matched in the reconstruction by adjusting the reconstruction parameters [116, 117]. Reconstruction parameters can also be adjusted to obtain uniform axial and radial density within the reconstruction [118]. While uniform density is a valid assumption for single phase materials, it does not guarantee accuracy of the reconstruction, and should be used in conjunction with additional data if possible. There have recently been approaches to improve the accuracy of the reconstruction protocols by incorporating dynamic parameters [119], using different point projection models [120], or using hybrid methods, but these are outside the scope of the current work.

3.1.4 Difficulties with the study of insulators using APT

Originally the high fields necessary for evaporation was induced by voltage pulsing of conducting materials, limiting the application space of the technique. More recently laser pulsing has been utilized to induce high fields by what is generally accepted as largely thermal mechanisms [121], allowing for the analysis of semiconducting and insulating materials, such as oxides. However, it is well established that in the analysis of oxides the acquired composition is deficient in oxygen compared to the expected stoichiometry [122-124], making phase identification and precise chemical measurements particularly difficult when the "right" answer is unknown.

Off stoichiometry in insulators and semi-conductors has been related to a number of inter-related mechanisms including ion dissociation [125-127], detector dead zone loss [128, 129], neutral ions [122, 125, 127], mass spectrum overlap issues [124], and multihits [128-130]. Mass spectrum overlap, particularly of oxygen peaks, could result in oxygen loss depending on the peak assignment. For instance, the peak at 16 Daltons (Da) could be labeled O^{+1} (mass 16 / charge +1) or O_2^{+2} (mass 32 / charge +2), but the former assignment would attribute half as many O atoms to the peak as the later. It is generally accepted that the 16 Da peak is O^{+1} based on experiments conducted on oxides fabricated with O_{18} [124] and prediction of the charge stage ratios of both oxide species indicating the likelihood of O_2^{+2} is low [127].

However, the most prevalent loss of information results from multihits, or instances when multiple ions hit the detector at very similar times. Multihits are prevalent in the study of oxides and other high field materials using laser pulsing atom probe [128-130], and thus significant work has been done to understand what causes them and how they affect the data. They can arise from (1) atoms on different portions of the tip evaporating from the same laser pulse, (2) a clustered ion evaporating and dissociating into two or more ions in-flight, or (3) an extra atom evaporating after the laser pulse, but before the next pulse. In scenario (1) the atom is most likely detected and accounted for correctly in the reconstruction, because the spacing between the events is sufficient for the detector to distinguish them. However, in scenario (2) the dissociated ions can hit the detector very close to each other in time and/or space, such that the hits cannot be adequately distinguished [129]. The region where such information is lost is referred to the detector dead zone, which can be measured for its spatial and temporal limits. Dissociation can also result in neutral ions, which are not properly accounted for in the mass spectrum. Finally, in scenario (3) the "late" atom can end up as background noise because its time of flight is measured to be longer than its actual time of flight, and thus it is not placed correctly in the mass spectrum.

3.1.5 Methods to better understand or reduce oxygen loss

Preferential loss of a certain element in studies of insulators and semi-conductors is an area of intense recent interest, due to the otherwise high resolution and chemical sensitivity of APT [126-128, 131, 132]. There are two complementary routes to address such loss: (1) limit the phenomena that lead to loss, such as dissociation and multihits, by careful selection of analysis parameters, or (2) recover the lost information by additional analysis of the collected data.

There are a couple methods that can be used to decrease losses associated with multihits. One method is to coat the oxide material with a conductive metal layer [132]. This has been shown to increase the rate of heat dissipation of the tip after an incident laser pulse, thereby reducing delayed evaporation and resulting in increased mass resolution, ultimately resulting in better quantification for oxides [132]. As mentioned previously, another method is by careful selection of analysis parameters. Laser energy in particular has been shown to have a significant effect on multihit prevalence and resulting chemistry measurements [130, 133]. By performing calibration experiments over a range of laser energies, detection rates, and base temperatures the

dependencies of multihit prevalence can be determined and analysis parameters selected to minimize their effects.

Additionally, some methods have been utilized in order to "recover" lost information. The most prevalent of these is analysis of the "dissociation tracks" present in the correlation scatter plot representing the dissociation of a molecular ion into daughter ions that result in a multihit on the detector. These dissociation tracks are obvious in analysis of multihits from specimens run in straight flight path instruments, and can be measured and quantified, allowing for "lost" data to be added back into composition measurements [128]. Dissociation of molecular ions has also been implicated in the formation of neutral species, such as N_2 or O_2, which can also be visualized in the dissociation tracks of specimens analyzed using a straight flight path instrument [127, 134]. However, in reflectron containing machines, such as the one used in this work, dissociated ions may be deflected outside the field of view by the reflectron, or continue in a straight flight path in the case of neutral molecules, so dissociated ions are not observed in the correlation scatter plot, making their impact on the measured stoichiometry impossible to quantify. However, analysis of other multihits, such as those appearing in thermal tails or due to late evaporation may still be possible.

3.1.6 Purpose

In the subsequent chapters APT has been used as a tool for analyzing oxides that form during high temperature aqueous corrosion of 304 SS, resulting in oxides with varying compositions of Fe, Cr, and Ni. Unfortunately, analysis in these atom probe specimens is rarely straightforward, due not only to the factors discussed above for studying oxides, but additionally due to the combination of multiple metals ions (Fe, Cr, Ni), with varying evaporation characteristics, all being incorporated into the oxide to various degrees. In order to gain a better understanding of how the analysis conditions affect chemical composition measurements, and what features observed in atom probe results are real or artifacts of the technique, the following study on relatively pure oxide samples similar to those observed in the aqueous corrosion process was conducted. These experiments provided valuable insight into the interpretation of chemical data obtained from the oxides grown on multicomponent alloys in the subsequent sections.

3.2 Materials

Five different oxide species related to oxides expected after elevated temperature aqueous corrosion of 304 SS were chosen to understand their evaporation behavior and the resulting

stoichiometry dependencies and reconstruction parameters. The oxides studied were FeO, Fe_2O_3, Fe_3O_4, Cr_2O_3, and $FeCr_2O_4$. F_2O_3 in the form of centimeter size pieces, and FeO in millimeter size pieces was obtained from Sigma Aldrich, both with reported purity of 99.8%. Millimeter size pieces of Fe_3O_4 used as an evaporation material was purchased from Stanford Advanced Materials with 99% purity. Cr_2O_3 was ordered from the Kurt J. Lesker company in the form of millimeter size pieces with reported purity of 99.9%. Finally, bulk mineral samples of $FeCr_2O_4$ were purchased from Ward Scientific. As a naturally occurring mineral this material contains a high degree of impurities in the form of Al and Mg. SEM images showing the grain size and structure of each oxide are shown in Figure 2. It should be noted that the grain structure of these purchased oxides did not match those of oxides observed after high temperature aqueous corrosion experiments. This is mostly likely due to the means in which the oxides are fabricated.

3.3 Experimental

APT specimens were fabricated using the site specific liftout technique [135] on a Helios 650 Nanolab or Nova 250 Nanolab dual beam SEM/FIB equipped with an Omniprobe micromanipulator. A variety of experiments were performed on each oxide using a Cameca LEAP 4000X HR equipped with an ultrafast UV laser and a reflectron lens in order to determine the dependency of measured composition on different experimental parameters. Data analysis was performed using IVAS 3.6.12. A baseline reference run was conducted at moderate operating conditions expected to result in high yield. The conditions for the baseline run were a base temperature of 50 K, a laser pulse energy of 50 pJ, a pulse rate of 200 kHz, and a detection rate of 0.005 atoms per pulse. This allowed for comparison of the mass spectra for each oxide, and provided a dataset to understand the multihit prevalence and laser heating affects for each material. Then changes were made in laser energy, temperature, or detection rate every ~1 million ions on the same specimen to determine the dependency of the results on the parameter of interest. Finally, correlative TEM and APT were performed on tips from some of the oxides to get a better understanding of the field characteristics and reconstruction parameters necessary for accurate volumetric reconstruction. TEM images were obtained on a JOEL 2010F TEM and analyzed using Gatan Digital Micrograph. Table 2 shows which experiments and analyses were performed for each of the five oxide samples.

3.4 Results

3.4.1 Baseline measurements

The overall measured chemistry from the baseline runs is reported in Table 3. Additionally, shown in Figure 3 are the mass spectra obtained from these baseline runs with the main peak groups labeled. As can be seen, iron oxide species typically evaporate as molecular species O_2, FeO, FeO_2, FeO_3 in addition to atomic species Fe and O, with various charge states. No obvious significant differences in the prominent evaporation species were observed from the different oxide materials tested. Figure 3b shows the two Cr containing oxide materials, and again reveals evaporation of molecular CrO, CrO_2 and CrO_3 in addition to atomic species. In the $FeCr_2O_4$ sample both CrO_x and FeO_x species were observed, but no peaks corresponding to mixed $FeCrO_x$ species were observed. This material also had a large amount of impurity elements including Al and Mg, and associated AlO and MgO peaks, as expected due to the relative impurity of the original mineral sample.

3.4.1.1 Oxygen deficiency

One artifact of the APT technique that was observed in these materials was an oxygen deficiency compared to stoichiometric oxygen content. In addition to the measured chemistry, Table 3 shows the percent deficiency of the measured oxide composition compared to the stoichiometric composition. Oxygen deficiency was calculated using the equation:

$$\%O\ Deficiency = \left|\frac{O_{stoichiometric} - O_{measured}}{O_{stoichiometric}}\right| * 100\% \quad (4)$$

The results show that all of the oxide species, with the exception of Cr_2O_3, exhibited significant oxygen deficiency at the baseline conditions. Iron oxide species all had greater than 30% oxygen deficiency, while mixed $FeCr_2O_3$ had ~12%. However, based on the measured stoichiometry, the oxide species, particularly the three different iron oxides, could still be distinguished from each other, as they exhibited unique measured Fe and O levels.

As will be shown in the next section, the oxygen deficiency can be minimized to an extent through careful selection of analysis conditions. However, an effort was undertaken to understand the source of the oxygen deficiency observed under the baseline conditions by

analyzing the multihit prevalence. Table 4 reports the percentage of single hits and mulithits detected for each oxide species, along with the oxygen deficiency previously recorded in Table 3. A clear correlation between increasing percentage of multihits, with increasing percentage of oxygen deficiency can be seen. The potential source of such multihit loss can be observed using a correlation scatter plot [128], and by visualizing the detector dead time [129], both shown in Figure 5 for Fe_3O_4. The correlation scatterplot shows the 2^{nd} order multihits (2 simultaneous hits) as the mass-to-charge ratio of the first hit versus the mass-to-charge ratio of the second hit. In this plot, high density regions show ions that are often correlated with each other. Vertical and horizontal collections of points show ions evaporated sometime after the laser pulse, but are likely part of the same species as the high density region they originated from. Diagonal tracks represent the same pair of ions, both of which evaporated after the laser pulse. In the mass spectrum, ions in these tracks are recorded as background noise because they appear at mass-to-charge ratios that are not representative of the actual ion. For instance, one of the highest density points in Figure 5a occurs at (32, 72) corresponding to evaporation of O_2^{+1} as the first hit and FeO^{+1} as the second hit in a multihit event. There is a horizontal, vertical, and diagonal track extending from this high density point. The vertical track likely represents additional O_2^{+1} molecules that evaporated after the initial laser pulse, or dissociated during flight, and will be plotted in the mass spectrum at their respective measured mass-to-charge ratio instead of at 32 Da. The horizontal track represents the same for FeO^{+1}, while the diagonal track represents additional pairs of O_2^{+1}, FeO^{+1} atoms that evaporate late. Each of these will be plotted incorrectly in the mass spectrum, becoming background noise that will be missing from the quantification. The same is true for each set of vertical, horizontal, and diagonal tracks. Visual analysis of the correlation scatter plot reveals that nearly every oxygen containing species detected in the mass spectra contributes to multihits, while the metal ions have little to no multihit signal, providing evidence that multhits are related to the measured oxygen deficiency.

Additional information is completely lost in the detector dead zone, a region in time and space where two hits cannot be distinguished from each other, and are counted as only one hit [129]. Molecular ions that originate from the same point on the sample and are of similar mass are likely to hit the detector very close in time and space, and thus are lost, while species of different masses that evaporate at the same time arrive farther apart in time due to their different kinetic energies. By plotting the distance in time and space of 2^{nd} order multhits the detector

dead zone was measured to be approximately 3 ns and 12 mm, meaning ions that evaporate within 3 ns of each other, and hit the detector less than 12 mm apart, are only counted as a single hit. The amount of signal lost to this dead zone, however, is difficult to determine.

3.4.1.2 Laser shadowing

Another artifact observed in the baseline experiments was laser shadowing, or a difference in detection rate or detected species on the side of the specimen that the laser is incident on, compared to the opposite side [124]. Laser shadowing can be immediately recognized by the difference in number of detected ions across the detector histogram, as shown in Figure 4a. The result, in terms of measured evaporation species and overall measured chemistry can be observed in the composition profiles presented in Figure 4b and c obtained from Fe_2O_3 across the specimen from laser side to shadow side (as shown by the arrow in Figure 4a). Overall oxygen measurements tend to be slightly higher on the shadow side compared to the laser side, with the exception of $FeCr_2O_4$, as shown in Table 5. This affect can result in differences in measured chemistry by 1-2% in different regions of the reconstruction. While this is important when considering precise chemical measurements obtained using APT, the small differences observed across the tip here were significantly less than the overall oxygen deficiency and the specimen to specimen variation observed in the multi-component oxides measured in the future sections. Thus, it was not considered to play a major role in the overall measured oxide compositions, and was largely ignored.

Overall oxygen deficiency, and spatial variation in measured chemistry due to laser shadowing, both exist in the analysis of oxides using laser pulsing atom probe, and thus must be considered during analysis under these conditions. Laser shadowing, although obvious, was deemed to not be significant enough to warrant further investigation, based on the chemical variation observed between specimens of the same material reported in future sections. Regarding oxygen deficiency, interestingly, not all of the studied oxides were equally prone, with the Cr containing oxides exhibiting significantly less oxygen deficiency than the Fe species. The oxygen deficiency was correlated to the prevalence of multihits for the material. Even so, the different oxide species were distinguishable from each other based on differences in the measured stoichiometry. However, the evaporation conditions that lead to high yield (low rate of fracture), such as high laser energies, especially in specimens that contain oxide/metal interfaces, are those that also exacerbate the issues of multihit loss and laser shadowing.

3.4.2 Measured chemistry dependence on analysis conditions

As already alluded to, the measured chemistry of APT specimens can vary based on the analysis conditions used by changing the laser/material interaction with respect to the artifacts discussed above. In general, the change can be attributed to changing the evaporation field applied to the specimen. For instance, in setting the laser pulse energy the base voltage will also be set in order to achieve the desired detection rate. By lowering the pulse energy, the base voltage, and thus evaporation field, will need to be increased to obtain an equal detection rate. Similarly, by increasing the desired detection rate at constant laser energy, the base voltage will also be increased, indicating a similar increase in applied evaporation field. In general, increased evaporation field is associated with a decrease in multihits compared to single hits, and is thus expected to result in closer to stoichiometric measurements. To understand how these dependencies apply to the oxide species of interest here, the analysis conditions were varied compared to the conditions used for baseline runs discussed previously and the resulting chemistry measurements were analyzed for trends.

3.4.2.1 Laser pulse energy dependence

Laser pulse energy dependency experiments were performed for all of the oxide samples. Typically the range of pulse energies explored were 0.5 pJ to 80 pJ. In some cases the lower pulse energies could not be reached without sample fracture. Approximately 1 million ions were collected at each analyzed pulse energy. The order of pulse energies was chosen to avoid a linear increase or decrease in pulse energy which may have resulted in compounding effects between the pulse energy and the tip radius. A 1-dimensional concentration profile down the tip axis was created from a cylindrical region down the center of the reconstructed volume, with the radius of the cylinder set to encompass nearly the entire volume. Variations in metal and oxygen ion compositions were used to identify the regions of different pulse energies, as shown ionically for Fe_2O_3 in Figure 6. The measured composition at each pulse energy was then determined by averaging the composition of the concentration profile within each segment after breaking down molecular ions into their respective atomic constituents. Graphs of pulse energy versus measured metal and oxygen composition for each oxide are shown in Figure 7 along with the stoichiometrically expected composition. FeO, Fe_2O_3, and Fe_3O_4 each exhibit closest to stoichiometrically correct compositions at the lowest pulse energy tested, and a decrease in measured oxygen and increase in measured Fe with increasing pulse energy. For Fe_2O_3, nearly

correct stoichiometry is achieved, while for FeO and Fe_3O_4, even at 0.5 or 1 pJ, respectively, the stoichiometry is still oxygen deficient by several atomic percent. In addition, the M:O ratio levels off at ~50 pJ for FeO and Fe_2O_3, but continues to diverge all the way to 80 pJ for Fe_3O_4. Conversely, Cr_2O_3 exhibits near stoichiometric M:O ratios over the range of pulse energies from 10 pJ to 50 pJ (and consistently fractured at lower pulse energies). $FeCr_2O_4$ also exhibits little variation in the measured stoichiometry with changing pulse energy, but is consistently oxygen deficient by a few atomic percent.

3.4.2.2 Base temperature dependence

In traditional voltage pulsing experiments on conducting metals decreasing the base temperature usually increases the mass resolution of the mass spectrum. The effect of base temperature in laser pulsing, where the evaporation is induced by raising the tip temperature with the laser, is less clear. A test of the base temperature dependence was performed on a single tip from FeO using a pulse energy of 50 pJ and a detection rate of 0.5%. The temperature was varied from 20 K-100 K and ~1,000,000 atoms were collected at each condition. A 1-dimensional concentration profile along the tip axis of the reconstruction shows no variation in measured stoichiometry. Therefore, base temperature has no significant effect on the measured chemistry. This suggests that the temperature rise induced by the laser during laser pulsing experiments is more than 80 K, which is consistent with predictions of temperature rise in oxides made previously [124].

3.4.2.3 Detection rate dependence

Detection rate calibration over a range of 0.5 – 5% (5-50 atoms per 1000 pulses) was conducted on one FeO tip at 50 K and 50 pJ pulse energy. Detection rate calibration was attempted on other oxide species, but the specimens tended to fracture at the second or third increase in detection rate, indicating a decrease in yield associated with the higher field conditions. The results for FeO are shown in Figure 8. As the detection rate was increased, the measured oxygen came closer to the expected stoichiometry, and the molecular ion evaporation rate was decreased. However, the changes were only very slight. Thus, raising the detection rate is not an effective method to increase the field in order to reach the expected stoichiometry due to the marginal changes, and the increased risk of fracture.

3.4.3 Reconstruction by correlative TEM/APT

As mentioned previously, correlative TEM/APT has been used as a method to gather additional information about the specimen, including the shape (radius and shank angle) and the presence of features (grain boundaries, interfaces, precipitates) that can be used to adjust the reconstruction parameters [116, 117]. In this method, TEM images of the specimen are collected before and after APT evaporation, allowing for direct measurement of the initial voltage, final voltage, and analyzed Z-depth. This information can be used to generate a reconstruction that matches the physical parameters of the tip instead of using one of the default methods mentioned earlier.

Correlative TEM/APT was attempted on the pure oxide specimens studied here in an attempt to provide additional understanding of how to properly reconstruct oxide containing specimens, such as by calculating the evaporation field of the oxide material based on the shape and applied voltage, and determining the reconstruction parameters that result in uniform density profiles and accurate shapes. Furthermore, it also provided an evaluation of the technique on relatively easy to prepare samples in order to determine if such a method should be employed for more complex samples that contain multiple oxide species and interfaces, such as those in the following work.

An example of the results obtained using correlative TEM/APT is provided in Figure 9 from the FeO material. Figure 9a shows the TEM images obtained before running the tip, after an initial run of ~500,000 ions, and after a subsequent run of 8 million ions. The reconstruction using default parameters, along with the measured axial and radial density, are shown in Figure 9b. This reconstruction clearly is physically inaccurate based on the TEM images, despite the flat axial and radial densities, indicating that density alone is not adequate to ensure reconstruction accuracy. Finally, an adjusted reconstruction is shown in Figure 9c, along with axial and radial density measurements. For the adjusted reconstruction a fixed shank angle was used based on calculating the shank ankle, α, required to give the measured initial and final radii and z height, according to the equation:

$$\alpha = tan^{-1}\left(\frac{R_{final} - R_{initial}}{Z + R_{final} - R_{initial}}\right) \quad (5)$$

After adjusting the reconstruction parameters, a better fitting reconstruction, still with flat density profiles is obtained. It should be noted, however, that the calculated shank angle does not match that which would be measured from the TEM image, due to the fact that the analyzed volume is a subset of the original volume due to field of view limitations of the instrument.

The evaporation field of the oxide material can be estimated instead of using the default field for Fe, the most prevalent atomic species detected. The calculated field for FeO was 25.0 V/nm at the beginning of the run and 20.4 V/nm at the end of the run (assuming k=3.3). An average field of ~23 V/nm could be applied for future runs of this oxide, and should provide a better reconstruction than default parameters. This field is less than the theoretical field of Fe (33 V/nm), but still the same order of magnitude of fields for other metal species. Unfortunately, this oxide was not one of the oxides observed on the samples obtained after aqueous oxidation experiments, so this calculated field was not utilized. Furthermore, additional correlative samples of the other pure oxide samples were attempted, but in most cases they failed during APT after TEM imaging. This may be due to contamination of the specimen during TEM imaging combined with the fact that the other oxides were small grained materials that exhibited many grain boundaries within each tip, making them more fragile to begin with. Unfortunately this method is time consuming and drastically reduces yield even under moderate analysis conditions, so it was abandoned for further use in the following chapters.

3.5 Discussion

The above results indicate even the study of relatively pure oxides using laser pulsing atom probe is a complex matter. However, they did reveal a number of trends that can be used to help analyze the less ideal oxides discussed in the following chapters.

3.5.1 Selection of analysis parameters

Two considerations must be made in selecting the analysis parameters for oxide materials: yield and stoichiometry. Ideally analysis conditions should be chosen to optimize the stoichiometry with respect to the expected stoichiometry, particularly if the real composition is known. In all of the oxide materials studied here, the real composition was approached by running under conditions that increased the field and decreased the effects of multihits and molecular ion evaporation. The most effective way to achieve this for iron oxides was to decrease the pulse energy to very low levels, in the range of 0.5-1 pJ. Even under such conditions the measured stoichiometry only approached, but did not reach the expected stoichiometry for

the iron oxide species studied. In contrast, the chromium oxide materials in general exhibited measured stoichiometry more similar to the expected stoichiometry, including higher measured oxygen content. This was attributed, in general, to less multihit evaporation even at higher pulse energies. Furthermore, the chromium oxide chemistry measurements were essentially independent of pulse energy. Increasing the detection rate, at constant pulse energy, also increased the applied evaporation field, and resulted in closer to stoichiometric measurements. However, the changes in measured stoichiometry were more subtle than those achieved by decreasing the pulse energy, and accompanied by an increased rate of fracture particularly at high detection rates. By these criteria alone, analysis parameters for oxide materials should be low pulse energy and moderate detection rate, and the multihit percentage should be monitored and minimized.

Unfortunately, yield must also be considered. In this case yield refers to the likelihood of premature fracture of the specimen, resulting in short runs (few collected ions) or loss of information (such as what is happening at the oxide/metal interface). In the pure oxide specimens analyzed here yield generally was unaffected over the range of pulse energies studied, with the exception of Cr_2O_3, which repeatedly fractured at conditions below 10 pJ. The other specimens typically evaporated with no issues down to at least 1 pJ, allowing for a set of good conditions that give reasonable stoichiometries. Increased detection rate even to 1% (from 0.5%) also routinely resulted in fracture in all of the materials that exhibited small grain size. Yield was also reduced for specimens that were imaged using TEM for correlative analysis. Since the detection rate did not have a huge effect on the measured stoichiometry, 0.5% was deemed acceptable. Unfortunately, when low pulse energy conditions were attempted for oxides grown in high temperature water, premature fracture was routinely observed. This was attributed to presence of multiple interfaces (oxide/oxide and oxide/metal interfaces) often observed in the multi-layer structured oxides of these materials. For these reasons, pulse energy of 50 pJ was generally used because it gave acceptable yield, despite the less than ideal stoichiometric measurements.

3.5.2 Oxide behavior with non-ideal analysis parameters

Despite the fact that conditions used for analysis in subsequent sections were non-ideal in that they were not optimized to obtain the closest to correct stoichiometry, the laser energy dependency experiments on pure oxides provide some insight into the results obtained at these

non-ideal conditions. At 50 pJ, the laser energy used in subsequent analyses, the measured composition for most of the oxide species has essentially plateaued. Each oxide exhibits a unique measured composition distinguishable from the other oxides. For instance, FeO has measured oxygen content of 36±1%, while in Fe_2O_3 it is 51±1% and in Fe_3O_4 it is 47±1%. The measured Fe content in these materials is 64±1%, 50±1%, and 53±1%, respectively. For Cr oxide species the oxygen and metal contents are close to stoichiometric. Educated guesses of the phase of a particular oxide region can therefore be made based on upon these results, although the two most likely iron oxide species (Fe_2O_3 and Fe_3O_4) exhibit pretty similar properties. Therefore, additional characterization techniques, such as Raman spectroscopy and electron diffraction were utilized to aid in identifying the oxide species, when applicable.

3.5.3 Application to the interpretation of APT data from aqueous oxides

The results outlined in this chapter were used as a baseline for the subsequent analysis of oxides formed on 304 SS after high temperature aqueous exposures in the following chapters. These conditions are expected to result in a two layered oxide with a nanocrystalline mixed spinel ($FeCr_2O_4$) adjacent to the metal, and an outer magnetite (Fe_3O_4) layer. An example specimen, exhibiting a two layered oxide obtained from inside a crack mouth exposed to high temperature deaerated water, is shown in Figure 10. APT was performed at the same conditions used for the pure oxide baseline runs, namely 50 pJ pulse energy, 50 K temperature, 200 kHz pulse rate, and 0.5% detection rate. The reconstruction was performed using the default voltage evolution method in the absence of any additional information on specimen shape or evaporation field. The reconstruction exhibits the inner oxide spinel at the apex in blue, and two adjacent "outer oxide" particles with different Ni contents on the bottom in pink. The measured stoichiometry of the right grain of the outer oxide in Figure 10 is 51.4% Fe, 1.5% Ni, 1.0% Cr, and 45.9% O. Adding the metal contributions together, given this is not a high purity oxide, the measured stoichiometry is 53.9% metal and 45.9% O. This clearly mostly closely aligned to the composition of Fe_3O_4 obtained at a pulse energy of 50 pJ, as expected for this oxide. The same relationship holds for the left grain despite the different Ni level.

The inner, mixed oxide has a measured composition of 29.7% Fe, 16.4% Cr, 2.2% Ni, and 2.4% Mn, or total metal content of 50.7%, and oxygen content of 49.1%. The measured metal to oxygen ratio in this case is clearly different than that obtained from the mineral sample of $FeCr_2O_4$. However, it is even farther from the measured stoichiometry of Cr_2O_3, the other

likely Cr-rich oxide that could exist. As noted previously, the mineral sample had Al and Mg impurities, and was crystalline as opposed to the expected nanocrystalline structure of the aqueous grown oxide. Both of these factors may play a role in the differences in measured oxide composition, and were unfortunately unavoidable. This trend was observed to varying degrees in the subsequent work for Cr-containing oxides.

3.6 Conclusions and perspectives for subsequent work

These APT results obtained on relatively pure oxides provide useful insight that was used in subsequent analysis of oxides grown on multicomponent alloys in high temperature water in regards to interpreting the measured stoichiometry and the best methods to use for reconstruction.

Clearly, the conditions chosen for APT analysis can have a dramatic effect on the quantification results for the oxide species of interest in this work. However, in many cases, no set of analysis conditions can give the true, or expected, values due to inherent problems with material-laser interactions in this technique. Furthermore, the conditions that give the most accurate results also lead to decreased yield. Thus, it is important to understand how the measured stoichiometry may relate to the actual stoichiometry for materials where the resulting oxide is not necessarily known. By studying ‘pure’ known oxides under a variety of conditions a good understanding of the relationship between conditions and resulting measured stoichiometry has been achieved. Ideally, running oxide specimens under high field conditions such has high detection rate or low laser energy reduces the multihit percentage, and ultimately results in closer to real measured stoichiometries. This appears to be most relevant for iron oxide species, while chromium oxides were near-stoichiometric independent of the analysis conditions. For non-ideal analysis conditions, the measured oxygen content, however, can be used to estimate the oxide identity since each oxide exhibited a unique metal to oxygen ratio. Thus, for practical reasons related to increasing the specimen yield, a majority of the samples analyzed in the rest of this work were run under less rigorous conditions, usually 50 pJ pulse energy, 50K temperature, and 0.5% detection rate. Oxide identification was made using the results of this chapter, and combined with additional analysis techniques such as Raman spectroscopy.

Reconstruction parameters must also be considered. This work showed that correlative TEM/APT could be successfully used to adjust the reconstruction parameters to achieve a more physically accurate reconstruction than that obtained using the default methods. However, it also

showed a significant decrease in yield when this technique was attempted. Furthermore, the evaporation field was calculated (for an assumed k-factor) for FeO, but since the analysis was not successfully performed on specimens of other species, estimation of the evaporation fields were not available for the oxide species that were observed in subsequent analyses. Additionally, density based reconstructions could not be employed in subsequent work due to the presence of interfaces across which uniform density is not guaranteed. In any case, it was shown that density based methods should be combined with additional information in order to be meaningful. Due to these limitations, the subsequent work was primarily analyzed by utilizing the default reconstruction methods, based solely on voltage evolution or forced shank angle. While overall the image of the resulting reconstruction cannot be assumed to be physically accurate, the chemical information gathered from each region should still be meaningful. Scale bars, however, both in the images and in the composition profile graphs, should be considered only estimates.

Table 2: Pure oxide APT analyses

Analysis	FeO	Fe_2O_3	Fe_3O_4	Cr_2O_3	$FeCr_2O_4$
Reference Run	✓	✓	✓	✓	✓
Laser/Shadowing Effect	✓	✓	✓	✓	✓
Multihit Analysis	✓	✓	✓	✓	✓
Pulse Energy Dependence	✓	✓	✓	✓	✓
Detection Rate Dependence	✓				
Temperature Dependence	✓				
Correlative TEM/APT	✓				✓

Table 3: APT measured stoichiometry and oxygen deficiency at baseline analysis conditions

Oxide	Metal (At%)	Oxygen (At%)	% Oxygen deficiency
FeO	63.8	36.2	43.2
Fe_2O_3	50.4	49.6	34.4
Fe_3O_4	54.3	44.6	38.4
Cr_2O_3	41.1	58.4	5.3
$FeCr_2O_4$	42.9	53.9	11.9

Table 4: Multihit proportions for pure oxides at baseline analysis conditions

Oxide	% Single hits	% Multihits	% Oxygen deficiency
FeO	61.5	38.3	43.2
Fe_2O_3	65.8	34.1	34.4
Fe_3O_4	64.3	35.6	38.4
Cr_2O_3	90.5	9.3	5.3
$FeCr_2O_4$	73.7	26.1	11.9

Table 5: Measured oxygen and metal contents on the laser side versus shadow side obtained by isolating a 10nm diameter cylinder on each side of the detector histogram

Oxide	Laser side		Shadow Side	
	Oxygen	Metal	Oxygen	Metal
FeO	32.8	67.2	33.2	66.7
Fe_2O_3	49.1	50.9	49.9	50.1
Fe_3O_4	44.1	55.9	48.2	51.8
Cr_2O_3	58.6	41.4	59.5	40.4
$FeCr_2O_4$	54.4	45.4	53.4	46.3

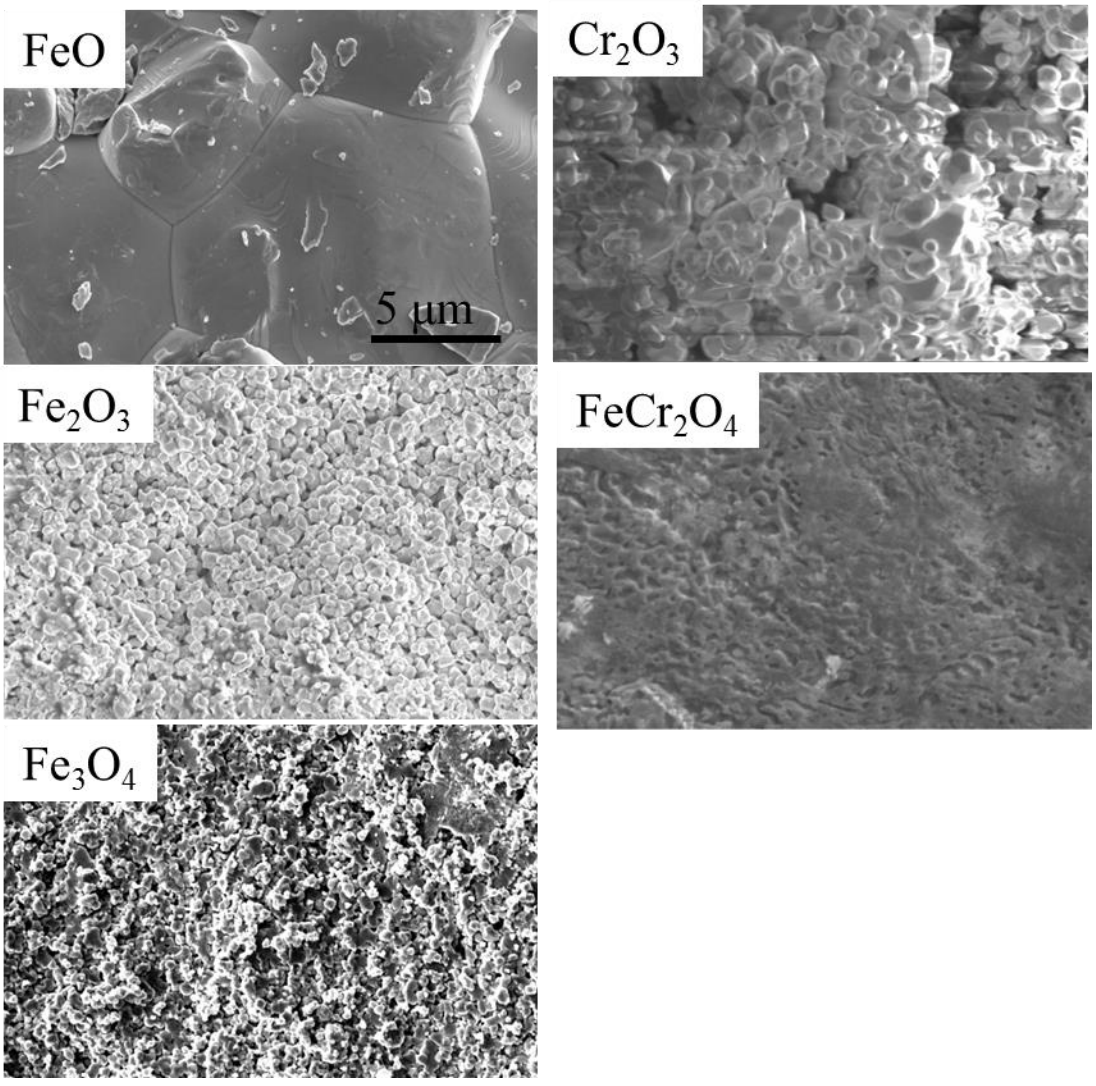

Figure 2: SEM images of the five "pure" oxide structures examined

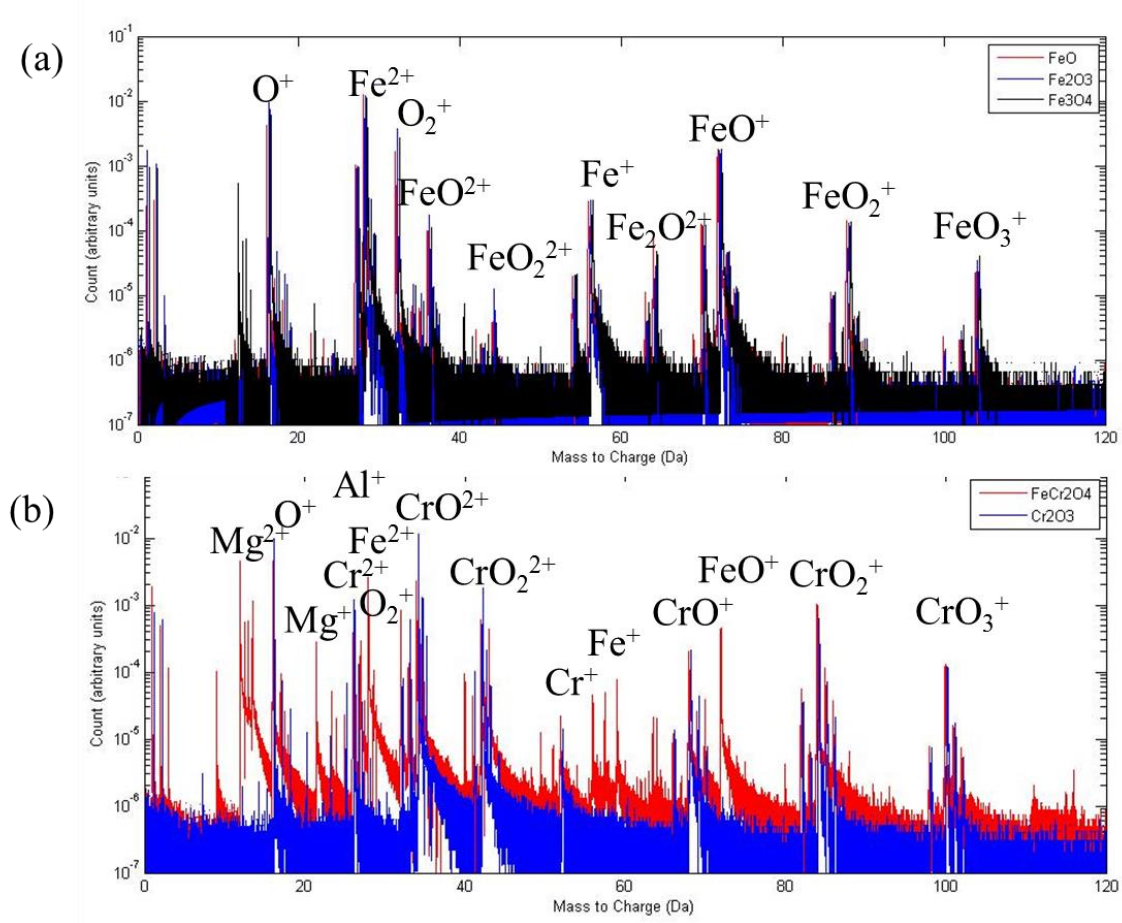

Figure 3: Characteristic APT spectra obtained at 50 pJ laser energy for (a) Fe oxide species and (b) Cr and mixed oxide species.

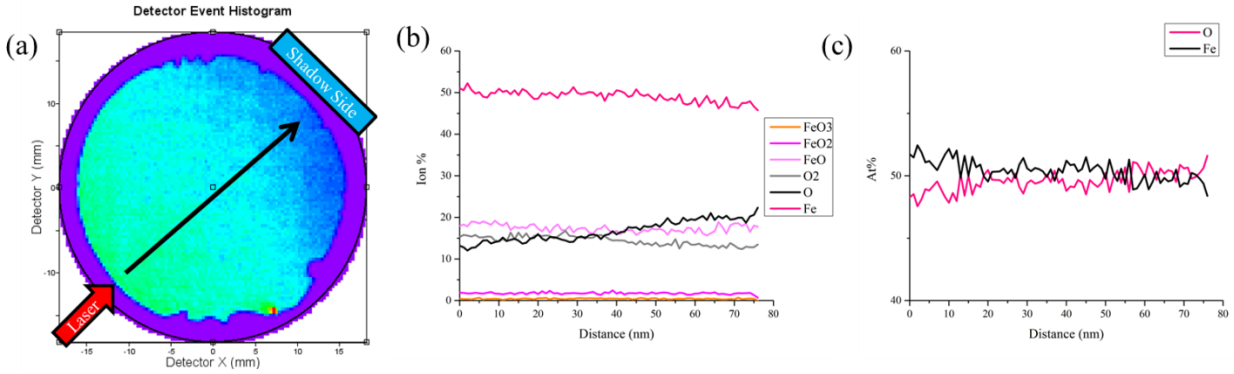

Figure 4: Effect of laser shadowing on measured composition. (a) Detector histogram. (b) Ionic composition along the arrow in (a). (c) Atomic composition along the arrow in (a)

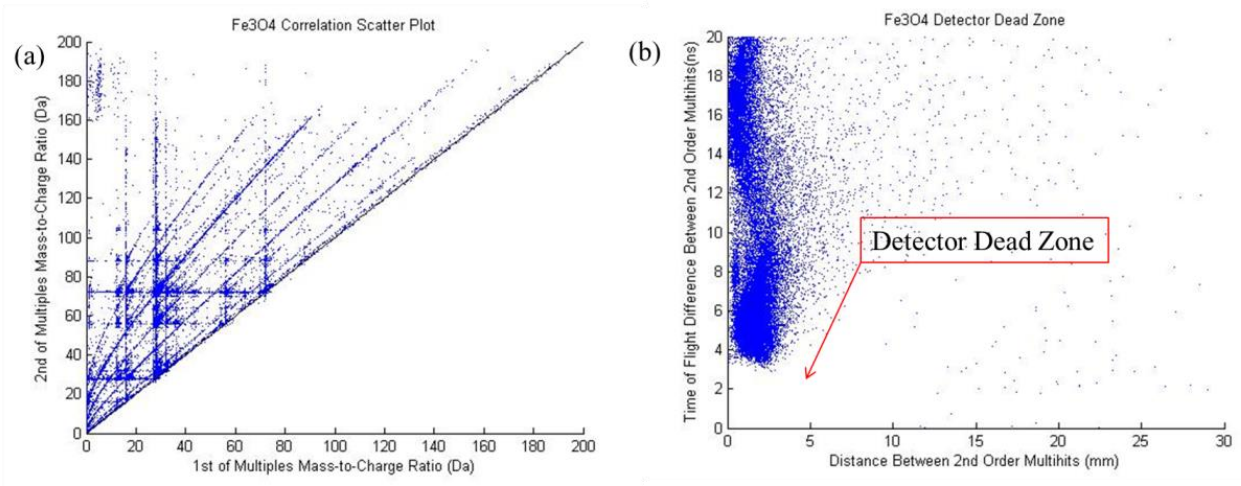

Figure 5: Correlation scatter plot (a) and detector dead zone (b) for Fe_3O_4 second order multihits. Horizontal, vertical, and diagonal tracks in (a) represent likely oxygen loss. The detector dead zone is ~3 ns and 12 mm in size.

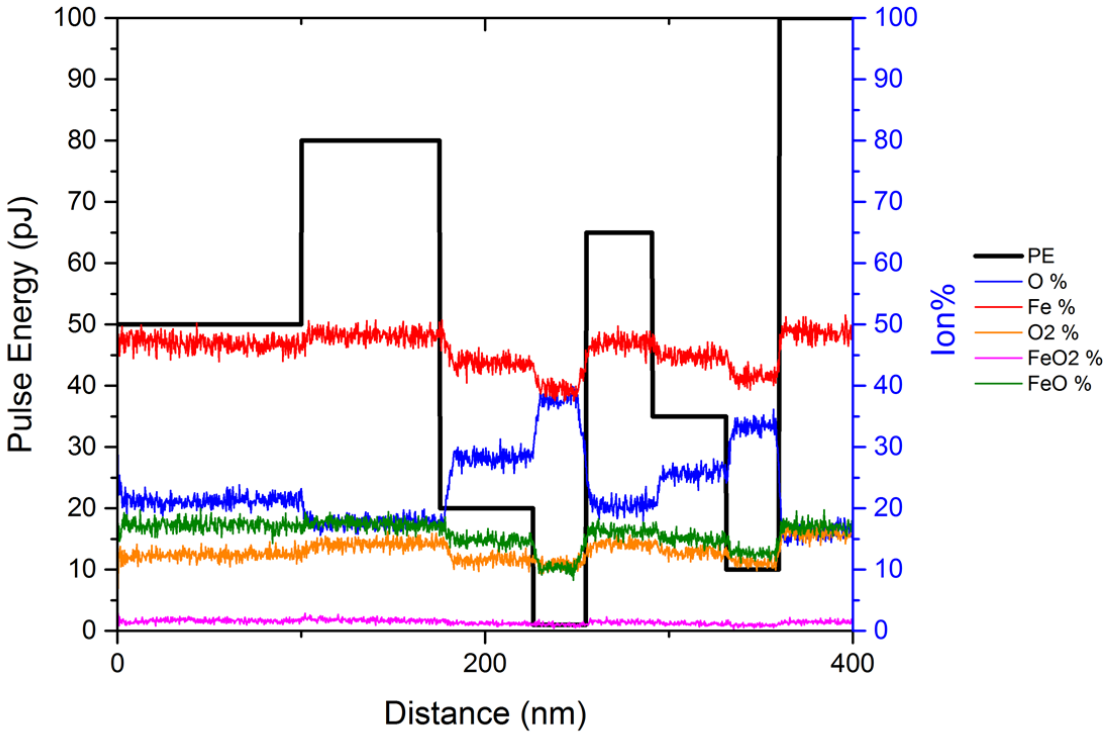

Figure 6: Representative pulse energy calibration curve for Fe_2O_3. The black curve (left axis) is the applied pulse energy and the colored curves (right axis) are the ion percent of the corresponding molecular ion detected by APT.

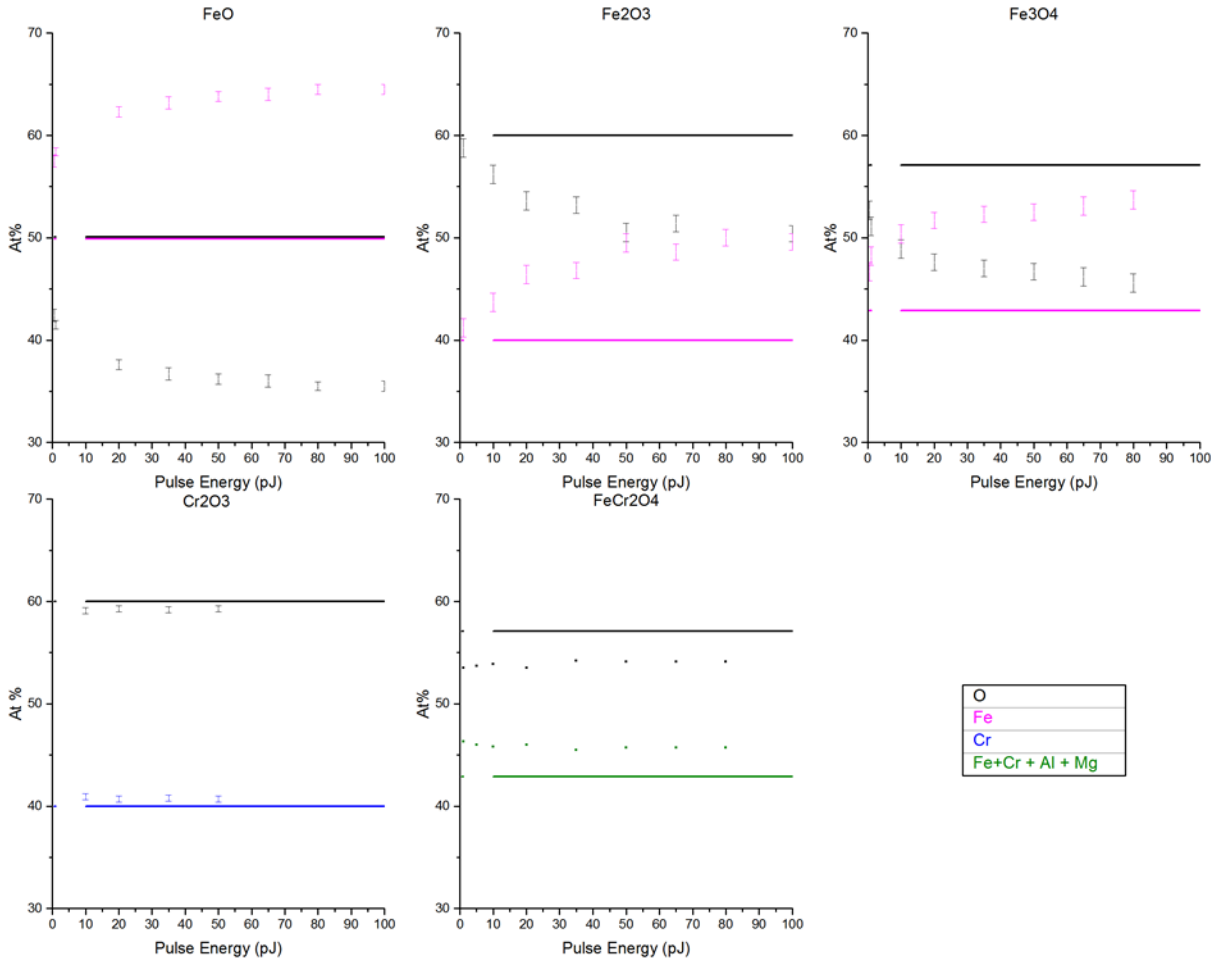

Figure 7: Measured chemistry versus pulse energy for each of the studied oxides. Solid horizontal lines represent the expected stoichiometry, and points with error bars represent the APT measured stoichiometry. In general, APT measurements become closer to expected values with decreasing pulse energy.

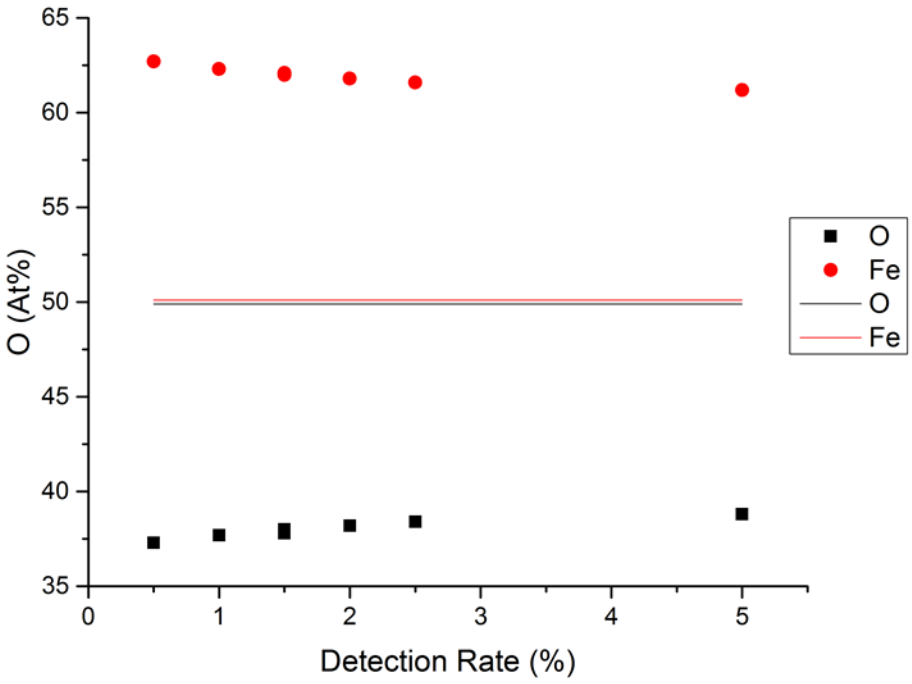

Figure 8: Detection rate calibration performed on FeO. Solid horizontal lines represent the expected stoichiometry, and points represent the APT measured stoichiometry. Increasing the detection rate brings the measured stoichiometry slightly closer to the expected value.

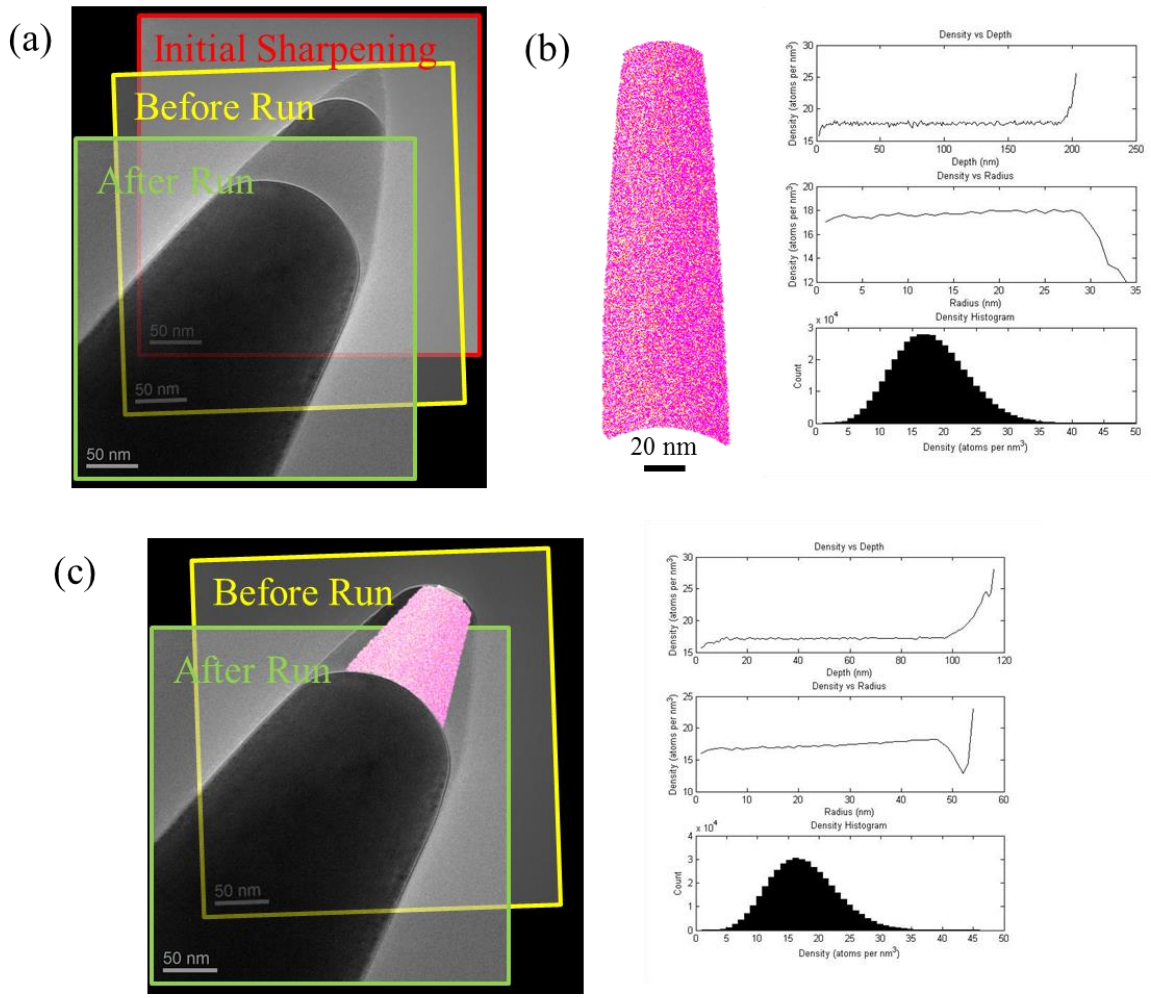

Figure 9: Correlative TEM/APT Results. (a) TEM images of the tip after initial sharpening, after an initial run of 500,000 ions, and after a run of 8 million ions. (b) An APT reconstruction using default reconstruction parameters, and measurements of the axial and radial densities. (c) An APT reconstruction with modified reconstruction parameters based on the information gathered from TEM images, and the corresponding axial and radial density distributions.

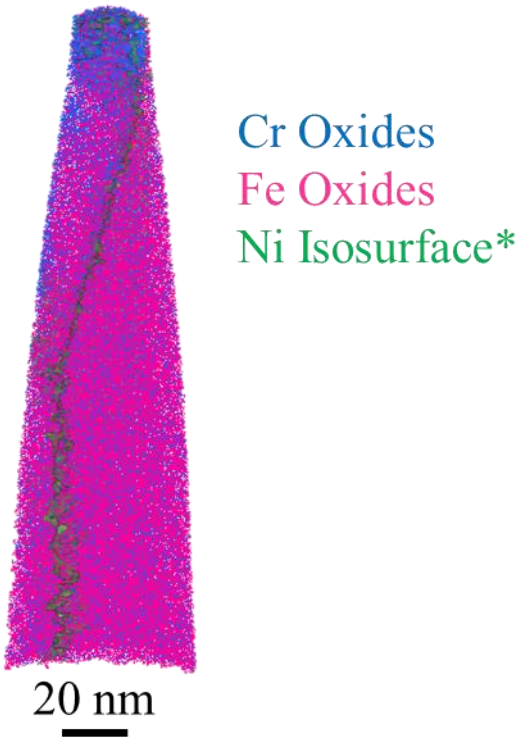

Figure 10: APT reconstruction of an oxide obtained from a corrosion test with two distinct oxide phases, for chemistry comparison to the pure oxides. The Cr-rich oxide phase is shown in blue and Fe-rich oxide phase is shown in pink. *The Ni isosurface delineates two Fe-rich oxide grains that had different Ni levels.

CHAPTER 4:

The Role of Surface Deformation in the Initial Stages of Oxidation of 304 SS in High Temperature Deaerated Water

4. 1 Introduction

Type 304 and 316 SS have been widely incorporated into components of pressurized water nuclear reactors (PWRs) and boiling water nuclear reactors (BWRs), and thus are subject to high temperature aqueous corrosion. Thus, understanding the corrosion processes of 300 series SS in high temperature water has been an area of scientific pursuit for several decades.

In high temperature aerated and deaerated water, a dual layer oxide forms on the surface [3, 8, 11, 14, 17, 18, 20, 22, 28, 136]. The outer layer is composed of discrete oxide particles. In oxygenated water, these particles are a mix of Fe_3O_4 and Fe_2O_3 [3, 8], while in deaerated water the Fe_3O_4 or $NiFe_2O_4$ phase is favored [8, 17, 18, 22, 24]. The inner oxide is a Cr-rich nanocrystalline layer. While it is often reported as a non-stoichiometric M_3O_4 spinel [8, 14, 18, 20, 22], it is sometimes considered to have an M_2O_3 component [8, 24, 26, 28].

The mechanisms by which this dual layer oxide forms are still up for debate. In an aqueous environment oxides can form by either dissolution/precipitation mechanisms, or by solid state reactions [32]. In the case of 304 SS, the inner layer is universally considered to grow by a solid state reaction requiring the diffusion of oxygen to the oxide/metal interface [3, 11, 17, 20, 22, 28, 29, 34, 137]. The outer oxide is reported by many to occur by a dissolution-precipitation reaction [14, 20, 28], while some have concluded it occurs by solid state outward growth at the solution/oxide interface [17, 29]. Evidence for the former includes particles growing on top of one another [3], lack of particles in unsaturated water [20], and apparent correlation with surface roughness [14]. Evidence for the latter includes the fact that all of the metallic cations rejected from the inner oxide appear to be incorporated into the outer oxide film [17]. It is possible that both mechanisms are at play [18], which may depend on additional environmental factors, such as water flow rate [20] or incorporation of dissolution products from the reactor vessel [138].

The role of material deformation in the oxidation process is also still unclear. Several authors have reported a marked decrease in corrosion rate on specimens electropolished or hand

polished to a mirror finish compared to ground or machined surfaces [9, 18, 21, 29] due to the formation of a more uniform, non-porous, protective layer. On the other hand, some authors have concluded that deformation of the surface reduces the corrosion rate [14, 136, 139]. This has been attributed to increased rate of Cr diffusion along deformed regions, resulting in a more Cr-rich protective oxide film, and a commensurate inhibition of Fe and Ni diffusion in the Cr-rich oxide [14, 139]. There have been direct observations of morphological differences in the outer oxide layer depending on the surface condition [14, 17, 18]. However, despite the fact that subsurface deformation is implicated in the role of diffusion of metal and oxygen species, the inner oxide layer formed in this region has been less rigorously studied with respect to the underlying microstructure, with only recent, yet contradictory, emphasis on this topic [21, 136].

The current work aims to better understand the role of surface deformation in the early stages of high temperature aqueous corrosion processes of 304 SS by looking at the oxide products at a local, high resolution scale. SEM and scanning transmission electron microscopy (STEM) imaging was used to characterize the morphology of the oxide layers, while APT provided high resolution three dimensional chemical mapping of the inner oxide layer and the oxide/metal interface. From these observations, mechanisms of oxidation relating to the underlying microstructure are proposed.

4.2 Experimental

4.2.1 Materials

Corrosion coupons of dimensions ½” x ½” x ⅛” (13 x 13 x 3 mm) were fabricated from a heat of annealed 304 SS, with composition shown in Table 6. One side was ground by hand with 220 and 320 grit silicon carbide sand paper, resulting in a rough surface and underlying surface deformation. The opposite side was ground by hand with sequential steps down to 1200 grit sand paper, and then a circular region 1 cm in diameter was electropolished at room temperature in a perchloric acid/acetic acid mixture. The electropolished surface was smooth and adequate material was dissolved to remove the deformation layer induced by grinding. By having both surface finishes on the same specimen, it was assured that the exposure conditions were equivalent for each exposure time.

4.2.2 Exposures

Exposures were conducted in a nickel autoclave for exposure times ranging from ~10 minutes to 72 hours with deaerated water (35 cc H_2/ kg H_2O) at a pressure of 1200 psi and a temperature of 288 °C. The water pH was adjusted to 10 at room temperature such that the 288 °C pH was approximately neutral ($pH_{288\ ^\circ C}$ = 6.2). To accomplish such short exposure times while avoiding environmental exposure during heat up and cool down, the following procedure was developed. The autoclave was purged with nitrogen gas, and then a calculated amount of deaerated water was added to the autoclave. This initial water was heated up such that upon thermal expansion it remained just below the test coupon. Water was then added to submerge the coupon, but the temperature was nearly maintained and actively heated to return to the test temperature. Upon reaching the desired exposure time the water was cooled as rapidly as possible, causing it to contract below the level of the specimen, and drained to minimize further exposure. Level limit indicators were used to monitor the level of the water compared to the sample coupons to ensure that the desired exposure conditions were met. The test apparatus and procedure was tested on one coupon that was never fully submerged to check for oxide growth. Limited oxide growth in the form of surface particles was observed on the surface and confined to circular regions indicative of condensation, but the overall oxide thickness was negligible. An additional specimen was exposed for the minimum amount of time possible (~ 10 minutes) by starting the cool down procedure immediately after submersion to provide a baseline for oxide growth. Subsequent exposures were conducted for 0.5, 1, 4, 56, and 72 hours. Additional samples were oxidized in air for comparisons of the characteristics of the oxide and interfacial segregation, and are discussed in Appendix III. Another sample with a machined surface (significant surface deformation) was oxidized for 3 months to understand the oxide growth after longer time periods, and is discussed in relation to the ground specimens.

4.2.3 Analyses

Raman spectra were obtained using a Renishaw inVia microscope with a 532 nm laser, a laser power of 10, and a minimum of 20 scans on each surface to reduce noise. APT and TEM specimens were fabricated using a site-specific liftout technique [135] on either an FEI Helios 650 Nanolab or FEI Nova 200 Nanolab dual beam scanning electron microscope (SEM)/ focused ion beam (FIB) equipped with an Omniprobe micromanipulator. Scanning TEM (STEM)

images were obtained on a Hitachi HD 2300A STEM operated at 200 kV and used to measure the average oxide thickness on each specimen and examine the morphology of the inner oxide layer. Oxide thickness was measured every 50 nm across the TEM specimen using ImageJ, for greater than 130 measurements per specimen. APT was performed on a Cameca LEAP 4000X HR in laser mode using a pulse energy of 50 pJ, a detection rate of 5 atoms per 1000 pulses, a base temperature of 50 K, and a pulse rate of 200 kHz. Duplicate samples from most oxidation conditions were obtained and used to verify features and determine measurement error.

APT reconstructions and analyses were performed using Cameca IVAS version 3.6.12. Volumetric reconstructions were created using the voltage evolution method. Due to the increase in evaporation field experienced when the specimen reaches the oxide/metal interface, the reconstructions obtained using this method appear bell-shaped. While these are not necessarily accurate representations of the analyzed volumes, in the absence of additional information on the evaporation characteristics of the oxides it was deemed acceptable for the purpose of the current study. However, the scale bars provided in with the reconstructions should be taken with caution and scaling of the oxide and metal phases may differ. During mass spectrum assignment overlapping peaks were checked to determine which element(s) provided the greatest contribution, and labeled as such. Peak deconvolution was performed on select reconstructions to check the validity of this method, and the difference in measured composition between full deconvolution and the method used was never more than 1 at% for a given element. This was deemed acceptable since the specimen to specimen variation in measured composition was typically larger than 1 at% for each major element. Chemical measurements from APT data were made in one of two ways: For large uniform volumes, the region of interest (ROI) was isolated and the bulk chemistry was measured within that ROI. For small regions, proximity histograms (or proxigrams) [140] were made from an iso-concentration surface (where the concentration value was selected to minimize interfacial noise and reported is in the appropriate figure captions) outlining the region of interest and the chemistry was averaged over the flat portions of the proxigam plot. To reduce noise the measurements were made after performing a background correction on the mass spectrum using IVAS. It should be noted that the measured oxygen content was always below the expected stoichiometric value at the laser energy employed. This phenomenon has been noted previously for laser pulsing APT of insulators and semiconductors,

as discussed in Chapter 3. Nevertheless, the measured oxygen content is reported for completeness.

4.3 Results

4.3.1 Surface and cross-sectional imaging

Characterization of the oxide morphology was accomplished using surface and cross sectional imaging. SEM images of the surface, and STEM images of the oxide cross section, after select oxidation times, are shown in Figure 11 and Figure 12 for ground and electropolished surface conditions, respectively. On the ground surface, oxide particles grow in size and number density with increasing oxidation time. The particle size and density observed on the electropolished surfaces are significantly less than those observed on the ground surface through the initial stages of oxidation.

On the ground surfaces, inner oxide penetration varied significantly in the early stages of oxidation, as shown in the phase contrast cross sectional images in Figure 11, resulting in wide standard deviations in the measured thickness. On the other hand, electropolished samples exhibited much more uniform inner oxide thickness (Figure 12), with no additional oxide penetration observed, even at grain boundaries (see 72 hr specimen in Figure 12). After 3 months of oxidation the oxide thickness on machined surface shows much less local variation in thickness (Figure 13a). The inner oxide thicknesses (x) measured from STEM images were used to fit a power law relation with time (t) as shown in Figure 14:

$$x = k_p t^n \tag{6}$$

For the ground surface and electropolished surfaces, the exponent was 0.27 and 0.28, respectively, while the rate constants, k_p were 42 and 9.7 nm/hr, respectively. It should be noted that the relatively low oxide thickness on the 72 hour ground specimen can be attributed to fewer observed areas of deep penetration in the cross section analyzed compared to the other ground specimens. The 56 hour electropolished specimen also exhibited lower oxide growth than expected based on the trends observed otherwise.

4.3.2 Raman spectroscopy

The oxide phases and chemical development were identified using Raman spectroscopy and APT. Raman spectra from each sample are shown in Figure 15, and represents signals from both oxide layers, since complete coverage by the outer layer was not observed in the 72 hour timeframe of the experiments. On the ground samples the peaks at 226, 292, and 409 cm^{-1} are characteristic of hematite (Fe_2O_3). The characteristic peaks for other likely oxide species $FeCr_2O_4$ (683 cm^{-1}), $NiFe_2O_4$ (486 and 697 cm^{-1}), and Fe_3O_4 (665 cm^{-1}) all share the region 660-700 cm^{-1}. On ground specimens this peak broadens with increasing exposure time, indicating the simultaneous presence of multiple of these phases. On electropolished specimens the main peak shifts from left to right, indicating that the chemistry of the spinel phase is shifting from initially magnetite rich towards a nickel ferrite phase.

4.3.3 Atom probe tomography

APT was performed for select immersion times for both the ground and electropolished surfaces with an emphasis placed on capturing the inner oxide layer, and the inner oxide/metal interface.

4.3.3.1 Electropolished specimens

The oxide formed on electropolished specimens was locally uniform in composition for each exposure time, but developed chemically over the time period studied. This can be observed in the volumetric reconstructions of specimens obtained after 1, 4, and 72 hour exposures in Figure 16. 1-dimensional concentration profiles down the tip axis show that the inner oxide films exhibited little to no chemical fluctuation throughout the analyzed depth. The measured composition of the oxide film for each exposure time is reported in Table 7. Some fluctuation in the measured composition existed from specimen to specimen, accounting for the errors reported in Table 7. The oxide is deficient in Fe, and to a lesser extent Ni, compared to the original matrix composition, but the deficiency appears to decrease over time. The oxide/metal interface is enriched in Cu with the Cu concentration and thickness increasing with exposure time. This can be observed clearly in both the reconstructions and 1 dimensional concentration profiles in Figure 16.

4.3.3.2 Ground specimens

In contrast, the specimens obtained from ground surfaces exhibited local fluctuations in the oxide chemistry and penetration of oxygen below the oxide/metal interface, resulting from the deformation microstructure at the surface. This can be seen in the volumetric reconstructions presented in Figure 17, where a blue isoconcentration surface of CrO has been used to separate the oxide regions. (The value of CrO surface was chosen to best represent the interface within each region and is reported in the figure caption). Inside this isoconcentration surface the oxide is Cr-rich, while outside it is richer in Fe compared to Cr, and has more Ni incorporated. The respective average compositions of each region are reported in Table 7, along with the total average composition of the two regions combined. The temporal development of the oxides is seen to proceed by preferential loss of Fe and Ni resulting in the Cr-rich oxide, and then by slower oxidation of the adjacent material with less loss of Fe and Ni. This can be visualized by examining the proxigrams in Figure 17, which measure the composition across the isoconcentration surfaces. They are organized to represent the development of the oxide from least developed (formed earliest) to most developed, and the actual region they were obtained from is indicated by numbered brackets. As oxidation begins the oxidized regions are already starting to be deficient in Fe and Ni, but the adjacent matrix is unaffected. At longer times, additional Fe and Ni are lost from the fully oxidized regions, while the adjacent regions are starting to lose Fe and become oxidized. After 72 hours, both regions have continued to lose Fe and are completely oxidized, resulting in regions of two distinct oxide chemistries. At this point the oxide is nearly fully developed, as little change in the measured stoichiometry is observed even after 3 months of oxidation.

The outer oxide particles are rich in Fe with small Ni and Cr contributions, consistent with the fact that Fe is the primary element depleted from the inner oxide layer. Specimens from both 1 and 72 hours each preserved a portion of the outer oxide particle at the specimen apex, as can be seen at the top of both reconstructions in Figure 17. The measured composition of these particles is similar after both oxidation times, and is shown in Table 7. The measured oxygen deficiency compared to stoichiometric magnetite has been discussed in Chapter 3.

The characteristics of the oxide/metal interface also differ from the electropolished specimens, in that Ni is observed to be enriched at the interface, while Cu segregation in this region, while present, is at significantly lower levels. As seen in Figure 17, the interface was

largely lost in the 1 hr and 3 month specimens, but regions below the actual interface still exhibit Ni and Cu enrichment. The interface was captured in the 72 hour specimen and shows that Cu and Ni were both present, albeit discontinuously at the oxide/metal interface. The Cu enrichment for this specimen only reached levels of ~ 3 at% compared to 40 at% in the electropolished 72 hour specimen, while Ni enrichment reached levels of ~50 at% in some areas.

4.4 Discussion

The oxide products between the two surface conditions appear different, necessitating differences in the diffusion processes occurring. However, the literature provides us with some starting points to understand the oxidation process. First, it is universally accepted that the inner oxide layer grows inwardly such that the top of this layer is the original metal surface [3, 11, 17, 20, 22, 28, 34, 137]. This is supported by the current results and can especially be observed in the electropolished case, where a smooth interface is observed at the top and a wavy interface is observed at the bottom (Figure 12). Significant variations in the oxide thickness of ground specimens (Figure 11) also points inward growth by oxygen penetration.

The thermodynamically stable oxide phases for the test environment can be predicted from a Pourbaix diagram, and are a mixed spinel structure (Figure 1). The spinel structure takes the form AB_2O_4 where A is composed of divalent cations, and B is trivalent cations. The thermodynamically stable compositions for the immiscible spinel phases F_3O_4 and $FeCr_2O_4$ at 260 °C are $Fe(Fe_{0.85}Cr_{0.15})_2O_4$ (or $Fe_{2.7}Cr_{0.3}O_4$) and $Fe(Fe_{0.35}Cr_{0.65})_2O_4$ (or $Fe_{1.7}Cr_{1.3}O_4$) based on the fact that magnetite (Fe_3O_4) is an inverse spinel, while $FeCr_2O_4$ is a normal spinel, so a full solid solution does not exist [18, 30]. Ni is most likely to replace Fe in the divalent 'A' positions.

The diffusion coefficients for relevant species in the oxide and metal layers are available to varying degrees. In a spinel oxide lattice the relative rates of diffusion are determined by the lattice site (octahedral or tetrahedral) preference such that the diffusion rate follows the following order:

$$D_{Fe}^{+2} > D_{Ni}^{+2} \gg D_{Cr}^{+3} \quad (7)$$

This is because Fe can diffuse in either octahedral or tetrahedral sites, whereas Cr prefers octahedral sites [29, 141]. The filling of octahedral sites by Cr slows the diffusion rate of other

elements [22]. Furthermore, the diffusion of oxygen anions through the oxide lattice is slower than metal cation diffusion [18, 29].

Diffusion in the matrix must also be considered. The bulk and GB diffusion coefficients for Fe, Cr, and Ni were extrapolated from higher temperature data and are reported in Table 8. The general trend for both bulk and GB diffusion is

$$D_{Ni} > D_{Cr} > D_{Fe} \quad (8)$$

At the test temperatures and durations of the current tests, bulk diffusion, and even GB diffusion are not expected to be significant. However, deformation imparted by grinding is likely to increase the local diffusion rate of both metal cations and oxygen anions by short circuiting the bulk or GB diffusion pathways through the introduction of vacancies and/or dislocation pipelines [142, 143].

Finally, the electrochemical nobility must be considered to determine the preference of metal species to oxidize. This can be quantified by the electrochemical potential, and in most negative potential (easiest to oxidize) to least negative (hardest) follows the following order for the relevant species:

$$Cr^{+3} > Fe^{+2} > Ni^{+2} > Cu^{+2} \quad (9)$$

However, because this oxide is formed in high temperature water, the stability of the resulting oxide must also be considered, as discussed previously.

4.4.1 Electropolished specimens

4.4.1.1 Oxidation process

The oxide chemistry observed on electropolished specimens is depleted significantly in Fe, and somewhat in Ni compared to the original matrix composition, while Cr is at or above the level of the matrix. No concentration gradient of any species exists within the oxide layer, or in the matrix underneath the oxide/metal interface (Figure 16). These observations are consistent with a mechanism governed by the flux of oxygen to the oxide/metal interface to react, and where the metal cation egress from the reacting interface to solution is sufficiently fast. The depletion levels of Fe and Ni is consistent with their respective diffusion rates in the oxide (Equation (7)), as is the rate limiting step being the diffusion rate of oxygen. This is shown schematically in Figure 18a where the length of the arrows corresponds to the relative diffusion

rates in the oxide layer. While the process is shown in two steps, both steps are actually occurring simultaneously to various degrees.

4.4.1.2 Copper

A question that remains is the source and role of Cu observed at the oxide/metal interface. Measurements of the surface chemistry after electropolishing, but before oxidation, performed using x-ray photoelectron spectroscopy and Auger spectroscopy confirmed that no Cu was present. Additionally, measurements of the water chemistry during testing revealed only ppb levels of Cu, suggesting that it was not a contaminant in the water. Finally, the presence of Cu was confirmed by performing EDS measurements on TEM lamella to preclude the possibility of it being an artifact of APT. Thus, the Cu is suspected to come from the material itself.

Cu in 304 SS has been observed to accumulate on the surface due to selective dissolution of less noble elements during anodic polarization experiments [144]. Furthermore, due to its high electrochemical nobility it is expected that Cu would resist oxidation, and thus may be rejected from a growing oxide layer, as has been used to explain Ni rejection during oxidation in similar environments [25]. However, the levels of Cu measured were in excess of what would be found due to rejection of Cu from the oxidized matrix of the measured thickness. To verify this, the number of copper atoms, N_{Cu}, observed in circular region from the center of each specimen was counted and corrected based on the detection efficiency of the LEAP 4000X HR using the equation:

$$N_{Cu} = \frac{N_{Cu}^{Measured}}{0.36} \tag{10}$$

The total number of atoms of steel necessary to provide N_{Cu} was then calculated based on the overall composition of Cu in the material (0.14 at% from Table 6):

$$N_{atoms} = \frac{N_{Cu}}{0.0014} \tag{11}$$

N_{atoms} was then constrained to a cylindrical volume (V_{total}) of the same diameter (d) used to measure N_{Cu} from the APT reconstruction, assuming an FCC lattice with 4 atoms per unit cell and a lattice constant of 0.36 nm in order to calculate a depth of matrix necessary to provide the measured Cu atoms:

$$depth = \frac{V_{total}}{A} = \frac{V_{unit\ cell} N_{unit\ cell}}{\frac{\pi d^2}{4}} = \frac{0.36nm^3 \left(\frac{N_{atoms}}{4}\right)}{\frac{\pi d^2}{4}}$$

$$= \frac{0.36nm^3 * N_{atoms}}{\pi d^2} \quad (12)$$

This depth was consistently higher than the measured inner oxide thickness, and thus Cu was assumed to be provided by a matrix dissolution – Cu rejection process, where the calculated depth in equation (12) was the dissolution depth, and the dissolution rate was determined based on the calculated depth and the exposure time, as shown in Figure 19. The necessary dissolution ranges from about 350 nm of dissolution in the first hour of exposure, to about 2 um of dissolution after 72 hours. The dissolution rate decreases with increasing exposure time, indicating that the dissolution slows as the oxide film grows. While this provides a potential explanation for the observation of Cu at the oxide/metal interface, it could not be validated by measuring dissolution in another way, such as weight loss of the specimen or quantification of metal species in the water after testing. Furthermore, the supposition of enhanced dissolution is at odds with previous results suggesting that metal cations are completely incorporated into the two oxide layers [17, 18].

Despite the uncertainty in the source of such high levels of Cu, the implications of Cu enrichment at the interface, regardless of the source, can still be discussed. As an electrochemically noble element that is not easily oxidized, the accumulation of Cu at the interface would inhibit the diffusion rate of oxygen to react at the oxide/metal interface. As the oxygen supply to the interface is slowed, so is the necessary egress of metal cations. This slowing of the oxidation rate is likely responsible for the increase in Fe incorporated into the oxide, and the stoichiometric development towards a thermodynamically stable composition of $(Fe+Ni)_{1.7}Cr_{1.3}O_4$ [18, 30]. Additional experimentation has been proposed in Chapter 7 to clarify the source and role of Cu in the oxidation process.

4.4.2 Ground surfaces

The oxide observed on ground surfaces was much more complex and cannot be described by a simple diffusion rate argument. This is due to the presence of short circuit diffusion pathways imparted by grinding that may increase the diffusion rate of metal cations in the metal

matrix to relevant levels even at the temperature studied and/or the diffusion rate of oxygen anions in the metal. Based on the 1 hour oxidation period that shows sub-interface oxidation, selective oxidation of Cr is now apparent (Figure 17). The network of oxidized Cr-rich fingers suggests oxygen diffusion occurred preferentially in these regions, likely due to the underlying deformation microstructure. Similar, more developed, regions are apparent in the top of the 1 hr specimen, and in the 72 hour and 3 month specimens. The oxide is very rich in Cr, yet still contains some Fe and Ni components. Thus, it is unclear if this is a spinel or chromia type structure. Comparison with the oxide compositions of model oxides in Chapter 3 might suggest it is more similar to Cr_2O_3 in that it has a relatively high measured oxygen concentration, which would be consistent with previous results on deformed surfaces [14, 139].

As Cr-rich oxides form along fast diffusion pathways by selective oxidation, Fe and Ni are either rejected to the nearby matrix, or diffuse through the oxide layer to the oxide/solution interface according to their relative diffusion rates (Fe faster than Ni). This process leaves pockets of Fe-rich regions that oxidize more slowly than their Cr-rich counterparts, in a mechanism likely similar to that observed on electropolished specimens – rate limited by oxygen ingress to the unoxidized region by normal diffusion through the oxide. Indeed, the oxide in this region is similar in chemistry to the oxide observed on the electropolished specimens, albeit slightly less deficient in Fe. This is also approaching a thermodynamically stable oxide composition when Fe and Ni are considered together. This process is shown schematically in Figure 18b where the length of straight arrows corresponds to the relative diffusion rate, and curved arrows representing diffusion in or rejection to the matrix by the mechanisms discussed above. Again, the while the process is depicted in two steps, they are actually occurring simultaneously.

The details of this oxidation process are supported by measurements of the overall oxide composition of the ground specimen (both Cr-rich and Fe-rich combined) compared to the electropolished oxide. After 1 hour of oxidation the combined oxide composition is richer in Fe and less rich in Cr than the electropolished specimen, but this may be due to the inclusion of regions of only partially oxidized metal in the measurement. However, after 72 hours the combined oxide composition is richer in Cr and more deficient in Fe and Ni than the oxide layer on the electropolished specimens. This supports the mechanisms of selective oxidation of Cr and rejection of Fe and Ni, either to the oxide/metal interface or to the oxide/solution boundary.

Differences also exist at the oxide/metal interface of ground specimens compared to electropolished ones. While Cu is still found at the oxide/metal interface, it is in discontinuous pockets and only reaches a few atomic percent. These levels are consistent with rejection from the oxide for the measured oxide thicknesses. Ni rich pockets are also observed at the oxide/metal interface when the interface was preserved (72 hour specimen in Figure 17) and in the matrix below the specimen (3 months in Figure 17). As discussed, Ni pockets could result from rejection of Ni from the Cr-rich oxide [25, 95, 145] or instead could represent areas depleted of Cr due to its to selective oxidation [38, 136]. The composition at the core of the Ni-rich region (measured on the 72 hour specimen) reaches nearly 60 at% Ni and is depleted in Fe to 40 at%, and fully depleted of Cr. The current results fail to provide evidence of one mechanism over the other.

4.4.3 Outer oxide

The composition of the outer oxide was only measured from particles observed on the ground surface, and was consistent with magnetite with some Ni incorporation based on the results from Chapter 3. This is also consistent with the Raman spectra, which exhibited a broad peak over the region that encompasses both Fe_3O_4 and $NiFe_2O_4$ for ground specimens, and a peak that shifts from Fe_3O_4 to $NiFe_2O_4$ for electropolished specimens. While small hematite peaks were seen in the Raman spectra of most of the ground specimens, and one of the electropolished specimens, they do not seem to be a main component of the outer oxide layer. Hematite has been noted as the primary outer oxide product in oxygenated water [3, 11], while magnetite is typically reported for deoxygenated water such as in this work [17, 18, 22]. The presence of hematite on both specimens after the short immersion time may suggest some oxygen remained in the autoclave despite the nitrogen purge.

The thickness of the outer oxide layer could not be satisfactorily measured using the same technique used for the inner oxide, due to wide variation in the coverage of outer oxide particles, as can be seen in Figure 11 and Figure 12. Qualitatively, however, the coverage was greater on the ground specimens than on the electropolished specimens, at least through the initial stages of oxidation. Previous results have suggested that the outer oxide layer should be the same thickness as the inner oxide layer, based on the volume expansion (Pilling-Bedworth) ratio upon

transitioning from metal to spinel oxide [22]. However, this assumes all of the rejected metal cations are incorporated into the outer oxide film.

There is still debate over the mechanism by which the outer oxide forms, between precipitation from solution and outward solid state growth. Based on the mechanisms described previously accounting for Cu at the oxide/metal interface, precipitation from solution would be expected to be greater on the electropolished specimens if significant dissolution did occur. On the other hand, a solid state growth mechanism would be expected to relate to the amount of oxidation occurring beneath the original surface. However, no direct correlation between outer oxide particle location and underlying oxide penetration could be made in this work, despite previous findings that related surface roughness with particle nucleation [14].

Regardless of the mechanism of outer oxide particle formation, this layer is largely considered not to have an effect on the overall oxidation response of the material [17, 20]. Indeed, complete coverage of the surface is never achieved, as can be seen from the specimen oxidized for 3 months in Figure 13, so solution supply to the inner oxide surface is never limited. For this reason, no additional emphasis was placed on determining the formation mechanism of the outer oxide layer in this work. However, experiments to clarify the mechanism of outer oxide growth are discussed in Chapter 7.

4.4.4 Kinetics

The processes described above have implications on the kinetics of the overall oxide growth. Oxide growth in the thick oxide regime (> 2 nm) is typically considered to occur according to a parabolic rate law (Equation (1)) [146]. Indeed, such a rate law has been measured experimentally for similar metal-environment systems [17, 21, 28]. Parabolic growth is observed when the oxidation phenomenon is diffusion controlled. However, in cases of impeded ionic mobility approximately cubic rate laws of the form:

$$x = k_p t^{0.33} \tag{13}$$

have been speculated [20, 33]. In the current results, the oxide thickness of the inner layer only was measured and determined to follow approximately cubic kinetics (Figure 14), consistent with the rate being limited compared to diffusion control. Based on the mechanisms proposed above, it is deduced that oxygen supply to the oxide/metal interface is the rate-limiting step, which may be a result of the low oxygen content in the water or impeded mobility in the oxide

film. It should be noted that large variation existed in the thickness measurements due to the measurement technique, resulting in a relatively poor overall fit for both rate equations, which may also affect the estimation of kinetic parameters. However, given the results that were obtained, the rate constant was lower for oxidation of electropolished surfaces than the oxidation of ground surfaces at commensurate oxidation times. This is likely due to the presence of fast diffusion pathways in the ground specimens that allow oxygen to travel faster through the metal during the early stages of oxidation, or the slowing of the oxidation process by the Cu layer, as discussed previously. While the outer oxide layer thickness could not be accurately determined with the method used herein, doubling the measured thickness for each exposure time (assuming complete incorporation and Pilling-Bedworth ratio of 2.1, as discussed previously) would only affect the rate constant, and not the exponent, in the rate law. The observed kinetics, then, are consistent with the proposed mechanisms of oxidation over these very short time periods.

4.5 Conclusions

APT and TEM were used to study the morphology and chemistry of the inner oxide film formed on ground and electropolished surfaces during exposure to high temperature deaerated water.

1. Consistent with some previous literature, the growth rate was found to be higher on ground specimens than electropolished specimens. In the current work, growth rate was only considered in terms of the thickness of the inner oxide layer. However, qualitatively, the outer oxide particles were larger and more numerous on ground specimens than on electropolished specimens.
2. The high chemical resolution of APT revealed significant differences in the structure of the inner oxide film between different surface conditions. On ground specimens, two regions of distinct chemistry have been found within the oxide. This was attributed to enhanced diffusion of O by short circuit pathways created during deformation, resulting in initial growth of a Cr-rich oxide by selective oxidation. Subsequent growth resulted in a mixed Fe/Cr oxide filling in the adjacent unoxidized regions.
3. On electropolished specimens the oxide film was uniform in composition and thickness, distinguishing it from ground specimens. This was attributed to growth limited by

diffusion of O in the absence of short-circuit pathways. Slower moving Cr and Ni cations were incorporated into the oxide film to a greater extent than faster moving Fe cations, which were lost from the inner oxide.

4. The oxide/metal interfacial chemistry also differed dramatically between surface conditions. On electropolished surfaces the oxide chemistry was consistent with the diffusion rates of the different alloy species through the oxide layer, while Cu was rejected to the oxide/metal interface. Cu enrichment was speculated to be the result of enhanced dissolution during the initial stages of exposure coupled with its high electrochemical nobility. On ground surfaces selective oxidation of Cr occurred first along short circuit diffusion pathways, resulting in the rejection of Ni and Fe to adjacent regions that oxidized more slowly according to a mechanism similar to that observed for electropolished specimens. The deformed microstructure promoted rejection of Ni by the fast growing oxide, or increased diffusion of Cr for selective oxidation, resulting in Ni enrichment at the oxide/metal interface.
5. Additional experiments to understand the source and role of Cu in the oxidation of polished specimens are warranted and will be discussed further in Chapter 7.
6. Enhancements to the previously understood mechanisms of oxidation were proposed to incorporate the different structures observed in the inner oxide film depending on the underlying deformation structure.

Table 6: Composition of 304L SS used in this study

B	S	P	Co	C	Cu	N	Mo	Mn	Si	Ni	Cr	Fe
<0.0005	0.0025	0.025	0.05	0.019	0.14	0.051	0.35	1.6	0.40	9.5	18.3	68.6

Table 7: APT measured oxide compositions of the electropolished and ground specimens after select exposure times (at%)

		1 hr				4 hour				72 hour			
		O	Cr	Fe	Ni	O	Cr	Fe	Ni	O	Cr	Fe	Ni
EP	Inner Oxide	47.4±3.4	33.2±3.3	11.6±5.0	5.4±2.2	53.4±1.9	26.3±1.2	13.6±1.2	4.9±0.2	53.1±0.2	22.1±0.7	15.9±0.5	8.4±0.5
Ground	Inner Oxide 1 (Fe-Rich)	41.4±9.4	15.9±4.2	34.8±10.2	5.1±1.6	-	-	-	-	51.9±3.7	19.1±2.6	20.8±6.4	7.0±3.8
	Inner Oxide 2 (Cr-Rich)	52.8±1.1	34.5±3.1	9.1±2.1	1.4±0.1	-	-	-	-	54.9±0.6	35.1±1.0	6.2±2.0	1.8±0.3
	Inner Oxide (Combined)	47.7±3.1	23.8±0.3	21.6±0.6	3.5±0.4	-	-	-	-	54.1±2.0	29.0±3.9	10.3±3.4	4.6±2.6
	Outer Oxide	42.9	3.3	49.3	3.6	-	-	-	-	44.1±1.1	3.2±0.2	47.6±3.5	4.9±2.2

Table 8: Extrapolated GB (D_{gb}) and volume (D_v) diffusion coefficients at 275 °C

	D_{gb} (cm^2/s)*	D_v (cm^2/s)
Fe	1.4E-15 [147]	4.1E-25 [147]
Cr	3.9E-14 [148]	2.17E-24 [147]
Ni	3.9E-13 [149]	1.0E-24 [149]

*GB width assumed to be 5E-8cm

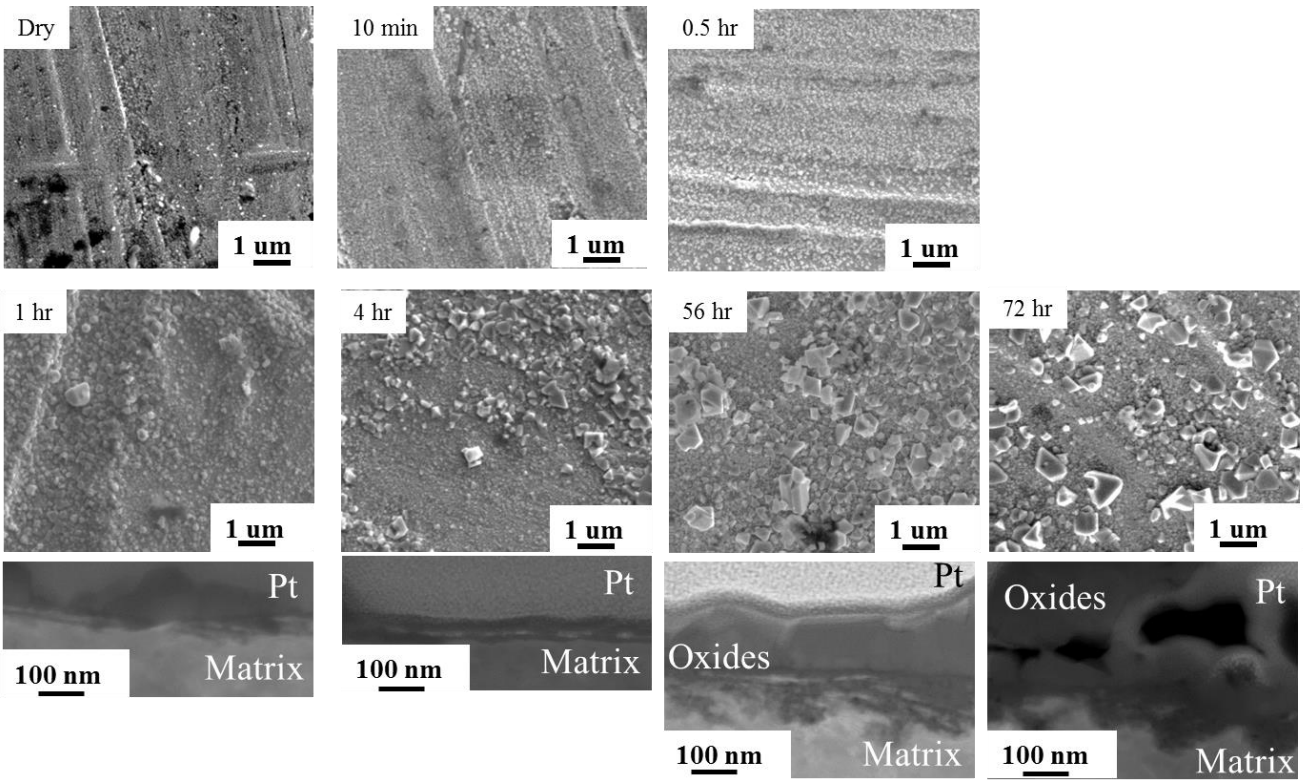

Figure 11: SEM surface images and STEM cross section images of ground surfaces after select oxidation times

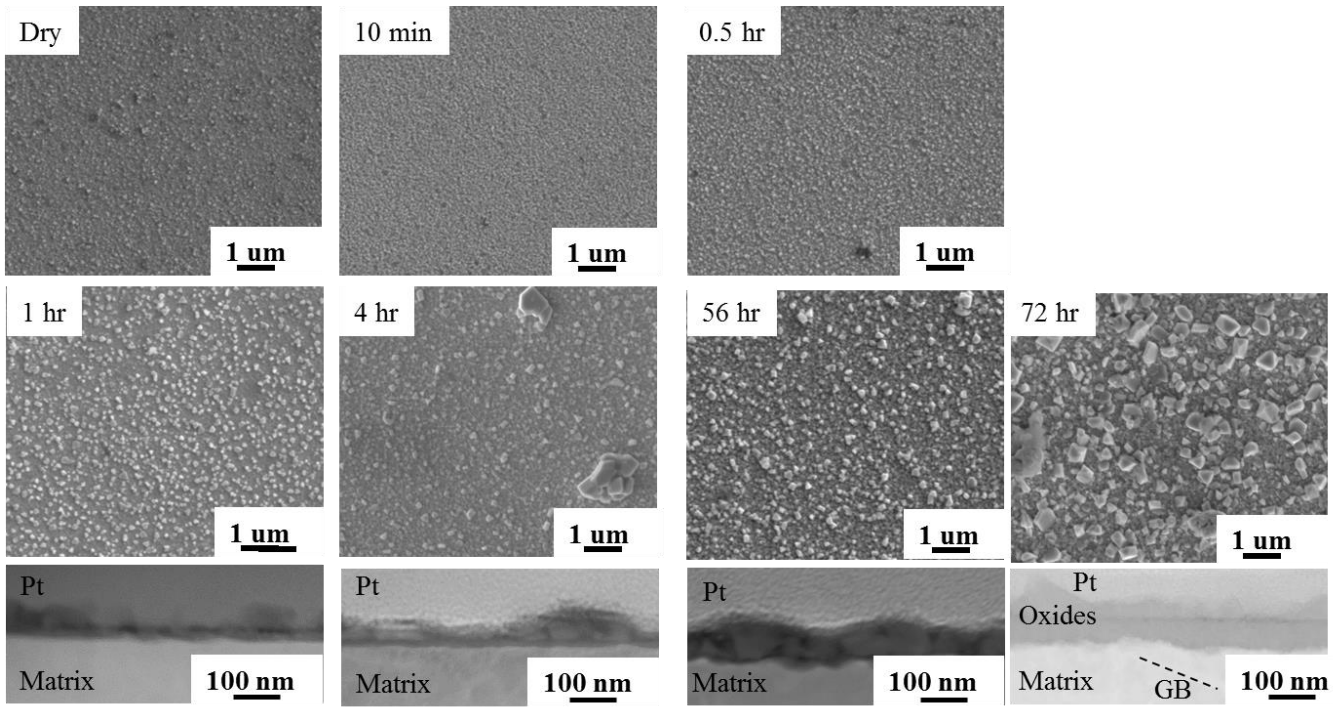

Figure 12: SEM surface images and STEM cross section images of electropolished surfaces after select oxidation times

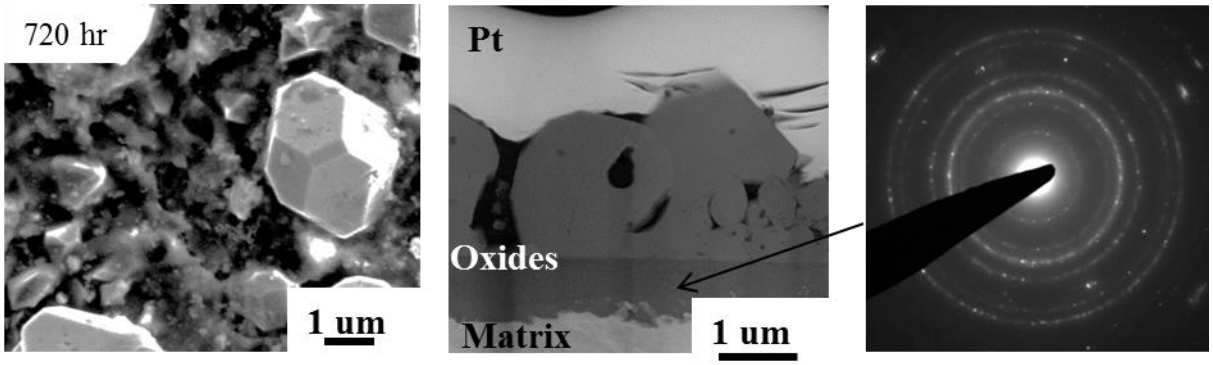

Figure 13: Characterization of oxide on a machined surface after 3 months. (a) SEM image of the surface, STEM image of a cross section, and diffraction pattern from the inner oxide.

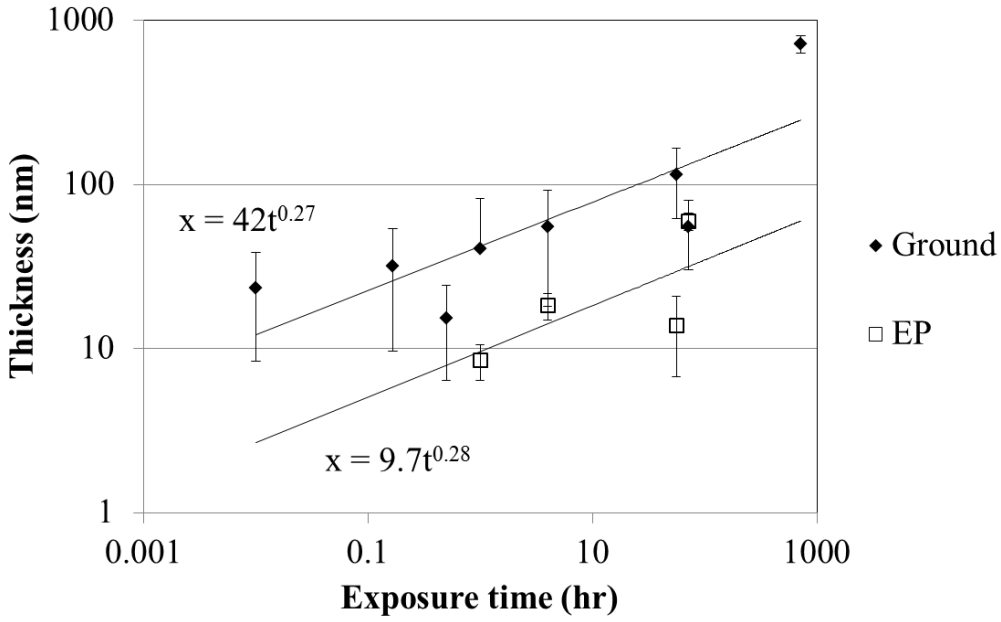

Figure 14: Oxide thicknesses measured from STEM cross sectional images

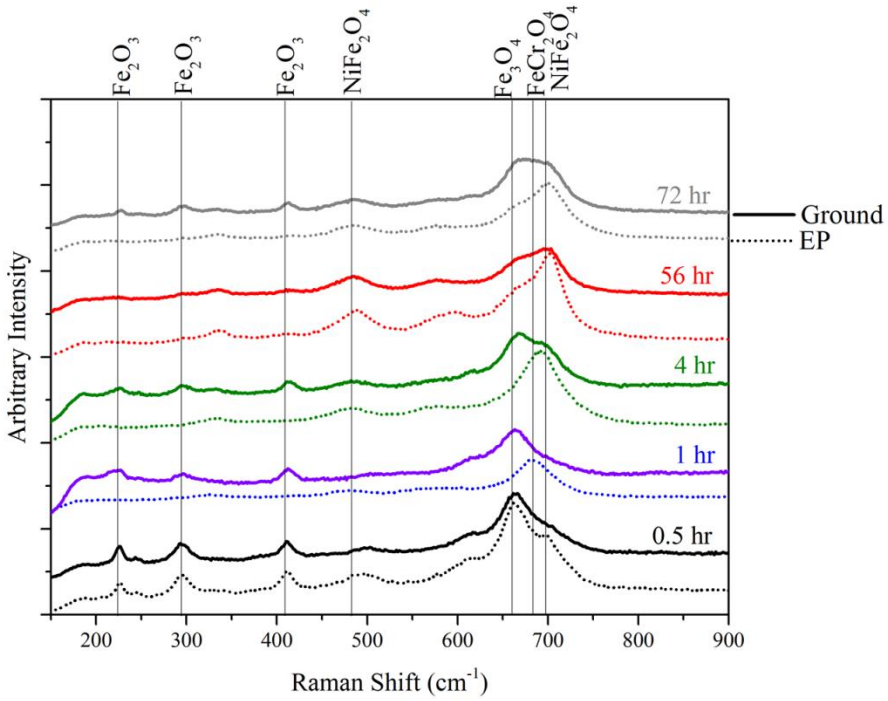

Figure 15: Raman spectra from ground (solid) and electropolished (dashed) lines after each exposure time

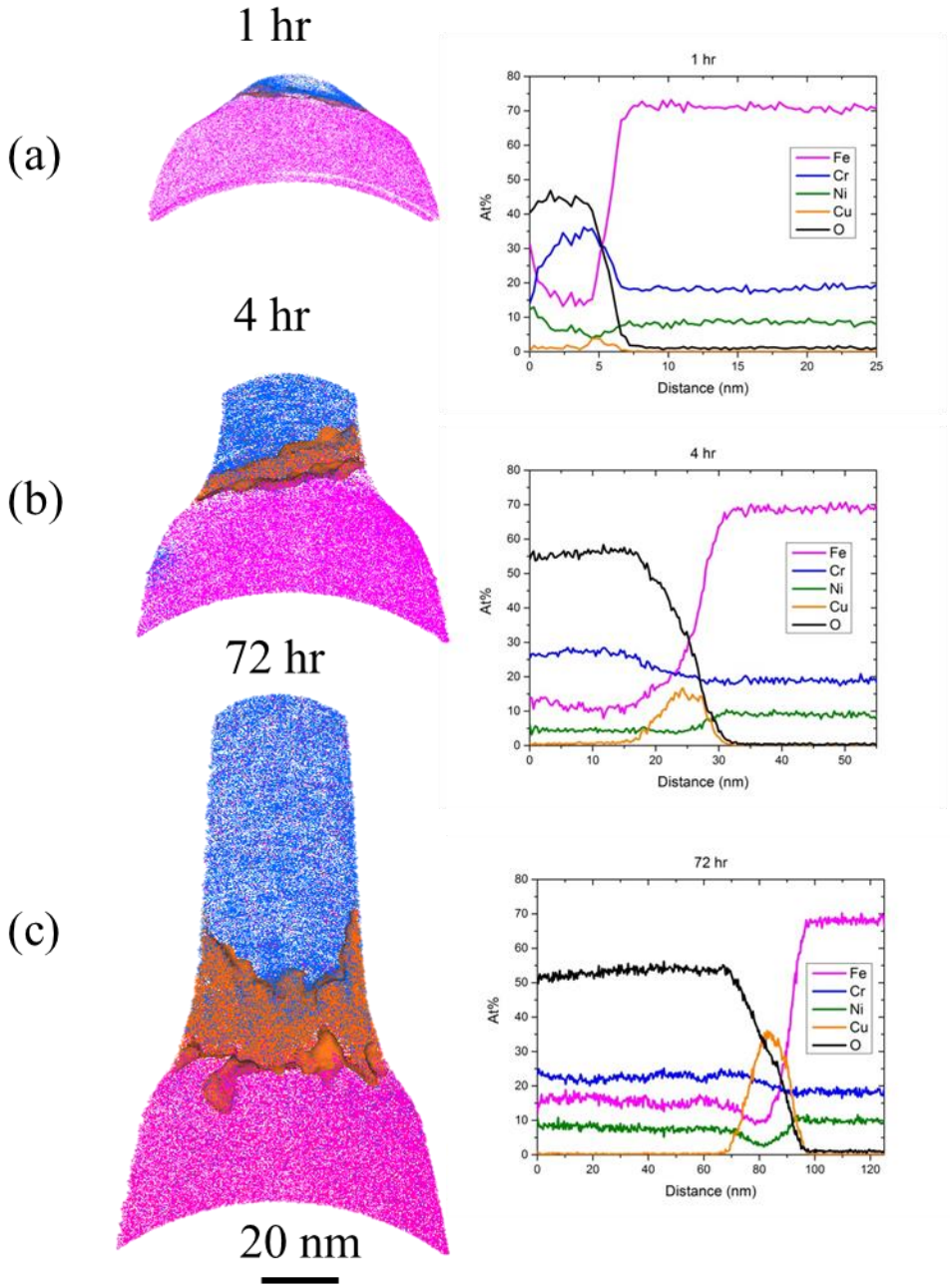

Figure 16: APT reconstructions of specimens obtained from electropolished surfaces after select exposure times. For each reconstruction a 10 nm slice from the center is shown with 10% of Fe atoms (pink), 100% of Cu (orange), and 100% of CrO (blue) ionic species, along with an 2% (a) or 8% (b and c) Cu isoconcentration surface (orange). Also shown are 1-dimensional concentration profiles of major species obtained from a 10nm diameter cylinder placed in the center of the reconstruction parallel to the specimen axis with a bid width of 0.3nm. (a) 1 hr exposure. (b) 4 hr exposure. (c) 72 hour exposure.

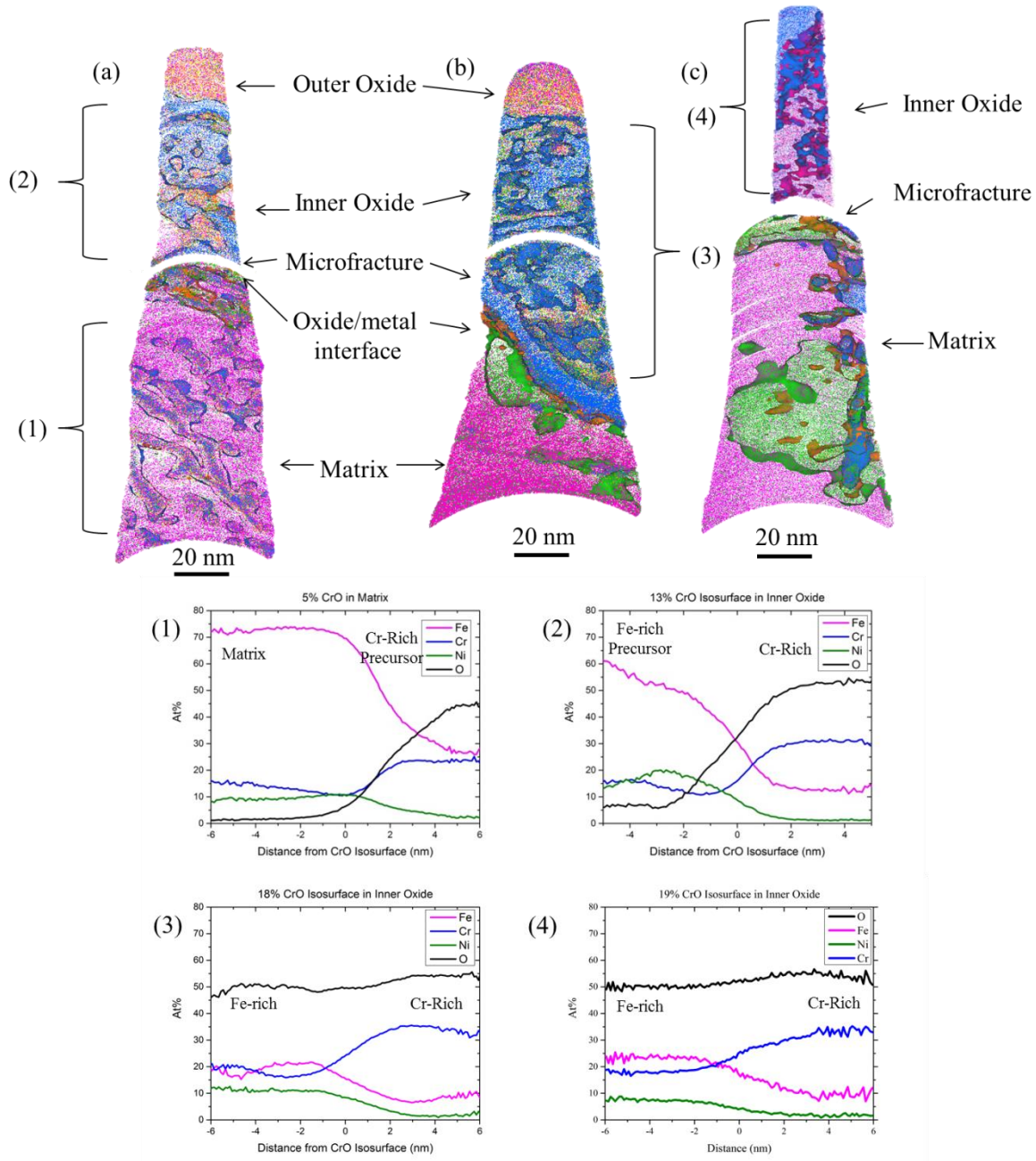

Figure 17: APT reconstructions of specimens obtained from ground surfaces after select exposure times. For each reconstruction a 4 nm slice from the center is shown with 30% of Fe atoms (pink), 100% of Cu (orange), 50% of Ni (green), 100% of FeO (yellow), and 100% of CrO (blue) ionic species, along with CrO isoconcentration surface as defined in the proxigram title (blue), a 2% Cu isoconcentration surface (orange), and a 22% Ni isoconcentration surface (green). Also shown are proxigram concentration profiles of major species obtained by measuring in either direction from the CrO isoconcentration surfaces within the relevant oxide layer. Each specimen exhibited a small microfracture, which is left as a gap of unknown width in the reconstruction. (a) 1 hr exposure. (b) 72 hour exposure. (c) 3 month exposure.

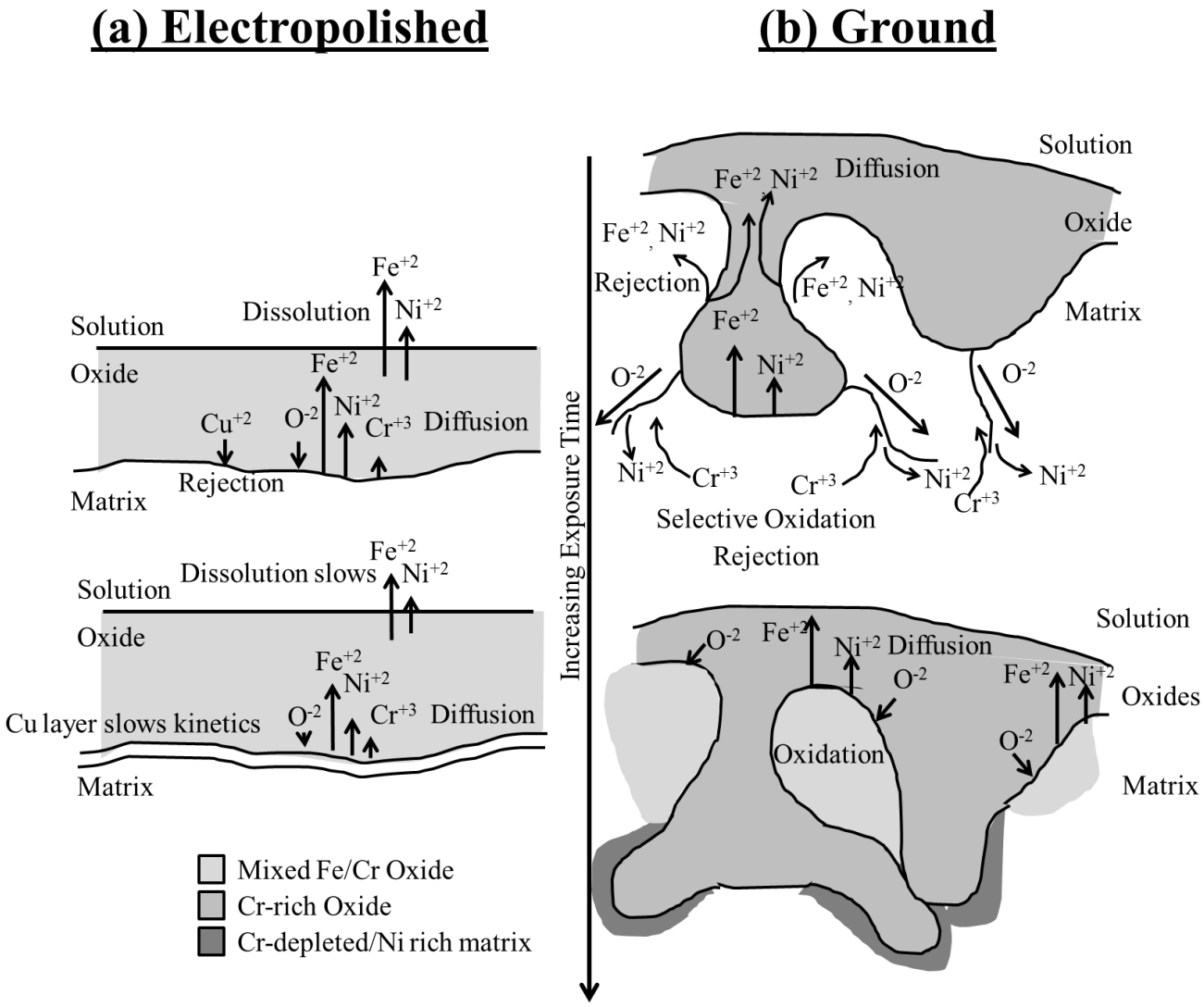

Figure 18: Schematic diagrams for the proposed oxidation mechanisms resulting in the observed inner oxide layers for (a) electropolished and (b) ground specimens. The length of straight arrows corresponds to the relative diffusion rate in the oxide, while curved arrows represent diffusion or rejection in the matrix. For each case, the two processes shown are actually occurring simultaneously, but the dominant process changes as time progresses.

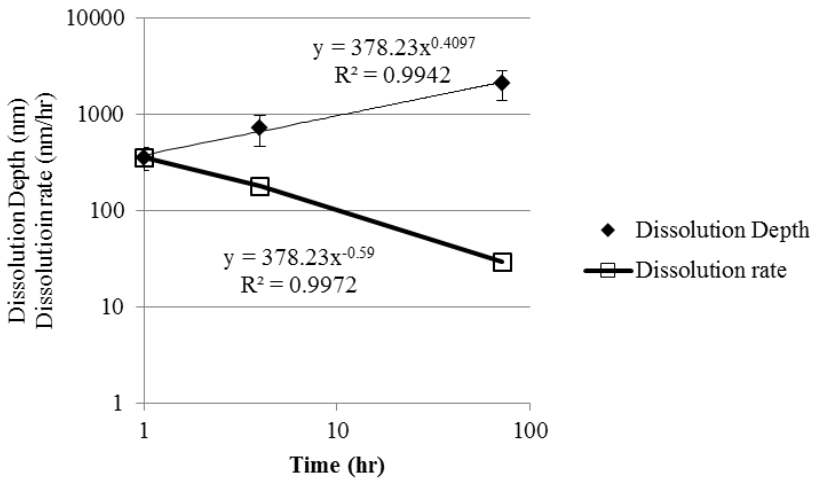

Figure 19: Necessary dissolution depth and calculated dissolution rate to achieve the amount of copper observed at the oxide metal interface, assuming full rejection of Cu from the oxide to the interface of electropolished specimens.

CHAPTER 5:

The Role of Microchemistry and Deformation in the Stress Corrosion Cracking Response of Dual Certified 304/304L SS in High Temperature Water[1]

5.1 Introduction

SCC is a serious materials degradation issue in nuclear reactor environments, with several noted cases throughout the world in the last several decades [40]. SCC can result from a combination of (1) a susceptible material, (2) an aggressive environment, and (3) a tensile load. One material that has been found to be prone to SCC is Type 304 SS, especially in oxidizing conditions such as those found in boiling water reactors or in occluded regions of pressurized water reactors where oxygen can accumulate. Enhanced propensity for SCC in such conditions has been linked to sensitization during welding that results in GB carbide precipitation and Cr depletion [60]. The Cr depleted GBs are susceptible to corrosion attack in oxidizing environments, promoting intergranular cracking. One strategy to mitigate SCC includes deoxygenating the water by the addition of hydrogen to reduce the potential for corrosion. Indeed, in hydrogenated water the opposite was found whereby SCC CGR is suppressed even in the presence of GB Cr depletion and carbide precipitation due to the formation of a network of carbides that impede GB sliding and crack growth [53, 54].

Deformation in the form of CW, which may be present due to machining during the fabrication of reactor components, has also been implicated in increased susceptibility to SCC in oxygenated and deoxygenated conditions [46, 77]. Suppression of deformation by careful fabrication procedures or post processing heat treatments may not be possible, and deformation

[1] The content of this chapter is adapted from the following articles which have been published or are currently under review:
Fisher, K. B., Miller, B. D., Johns, E. C., Hermer, R., Brown, C., Marquis, E. A., The effect of cold work on the crack response of dual certified type 304/304L stainless steel containing boron, Proceedings from the 17th International Conference on Environmental Degradation of Materials in Nuclear Power Systems – Water Reactors, Ottawa, Ont., CAN, 2015.
Fisher, K. B., Miller, B. D., Johns, E. C., Hermer, R., Brown, C., Marquis, E. A., The effect of cold work on the crack response of dual certified type 304/304L stainless steel containing boron, Proceedings from the 18th International Conference on Environmental Degradation of Materials in Nuclear Power Systems – Water Reactors, Portland, OR, USA, 2017. (under review)

levels as low as 5% CW have been noted to have an impact on the SCC response of some materials [39].

Another mitigation strategy for materials that may have exposure to oxygenated conditions is to remove the possibility of carbide precipitation and Cr depletion by suppressing the carbon content of the material, which is the basis for Type 304L SS. Dual certified Type 304/304L SS maintains the stricter strength requirements of Type 304 SS, while suppressing the carbon content below 0.03 wt%. However, other minor element additions may be present, or necessary, in order to fabricate this dual certified material. For instance, nitrogen may be added in place of carbon to enhance the strength of the material [58], while boron can be added to improve the hot-workability [59]. Such additions are not strictly controlled according to the material specifications.

Boron particularly has the potential to cause problems in terms of SCC susceptibility because it is insoluble in austenitic stainless steel and thus preferentially segregates to GBs. Furthermore, it can form Cr-rich borides during heat treatment [59]. Previous results identified the presence of Cr-rich M_2B borides in as-received mill annealed dual certified 304/304L SS that had elevated (18 ppm) boron content [57]. Further analysis suggested that the Cr depletion level was not significant enough for the material to be classified as sensitized [57], and indeed it passed the ASTM A262 Practice E sulfuric acid test indicating that it should be resistant to SCC [150]. However, double-loop potentiokinetic reactivation measurements of the degree of sensitization indicated that it may be susceptible to IGSCC [150].

The current work builds upon the evidence of the role of boron and other microchemical features in the IGSCC of dual certified Type 304/304L SS in oxygenated and deoxygenated conditions by performing SCC testing on mill annealed and deliberately sensitized material. Results from sensitized materials are compared to mill annealed materials under the same material deformation and SCC testing conditions.

5.2 Experimental

SCC tests were conducted on two heats of dual certified Type 304/304L SS with different boron contents and CW levels. Bulk measurement using glow discharge optical emission spectroscopy (OES) and inductively coupled plasma OES indicated that Heat D contained <6 ppm boron and Heat E contained 18 ppm boron. The chemical makeup of both materials, besides boron content, was essentially the same, as shown in Table 9. Heat D contained a small fraction

(~ 1.3%) of delta-ferrite stringers oriented parallel to the cracking direction [151]. Both heats were tested under two heat treatment conditions: mill-annealed (MA) and deliberately sensitized. The MA treatment was a solution annealed at 1079 °C for 3.5 hours and water quenched and the sensitization treatment was at 649 °C for 10 hours followed by air cool to room temperature. Heat treated bars were then loaded in uniaxial tension at 140 °C to introduce CW. Compact tension (C(T)) specimens were fabricated from MA bars with approximately 0, 5, and 10% CW and sensitized C(T) specimens were fabricated from only 0 and 10% CW material. Each specimen is identified by its heat (D or E), CW level (0, 5, or 10), and heat treatment (S for sensitized).

C(T) specimens were precracked in air at a final K_{max} of 19.8 MPa$\sqrt{m}$ to a crack length of 2.8 mm beyond the machined notch. SCC tests were conducted at 249 °C in three phases. The *in situ* electric potential drop (EPD) method was used to measure the crack extension during testing. Phase 1 occurred with a triangular load form with 500 s rise and fall time in aerated water (1 ppm O_2) with 150-250 ppb sulfate anion additions. Phase 2 had the same water chemistry as phase 1, but a trapezoidal load form with 500 s rise and fall time, and 9,000 s hold time. Phase 3 had the same trapezoidal load form as phase 2, but was in deaerated water with 30 cc H_2/kg H_2O and less than 20 ppb O_2.

After testing C(T) specimens were sectioned in half through the thickness using wire electric discharge machining (EDM). One half was fatigued apart for fractographic analysis and EPD crack extension correction measurements. The other half was polished to a mirror finish to remove the EDM surface and allow for cross sectional analysis of the crack path and crack tip. Characterization of the resulting cracks was performed using a variety of techniques in order to elucidate the driving factors for crack growth. Microstructural analysis of the materials was performed on an optical microscope after conducting ASTM A262 Practice A oxalic acid etch test (referred to as Practice A) [55]. A Helios 650 Nanolab or Nova 200 Nanolab dual beam scanning electron microscope (SEM)/focused ion beam (FIB) equipped with an Omniprobe micromaniplator was used for imaging and preparing APT and TEM specimens using the site specific liftout technique [135]. Electron backscatter diffraction (EBSD) was performed on a Philips XL30FEG using a TSL OIM detector and software. A Hitachi HD-2300A scanning TEM (STEM) system was used for phase contrast imaging and energy dispersive x-ray spectroscopy (EDS) and a JEOL 2010F TEM system equipped with a Gatan electron energy loss spectrometry

(EELS) system was used for additional imaging and chemical analysis of light elements. Finally, APT was performed on a Cameca 4000X HR local electrode atom probe in laser pulsing mode at a temperature of 50 K, a pulse rate of 160-200 kHz, a laser energy of 50 pJ, and a detection rate of 0.005-0.01 atoms per pulse to measure light elements, such as boron, in the GB and to characterize the oxide generated within the crack. Subsequent analysis was performed using Cameca IVAS 3.6.12 software. Reconstructions were fabricated using the voltage evolution method for matrix specimens and the shank angle method for specimens containing both oxides and matrix due to varying evaporation field.

5.3 Results

5.3.1 Microstructure

Deformation in the form of CW increases the dislocation density in the microstructure, causing increases in the material strength. To quantify the differences between the specimens tested the yield, ultimate, and flow stress of each material were measured by the Naval Nuclear Laboratory, and are reported in Table 10.

Practice A results for MA and sensitized specimens of both heats and 0 and 10% CW levels are shown in Figure 20. Consistent with previous results from the same material [57, 150], Heat E exhibits a dual structure (some GB etching) in the MA condition. It appears to exhibit increased GB etching at 10% CW than at 0% CW, although Practice A does not allow for such distinction in the classification system. Heat E exhibits similar levels of GB etching in the sensitized condition. On the other hand, heat D exhibits no GB etching (step structure) in the MA condition. However, in the sensitized condition, etching of discrete intragranular points is also observed. These were found to correlate to the delta ferrite phase by etching the perpendicular surface, as shown in the inset of specimen D10S in Figure 20. None of the etch structures identified in these materials would indicate suspicion of susceptibility to SCC, as no ditch structures surrounding entire grains were observed.

5.3.2 SCC crack growth

The measured SCC CGR for all specimens is shown as a function of the test phase in Figure 21, and tabulated along with measured crack extension and exposure time in each phase in Table 11. In general, the CGR decreases from phase 1 to phase 3, commensurate with the decrease in aggressiveness of the test environment and load form. Additionally, in the sensitized

specimens higher CW level is clearly linked to higher CGR in phases 1 and 2 compared to 0% CW. In MA specimens the CGR trend is less clear: One specimen, E10, exhibits CGR more similar to sensitized specimens with 10% CW, while the remaining specimens (E0, E5, D0, D5, and D10) all exhibit lower CGRs in phases 1 and 2. Interestingly, three of the four 0% CW specimens (E0, E0S and D0S) exhibit an apparent increase in CGR in phase 3 compared to phase 2.

Additional analysis of the SCC crack growth character (intergranular (IG) versus transgranular (TG)) was performed by examining the crack path in relation to the GB structure using EBSD, and the overall crack character by imaging the fracture surface. EBSD maps of a crack cross section of each specimen are shown in Figure 22. The mapped region shows all of phase 3, and most or all of phase 2 in most cases, although the exact test phase boundaries could not be determined. It should be noted that a single, random cross section of the crack from near the middle of the original C(T) specimen was analyzed, so it is unclear how representative of the entire cracking character it may be. It does, however, highlight the extent of crack branching and the degree of IG versus TG cracking character in a qualitative manner. From the EBSD maps it is seen that of the MA specimens, E10 favors IG cracking while the remaining specimens are largely TG in nature, with some IG portions or crack branches. Of the sensitized specimens, D10S and E10S, exhibit extensive crack growth that is largely IG in nature, while the 0% CW specimens show predominately TG nature.

These results are corroborated by backscatter SEM images of the fracture surfaces, sections of which are shown in Figure 23 for MA specimens and Figure 24 for sensitized specimens. The approximate test phase boundaries were overlaid according to the corrected EPD crack extension by measuring down from the phase 3 crack tip/fatigue apart line (clearly visible due to the lack of oxide after the crack tip) and up from the precrack/phase 1line (approximated from a change in the oxide structure). In two cases (D0 and D10S) the resulting phase 2 extension was significantly different than what was expected based on the corrected EPD measurement. A clear ‘rock candy’-like structure is observed on specimens E10 and E10S, indicative of IG cracking. Specimen D10S also exhibits some IG nature along with linear features parallel to the crack growth direction. E5 exhibits mixed character that is largely TG, but with some pockets of clearly visible IG cracking. The remaining specimens exhibit

predominantly TG cracking with some clamshell-like features typically associated with fatigue cracking mechanisms.

5.3.3 Grain boundary and interface chemistry

The GB chemistry was analyzed using APT in order to determine the role of boron and the sensitization heat treatment on the IG cracking behavior. GB chemistry is reported as interfacial excess (IE) which is a measure of extra (positive) or lost (negative) atoms of a specific species at the GB compared to the surrounding matrix, and is reported in units of atoms per area. Significant fluctuations were observed in many of the species within a single APT specimen, and from specimen to specimen within the same sample, so the reported values were averaged over multiple specimens from each material when possible. Random high angle GBs were examined from each of the 0% CW specimens as a baseline for GB chemistry, since no IG cracking was observed in these specimens. GBs ahead of IG crack branches in 10% CW specimens were then analyzed to determine if the GB chemistry was tied to the propensity for cracking. The overall GB chemistry results are summarized in the plots in Figure 25, and followed by specific examples of particular features in Figure 26a-d. Figure 26a shows an APT reconstruction of a GB from D0, along with a 1-dimensional concentration profile across the GB. As far as major elements, there was clear enrichment of Cr and depletion of Fe at the GB, while Ni was very slightly depleted. Minor element segregation of C, B, P, and Mo were consistently observed at the GB. No significant differences were observed at the GB of D0S after sensitization, nor in specimens D10 or D10S in GBs that crack branches were traveling along, compared to this baseline obtained from D0.

The measured GB chemistry trends for heat E, shown in Figure 25b are not as clear. Upon initial inspection each element behaves similarly – Fe is depleted while Cr is enriched at the GB. B, C, and P are also all enriched at the GB, while no Mo was measured in this material. However, significant variation within samples from a given specimen, and from specimen to specimen is obvious, and is attributed to the presence of some GB precipitates. An example of a GB precipitate captured in an APT specimen from E10 is shown in Figure 26b along with a 1-dimensional concentration profile across the precipitate. Evidence of these Cr-rich boride precipitates was consistently found in GBs along which cracks were growing in specimens E5, E10, and E10S. The measured chemistry of the boride was 44.3±1.0 at% Cr, 25.8±1.0 at% Fe, and 28.3±0.5 at% B. They are expected to be M_2B borides based on previous work on this heat

[57], and the known boron detection deficiency in APT due to its extremely high evaporation field and prevalence to evaporate in multihits [152]. An additional example of a specimen that captured the GB in the vicinity of a boride is shown in Figure 26c, clearly showing that the GB is depleted in Cr in contrast to the enrichment normally observed. It is difficult to know the exact proximity to boride precipitates of any APT specimens from this material, likely accounting for the larger variation in measured GB chemistry in Figure 25b. Finally, an example that captured both the GB and the boride precipitate from the GB ahead of a crack in E10S is shown in Figure 26d. In this example, while Cr is enriched in the GB compared to the surrounding matrix, the entire region is depleted in Cr compared to the nominal matrix chemistry.

As described, heat D exhibited a small amount of delta ferrite in the matrix that preferentially etched during Practice A, while the GBs did not. For this reason, the austenite/ferrite interface was also examined for unique chemical signatures. SEM images of the ferrite/austenite boundary for D10 and D10S are compared in Figure 27. These images clearly exhibit the presence of extensive precipitates at the interface and growing into the ferrite phase after sensitization heat treatment. Further characterization of the sensitized interface was performed using TEM as shown in Figure 28a-c. The precipitate is clearly identified as a Cr-rich carbide, likely of $M_{23}C_6$ form, and exhibits Cr depletion primarily in the ferrite phase adjacent to the precipitate.

5.3.4 Oxide chemistry and morphology

The oxide was examined in regions exposed to aerated and deaerated water using a combination of TEM and APT for a subset of the samples in order to gain insight into the role oxidation played in the cracking process. APT specimens were fabricated from a variety of regions in specimens E5, E10, and D10, encompassing primarily oxygenated water environments, and both IG and TG cracks, by performing site specific liftouts from the polished crack cross section. It is difficult to determine the exact exposure time of the specimens due to the high degree of crack branching, and the uncertainty in the representativeness of the farthest extended “crack tip” in the polished cross section with regards to the entire crack front.

The average oxide chemistry for each region is reported in Table 12. The oxide was composed of two distinct oxide types similar to those observed on surface specimens discussed in Chapter 4: An inner oxide layer adjacent to the metal that is compact and has mixed Fe and Cr content and low Ni content, and an outer oxide layer of discrete particles that is rich in Fe and

low in Cr with varying Ni levels. No significant difference was observed in the oxide chemistry between IG or TG cracks, Phase 1 or Phase 2 of testing, or heat E versus heat D. The only exception is the inner oxide chemistry of specimen E10 appears to be richer in Fe than the same oxide layer in the other specimens. While some variation is observed in the measured oxide chemistry from APT specimen to specimen, the oxide composition within each APT specimen were relatively uniform in composition and exhibited a clean oxide/metal interface without matrix penetration of oxygen. This can be seen in the representative atom probe reconstructions displayed in Figure 29 from specimens E5 and E10. These specimens, which also capture the oxide/metal interface, reveal low levels of Ni and Cu enrichment is observed, albeit discontinuously, at the oxide/metal interface.

Plan-view TEM specimens were fabricated from the farthest extended crack tip of the polished cross section, and are shown in Figure 30. Again, it is difficult to know how these crack tips compare to the final overall crack front, but based on additional analysis discussed in the next paragraph, it is assumed that each of these crack tips represents a crack that stalled during phase 2 oxygenated water testing, with the exception of specimen E0. The crack tips analyzed from heat D in the unsensitized condition were all transgranular, while in heat E, E0 was transgranular and E10 was intergranular. The crack tips analyzed from D10S and E10S after sensitization were intergranular. This is consistent with characterization of the main crack path using EBSD maps and fracture surface evaluation. In all cases the crack tip was filled with a mixed Fe/Cr spinel of varying Fe/Cr content. In the middle portion of the crack Fe-rich oxide particles were often observed.

Finally, TEM specimens capturing the crack tip from the final portion of testing, phase 3 deaerated water, were fabricated from the fracture surface by choosing a representative area of the crack front, as shown in Figure 31. For each specimen, SEM images of the fracture surface area chosen for analysis are shown along with the resulting TEM specimen and a close up of the oxide. In these specimens, only 1 half of the crack tip is captured because the crack was broken open to examine the fracture surface. The red arrow points to the transition from the oxidized crack tip to the fatigue apart. The approximate exposure time at the back end of the specimen, based on the phase 3 CGR, is also shown. It is clear that very little oxide is present in the crack in most of these specimens, due to the deaeration of the water, allowing us to conclude that previous plan-view crack tip TEM specimens were all gathered from the oxygenated test phase.

The specimen from D10 has a very thick oxide film, and this is attributed to essentially no crack growth in phase 3 (4 um of crack growth was measured, but may not have been observed over the entire crack front). Thus, this is actually a representation of the crack tip after phase 2 testing. The specimen from E10S also exhibits a thicker oxide film than the other specimens, and it is unclear if this is due to the region being obtained from an oxygenated phase, or due to microchemical or microstructural considerations, as is discussed later. E10 and E10S also both exhibit regions of enhanced oxide growth on the IG grain face (readily visible in the SEM image of specimen E10). One of these regions from E10 was analyzed further using APT, and a reconstruction is shown in Figure 29c. The oxide in this region is Fe-rich and surrounds a boride precipitate that appears to have partially dissolved based on its small size compared to GB precipitates discussed earlier.

In specimen D10S, a TEM specimen was prepared across a delta ferrite near the crack front, instead of perpendicular to the crack front as with the other specimens. This specimen is shown in Figure 28d along with an EDS map of the region (Figure 28e). It is again unclear if this cracking occurred during phase 2 aerated water, or phase 3 deaerated water. In this example heavy oxidation of the delta ferrite phase was observed, and the resulting oxide was rich in Fe and deficient in Cr as a result of the Cr depletion that occurred during sensitization. Further characterization of this oxide, in terms of the oxide structure, was not performed. Embedded in the oxide were Cr-rich precipitates that appeared much smaller than those observed at the delta ferrite/austenite boundary from the bulk, suggesting they have partially dissolved.

5.4 Discussion

5.4.1 The role of deformation

It is well understood that CW has a detrimental effect on the SCC propensity of 300 series stainless steels in oxygenated and deoxygenated conditions, even at levels as low as 5% [39, 46, 77]. This effect has been attributed to increased strength and decreased cyclic plastic zone (CPZ) size at the crack tip resulting from a higher dislocation density [77]. Plastic zone size can be calculated using the equation for the plain strain condition:

$$r = \frac{1}{24\pi}\left(\frac{\Delta K}{\sigma_f}\right)^2 \tag{14}$$

where σ_f is the flow stress. Calculation of the CPZ size (Table 10) does suggest that cold worked specimens do indeed have decreased CPZ size. However, the crack growth results were not consistent with a mechanism governed only by CW, as the different heats exhibited differences in CGR even under similar CW conditions.

10% CW had a pronounced effect on the SCC CGR and character of the crack, but only in the presence of sensitization and oxygen containing water (Figure 21). In the MA condition, E10 exhibited CGR in phase 1 and 2 aerated water enhanced by a factor of ~2 compared to the other specimens, and also exhibited evidence of some level of sensitization during Practice A. The enhanced CGR was accompanied by increased IG cracking, whereas the other specimens exhibited primarily TG cracking (Figure 22). In the deliberately sensitized specimens, both E10S and D10S exhibited much higher CGR than their 0% CW counterparts in oxygenated water (Figure 21), and it was again characterized as primarily IG cracking in E10S, and mixed IG and TG in D10S (Figure 22). On the other hand, D10, which had similar flow stress and calculated plastic zone size to E10, did not exhibit increased CGR, or IG crack growth.

Plan-view crack tip specimens gathered from the end of phase 2 testing in aerated water (Figure 30), and fracture surface crack tip specimens gathered from the end of phase 3 of testing in deaerated water (Figure 31) failed to clarify the role of deformation in the cracking process. Specimen E10S exhibited thicker corrosion product than the other specimens (neglecting D10, as discussed) in only slightly longer exposure time, but specimen E10, which had comparable deformation and exposure time, did not. This is possibly related to a microchemical effect, as discussed in the next section. Therefore, no correlation of oxide thickness or morphology with CW level could easily be identified, due to the unknown exposure times. However, APT specimens gathered from regions of the crack and fracture surface (such as those shown in Figure 29) do provide some clues as to the role of deformation when compared to surface oxidized specimens discussed in Chapter 4. The oxide film was mostly locally uniform in composition, and thus more similar in nature to the electropolished surface specimens. Some fluctuation in the oxide chemistry was observed in the 10% CW specimen (Figure 29b), but not to the extent observed previously, in that the Fe and Cr level never crossed. Small Ni and Cu pockets were occasionally observed at the oxide metal interface, as shown in the reconstruction in Figure 29a. While Cu reaches similar levels of a few atom percent, Ni, in general, is enriched

to a lesser extent than was observed in the deformed surfaces. These observations suggest that the local deformation in the material, either from the deliberate CW, or imparted by the crack advance, is not as pronounced as that observed on ground surface specimens analyzed in Chapter 4, resulting in a more uniform oxide composition.

While higher levels of CW do increase the SCC CGR due to changes in the CPZ size, such an explanation is unsatisfactory too fully explain the current results. Instead, the relatively low levels of CW in the current results are insufficient to promote enhanced SCC CGR without additional chemical factors such as sensitization, as discussed in more detail below.

5.4.2 The role of microchemistry

While the role of carbon in Type 304 SS under a variety of heat treatment conditions and water environments has been well established [53, 54, 60], the role of other minor elements is less well understood. In the current work boron, and carbon, in Type 304L SS are seen to play a role in SCC propensity.

After the MA heat treatment, increased boron and carbon levels were observed in similar levels at GBs compared to the matrix levels in both Heat D and Heat E, due to their insolubility in the steel matrix. However, considering only heat E exhibited GB etching during Practice A (Figure 20), and IG cracking in oxygenated water, microchemical factors were suspected. Furthermore, after sensitization both D10S and E10S exhibited enhanced CGR in oxygenated water (Figure 21), despite the fact that these low carbon materials were supposed to be resistant to sensitization heat treatments. This further implicated a potential role of other microchemical factors.

Indeed, Cr-rich boride precipitates were observed in cracked GBs in heat E after both heat treatments (Figure 26b and d). In the MA sample, Cr depletion was measured in the matrix adjacent to the precipitate, and in the GB close to boride precipitates (Figure 26c). Previous work has suggested that the term ‘sensitization’ applies to materials that exhibit GB Cr depletion to levels below 12 wt% [50], and that above this limit susceptibility to SCC should not be enhanced. While EDS measurements from this material had indicated that the Cr level in the GB remained above this 12 wt% limit [57], APT results shown in Figure 26 suggest that it can reach levels as low as 11.6 at% (10.9 wt%) in the GB and within a few nm adjacent to the precipitate. In the sensitized state the Cr depletion profile is more pronounced with depletion levels around

11.0 at% (10.3 wt%) or less extending for approximately 30 nm on either side of the precipitate and adjacent GB.

On the other hand, D10S exhibited similarly high CGR in aerated water test phases, but failed to exhibit any Cr depletion or precipitation along any GBs that were examined, whether randomly chosen or at GBs along which crack branches propagated. Evidence from the fracture surface, however, suggested that enhanced oxidation and crack propagation was associated with linear delta ferrites in the material (Figure 24), consistent with Practice A that showed enhanced etching of delta ferrites (Figure 20). Indeed, previous results for SCC in other austenitic steels with delta ferrite have shown improved resistance at low (< 7%) delta ferrite content and when the delta ferrite phase is present in isolated spheres, but when it forms a continuous network, SCC resistance is reduced due to cracking along the delta ferrite/austenite boundary [74]. In between the delta ferrites cracking occurred both in IG and TG forms (Figure 24), consistent with the EBSD maps that showed both types of cracking. Upon further inspection of delta ferrites in the bulk material, the delta ferrite/austenite boundary was decorated with Cr carbide precipitates after sensitizing heat treatment (Figure 27 and Figure 28). The delta ferrite phase is expected to form carbide precipitates more readily than high angle GBs according to the time-temperature-precipitation diagram [60, 68, 71]. Furthermore, as presented in Figure 28, Cr depletion of the ferrite phase preferentially occurs compared to the austenite matrix, which is consistent with the higher diffusion rate of Cr in ferrite than austenite [71].

Further examination of the resulting oxide was performed in order to understand the potential role of Cr depletion in the cracking process. Examination of a delta ferrite near the crack tip of the fracture surface indicates extensive oxidation of the ferrite phase around Cr-rich precipitates (Figure 28), consistent with enhanced oxidation resulting from Cr depletion, although, with the present observations, it cannot be determined with certainty whether oxidation occurred during phase 2 (aerated) or phase 3 (deaerated) testing. Furthermore, the measured oxide chemistry is Fe-rich and Cr depleted as a direct consequence of the metal chemistry before oxidation. Similar results were found for specimen E10 by examining one of the pockets of enhanced oxidation observed on the grain face (see Figure 30) using APT. These pockets apparently formed at regions where boride precipitation occurred, as evidenced by the APT specimen shown in Figure 29c. The Cr depleted region was subject to enhanced oxidation resulting in a Cr deficient oxide in the regions surrounding the boride precipitates. Farther away

from the precipitates the oxide chemistry returns to higher Cr content. This also provides a potential explanation for the enhanced oxidation observed in specimen E10S (Figure 30), although measurement of the overall oxide chemistry in several regions using EDS did not reveal Fe-rich, Cr deficient oxides like that observed adjacent to the boride in E10. The oxide was much thicker, however, and the resolution of EDS line scans and maps (not shown) may not have been sufficient to identify Fe-rich oxides of the thickness of the Cr depleted regions (~30 nm). The oxide in this region may also have been enhanced by the deformation level, or it is possible the specimen was prepared from a region that did not crack in Phase 3. A combination of deformation, local chemistry, and/or water chemistry effects is also likely.

Overall, these observations suggest that despite the low carbon levels present in the bulk material for both heats, allowing for L-grade classification, both heats were susceptible to sensitization in another fashion due to their unique microchemical properties. In heat D the fast diffusion rate of Cr in the delta ferrite phase, coupled with heat treatment times long enough for carbon diffusion from the austenite or grain boundaries, resulted in Cr carbide precipitation at the austenite/delta ferrite interface, and subsequent Cr depletion of the delta ferrite phase [70]. On the other hand, in heat E, the high boron content was sufficient for Cr-rich boride precipitation and subsequent Cr depletion of the GB and surrounding matrix, despite the lower diffusion rate of Cr in austenite. In both cases the result was a region of Cr depletion susceptible to enhanced dissolution and oxidation response, and resulting in a thicker, Cr deficient oxide film. Such thick, non-protective, oxide films have been implicated in cracking by a slip-dissolution mechanism by providing a brittle path for the crack to propagate along [43]. Indeed, many of the crack tip specimens (specifically, D5, D10, D10S and E10S) shown in Figure 30 clearly suggest that the crack tip itself is behind the oxide/metal interface in the oxide film.

Interestingly, sensitization appears to have a beneficial effect in non-cold worked material in an aerated environment based on CGR measurements in the current results (Figure 21). 0% CW specimens that exhibited some level of sensitization according to Practice A (E0, E0S, and D0S) all had suppressed CGR in aerated water compared to unsensitized 0% CW specimens (D0) and specimens with a higher degree of CW (D5, D10, and E5). This result is interesting as the cracking mode was primarily TG in all of these specimens (based on fracture surface examination), so GB (or interfacial) sensitization is not expected to have an effect on crack growth. It also seems to contradict conventional wisdom that in oxygenated water SCC

susceptibility increases with degree of sensitization, regardless of CW level. This effect disappears upon switching to deaerated water, where the CGR of non-cold worked, sensitized specimens actually increases compared to aerated water tests. To explore these relationships, the crack tip oxide structure was compared based on the crack tips generated from the fracture surfaces, from phase 3 deaerated water (Figure 31). For example, in comparing D0 (decreased CGR from phase 2 to phase 3) to E0, E0S, and D0S (increased CGR from phase 2 to 3), the crack nature (TG) and crack tip oxide (very thin) in all cases was similar, making the potential role of sensitization unclear. Similarly, in comparing E0 (increased CGR from phase 2 to 3) to E10 (decreased CGR from phase 2 to 3), the only difference appears to be that E0 exhibits TG cracking while E10 exhibits IG cracking, while both exhibit very thin oxide films, even in the presence of known GB sensitization in E10. Thus, the observed apparent effect of sensitization on CGR in undeformed specimens warrants further investigation to determine if it is real, an artifact of scatter in the CGR measurements, or a result of the testing order (aerated and then deaerated water).

5.4.3 The role of environment

It is well established that sensitized materials are susceptible to IGSCC in oxidizing conditions [60], while in deaerated water SCC can be suppressed by a network of carbides along grain boundaries [53].

In these tests the role of environment on the oxidation response was clear. Thick oxides films were generated in aerated water regardless of the presence of sensitization or nature of the crack. However, in sensitized specimens growing along the Cr depleted pathways, the resulting oxide was Cr deficient and thicker resulting in an easier pathway for crack propagation. This was apparent in the Cr depleted delta ferrite phase (Figure 28) although the test phase of this region is unknown. It was also apparent in deaerated water in E10, where pockets of thicker oxide were directly correlated to Cr-rich borides and Cr depleted regions (Figure 29c).

However, in all of the 10% CW sensitized specimens that exhibited enhanced CGR in aerated water the CGR was significantly suppressed upon testing in deaerated water, consistent with Ref. [53], even though fracture surface investigations indicated that the crack path continued to be IG. It is unknown if IG cracking would have occurred if it had not already existed from phase 2. The CGR of other cold worked specimens exhibiting primarily TG cracking (D5, D10, E5) also decreased upon transitioning from phase 2 to phase 3, regardless of

the prevalence of sensitization. Additionally, specimen D0, which did not exhibit sensitization or CW also exhibited the same type of decrease in CGR upon changing the test environment. This suggests that the less aggressive environment, in general, decreases the CGR irrespective of the CW or microchemical factors.

Environment appears to play an additional, albeit small, role in the CGR of non-cold worked, sensitized samples. Enhanced CGR in 0% CW specimens during phase 3 (compared to phase 2 CGR) occurred in the same three materials that exhibited microchemical evidence of sensitization (MA heat E, sensitized heats E and D), despite the cracking being entirely TG in nature. This occurred even though no evidence of different oxide structure was observed, as discussed previously. However, it should be noted that the CGR in both aerated and deaerated water was quite low, so despite a slight increase from phase 2 to phase 3, there still exists a similar resistance to cracking in either environment.

5.4.4 Implications for the use of 304L stainless steel in reactor environments

Type 304L SS is expected to be resistant to SCC in high temperature water by resisting sensitization associated with high carbon levels. The current work, however, suggests that while Type 304L SS can be resistant to SCC, additional factors must be considered.

Sensitization of these L-grade materials was observed in the form of Cr-rich borides in the elevated boron content material (heat E), and in the form of coarse carbides on the delta-ferrite/austenite interface in heat D, after deliberate sensitization. Heat E was also sensitized in the mill annealed condition, likely due to an inadequate quench rate during material fabrication. Thus, for practical applications of Type 304L SS in reactor components the chemical makeup, heat treatment, cold work/deformation, and environmental conditions must be considered. Elevated boron levels, or delta ferrite containing heats should be avoided in situations where: (1) the component is deformed (either surface or bulk deformation), (2) sensitization heat treatment may occur (ie. near welds), or (3) an oxidizing environment may exist. However, if any of these three components (deformation, sensitization, or oxidizing water) is not present, the prevalence of SCC will be reduced. The most reliable reduction in SCC CGR is obtained by ensuring the water is deoxygenated. However, in cases where deoxygenation is not possible, ensuring a low degree of deformation is the next best option, and slight sensitization might provide additional benefits, although this should be tested further.

5.5 Conclusions

1. Type 304L SS is not immune to sensitization in cases where it contains elevated boron content or delta ferrite stringers. Elevated boron content was shown to cause GB boride precipitation and Cr depletion during sensitizing heat treatments. In heats containing delta ferrite chromium carbide precipitation occurred preferentially at the delta ferrite/austenite interface and was accompanied by preferential Cr depletion in the delta ferrite phase.
2. In materials with 10% CW, sensitization promoted IGSCC and enhanced CGRs in aerated water. This is likely due to enhanced dissolution and oxidation of the Cr depletion region. Material deformation likely also played a role in enhancing the oxidation rate, although direct evidence of this, beyond the increase of SCC CGR in 10% CW materials, was not conclusively achieved. In materials with 0 and 5% CW, even when sensitized, cracking was primarily TG in oxygenated and deaerated environments, indicating relative resistance to SCC.
3. In materials with 0% CW sensitization may have an additional beneficial effect on SCC CGR in aerated water, although this should be tested further. This beneficial effect does not carry over to deaerated water, where the CGR actually increased slightly compared to aerated water when sensitization was present. The apparent beneficial effect of sensitization in aerated water in the absence of CW warrants further investigation, as it could not be obviously linked to a change in the oxidation response.
4. Careful consideration of the material features (bulk boron content, the presence and morphology of delta ferrite, and CW levels, and the likelihood for sensitization) and environment (oxygenated versus deoxygenated) should be employed when considering the use of Type 304L SS in reactor components.
5. Additional testing to decouple the role of crack mode (IG vs. TG) with water chemistry would be beneficial to ensure that sensitization in the presence of CW in a deaerated water environment results in IGSCC.

Table 9: Composition in wt% as measured by optical emission spectroscopy

Heat	B	S	P	Co	C	Cu	N	Mo	Mn	Si	Ni	Cr	Fe
D	<0.001	0.001	0.023	0.05	0.019	0.17	0.06	0.35	1.72	0.35	9.55	18.37	Bal.
E	0.0011	0.001	0.016	0.03	0.024	0.29	0.09	0.02	1.49	0.49	9.5	18.41	Bal

Table 10: Measured material properties and calculated cyclic plastic zone (CPZ) size

Heat	T (°C)	Specimen	Ultimate (ksi)	Yield (ksi)	Flow (ksI	CPZ (um)
D	249	0	59.0	24.3	41.6	10.9
		5	63.3	41.0	52.1	7.0
		10	65.9	51.9	58.9	5.5
		0S	60.1	26.1	43.1	20.0
		10S*	75.3	40.8	58.0	11.0
E		0*	70.5	30.4	50.4	7.5
		5	66.7	39.0	52.9	6.8
		10	70.8	57.4	64.1	4.6
		0S	71.1	29.5	50.3	14.7
		10S	79.6	61.8	70.7	7.4

* interpolated from additional data

Table 11: Test details including exposure time, measured crack growth rate, and EPD corrected crack extension for each specimen in each test phase

	Phase 1			Phase 2			Phase 3		
Specimen	Exposure time (hr)	CGR (um/hr)	Crack Extension (um)	Exposure time (hr)	CGR (um/hr)	Crack Extension (um)	Exposure time (hr)	CGR (um/hr)	Crack Extension (um)
D0	334	1.27	424	832	0.31	255	2351	0.03	59
D5	266	1.09	290	1062	0.21/0.11*	155	2056	0.005	11
D10	266	0.86	228	1062	0.17/0.03*	79	2056	0.002	4
E0	334	0.14	46	832	0.007	6.2	2351	0.11	259
E5	153	0.87	132	258	0.21	54	1172	0.02	26
E10	153	2.14	105	258	0.77	65	1172	0.14	551
D0S	750	0.11	17.8	428	0.03	30.5	1518	0.15	188
D10S	750	3.30	884	428	0.89	419	1518	0.06	132
E0S	750	0.08	22.9	428	0.03	15.2	1518	0.18	224
E10S	750	2.06	777	428	0.79	371	1518	0.05	109

Table 12: APT measured oxide chemistry from a variety of specimens and crack types

Specimen	Test phase	Description	O	Fe	Cr	Ni	Mn	Trace (Cu, Co, C, N, Al)	Unidentified
E5	1	IG Crack, Mixed Fe/Cr oxide	52.0±0.5	23.7±0.9	20.0±0.5	4.0±0.3	0.2±0.04	0.2±0.02	0.5±0.03
	1	TG Crack, Mixed Fe/Cr oxide	53.1±0.7	21.3±1.2	20.1±0.2	5.0±0.3	0.2±0.004	0.2±0.03	0.6±0.08
	2	IG Crack, Mixed Fe/Cr oxide	53.4	21.0	21.4	3.6	0.4	0.2	0.6
	2	IG Crack, Fe rich oxide	44.8	50.8	1.5	2.6	0.04	0.1	0.03
E10	2	IG Crack, Mixed Fe/Cr oxide	49.5±0.6	27.3±0.8	14.2±0.8	8.4±0.6	0.2±0.1	0.3±0.1	0.2±0.1
	2	IG Crack, Fe rich oxide	47.4±0.1	36.8±2.5	4.3±4.8	11.1±2.4	0.1±0.1	0.2±0.2	0.1±0.1
D10	2	IG Crack, Mixed Fe/Cr oxide	46.6	24.6	23.0	4.9	0.4	0.5	0.1

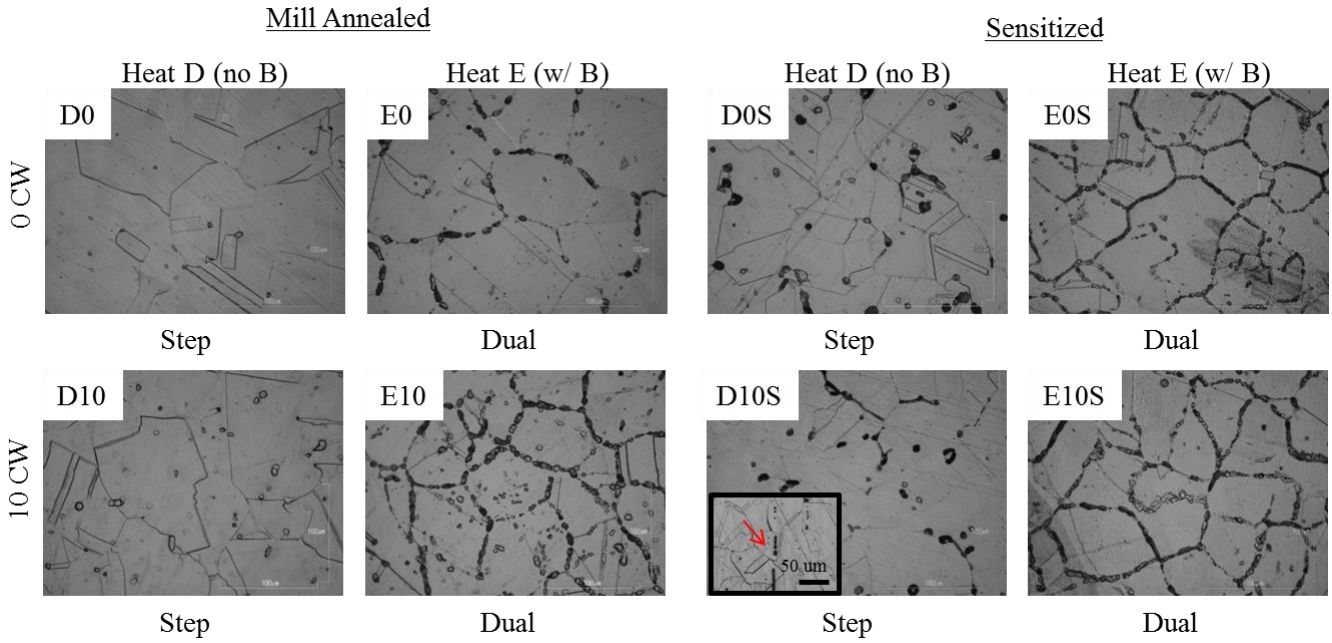

Figure 20: ASTM A262 Practice A etch test for each specimen in the 0 and 10% CW conditions (5% CW not shown). Heat E exhibited dual etch structure in both mill annealed and sensitized conditions, while heat D exhibited step structure for both heat treatments. Heat D exhibited etching at delta ferrites, as shown in the inset of D10S.

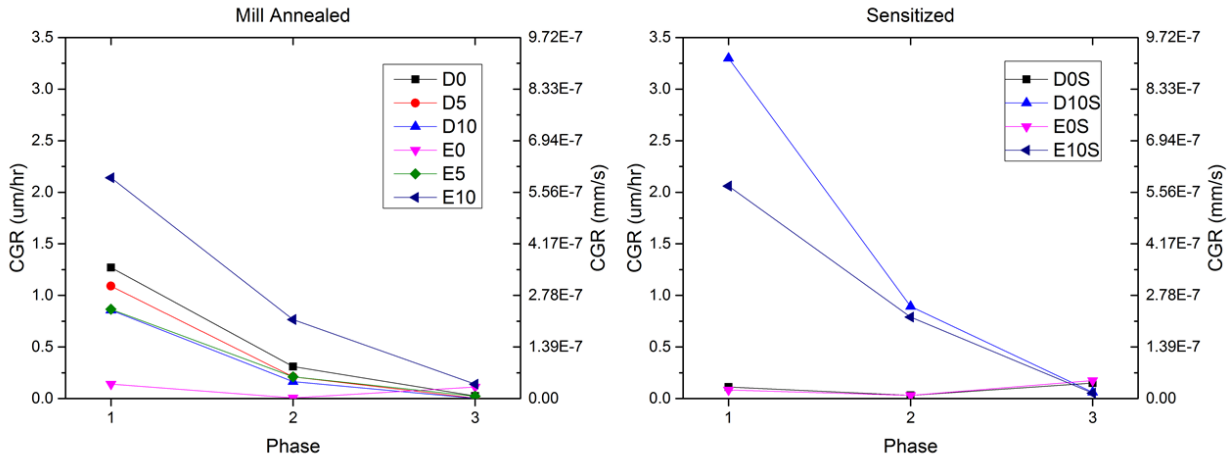

Figure 21: Electric potential drop measured crack growth rates as a function of test phase

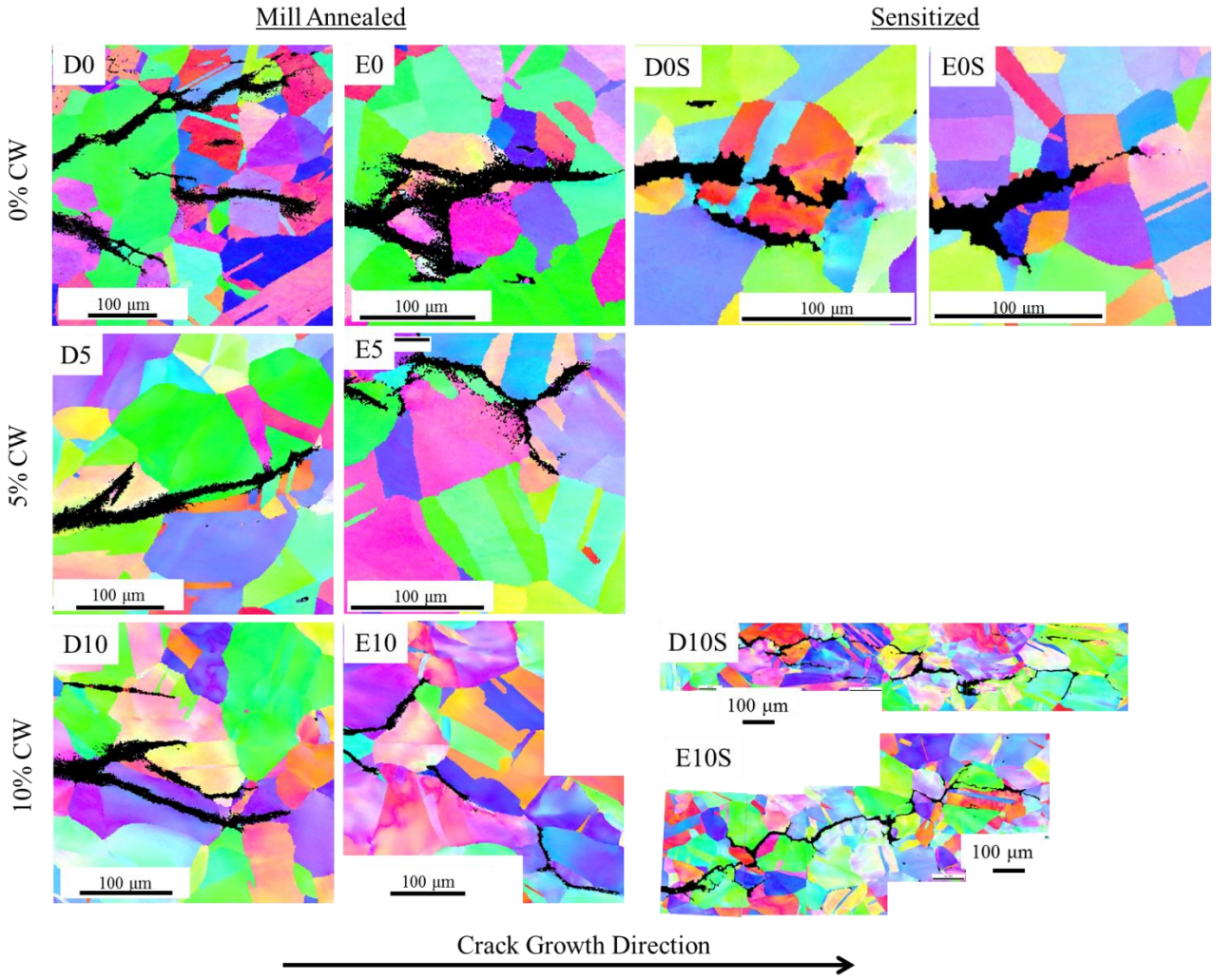

Figure 22: EBSD grain orientation maps. Black areas indicate the crack path. IG cracking was primarily observed in E10, E10S and D10S, while the other specimens exhibited primarily TG cracking.

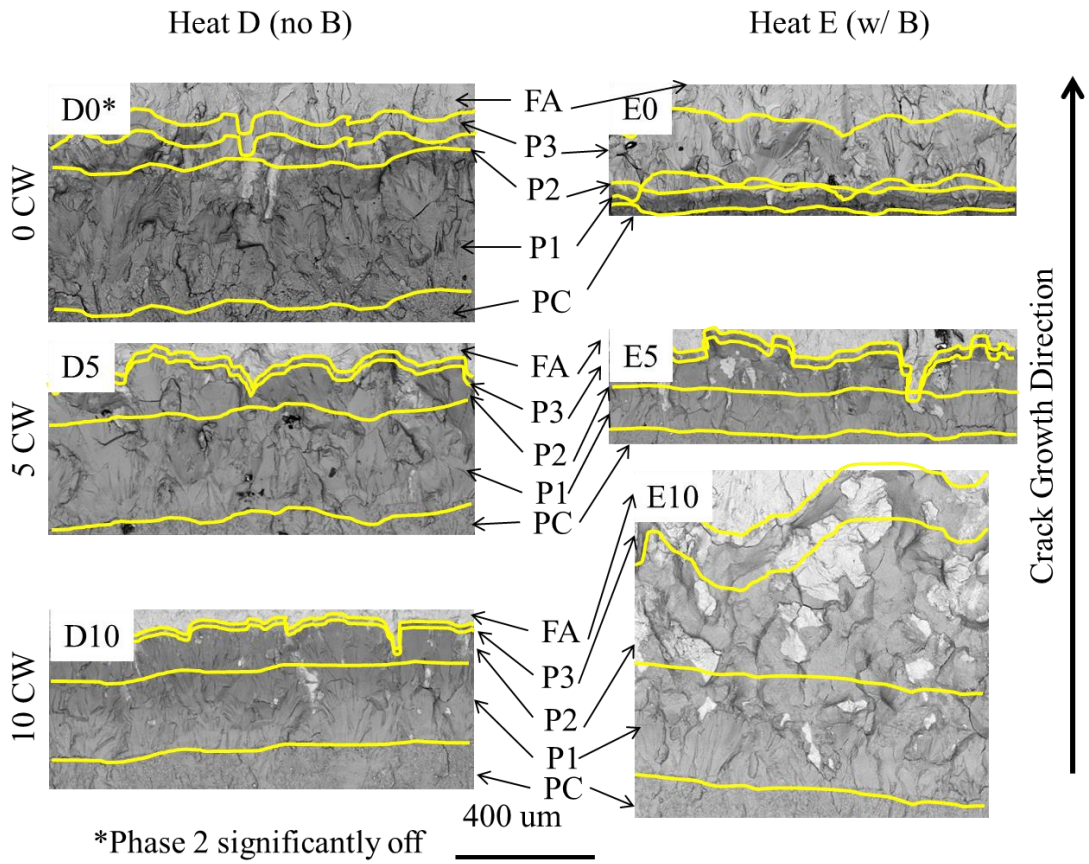

Figure 23: Fracture surface images of mill annealed specimens. Yellow lines indicate approximate test phase boundaries, which are labeled FA for fatigue apart, P3 for phase 3, P2 for phase 2, P1 for phase 1, and PC from precrack. *The estimated for phase 2 cracking in specimen D0 is significantly off from the corrected EPD crack growth estimate.

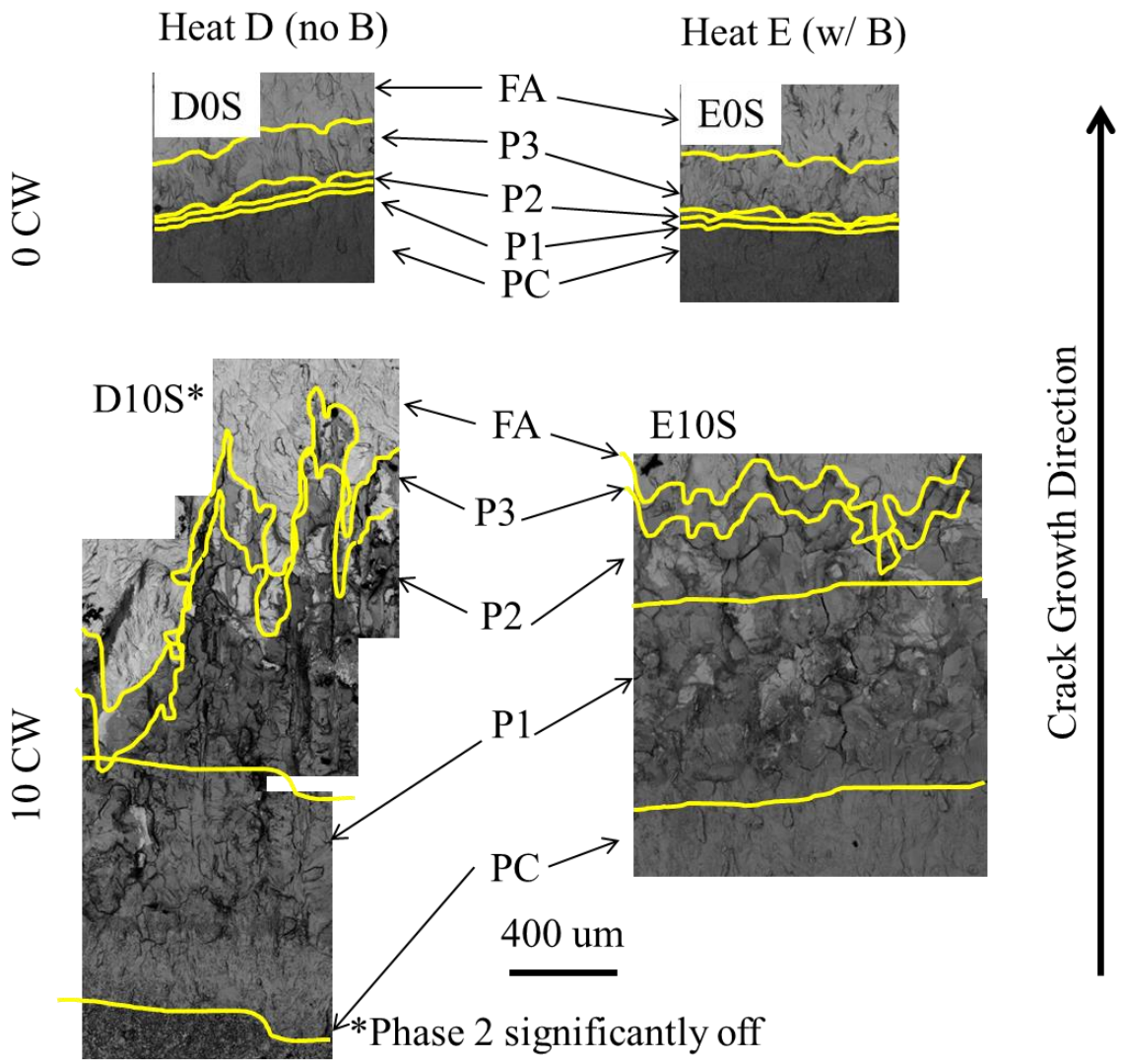

Figure 24: Fracture surface images of sensitized specimens. Yellow lines indicate approximate test phase boundaries. Yellow lines indicate approximate test phase boundaries, which are labeled FA for fatigue apart, P3 for phase 3, P2 for phase 2, P1 for phase 1, and PC from precrack. The estimated for phase 2 cracking in specimen D10S is significantly off from the corrected EPD crack growth estimate due to the high degree of fluctuation.

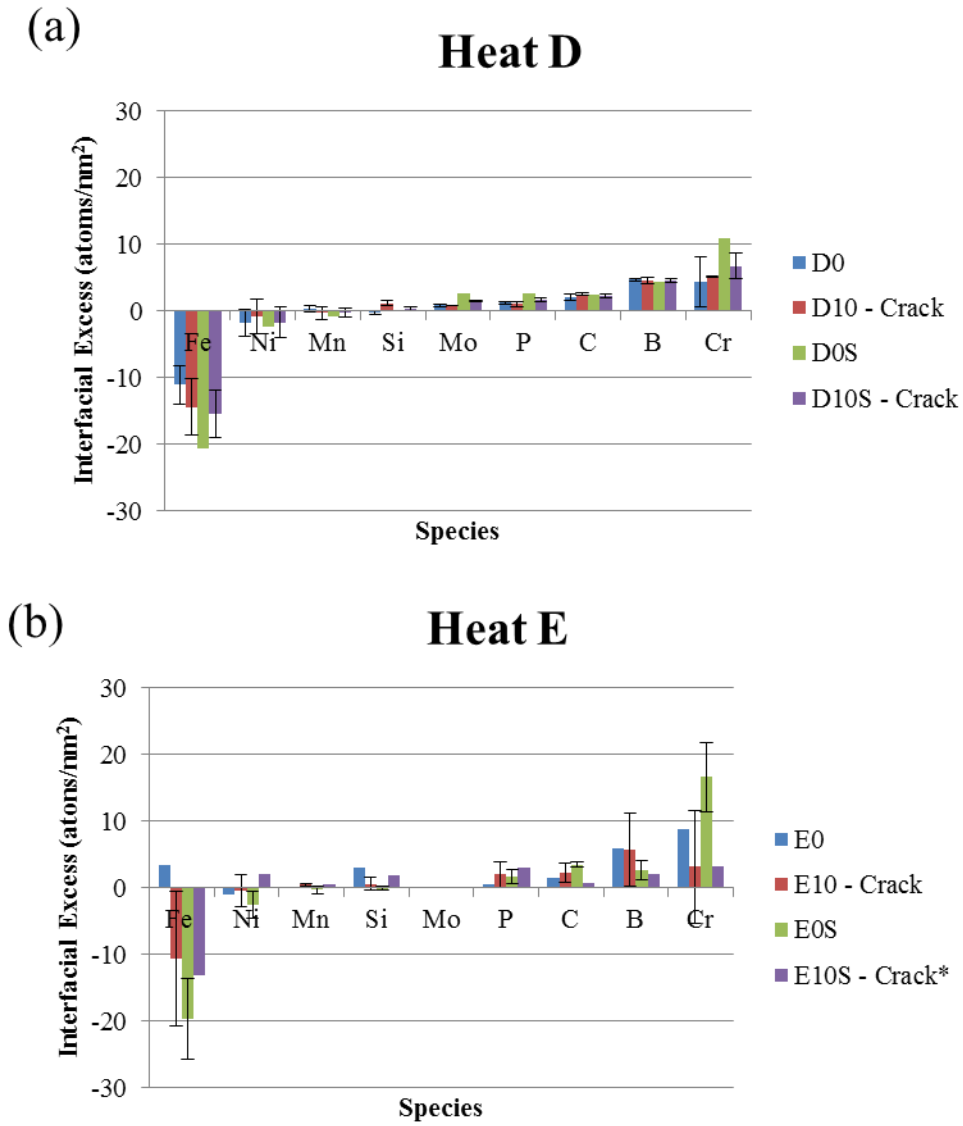

Figure 25: Interfacial excess measurements of elements at the grain boundary based on atom probe tomography results. Negative values indicate depletion and positive values indicate enrichment at the grain boundary. 0% CW specimens were obtained from randomly chosen high angle grain boundaries, while 10% CW specimens were from grain boundaries along which cracks were propagating. *In all cases obvious precipitates were avoided except in E10S. (a) Results from heat D and (b) results from heat E.

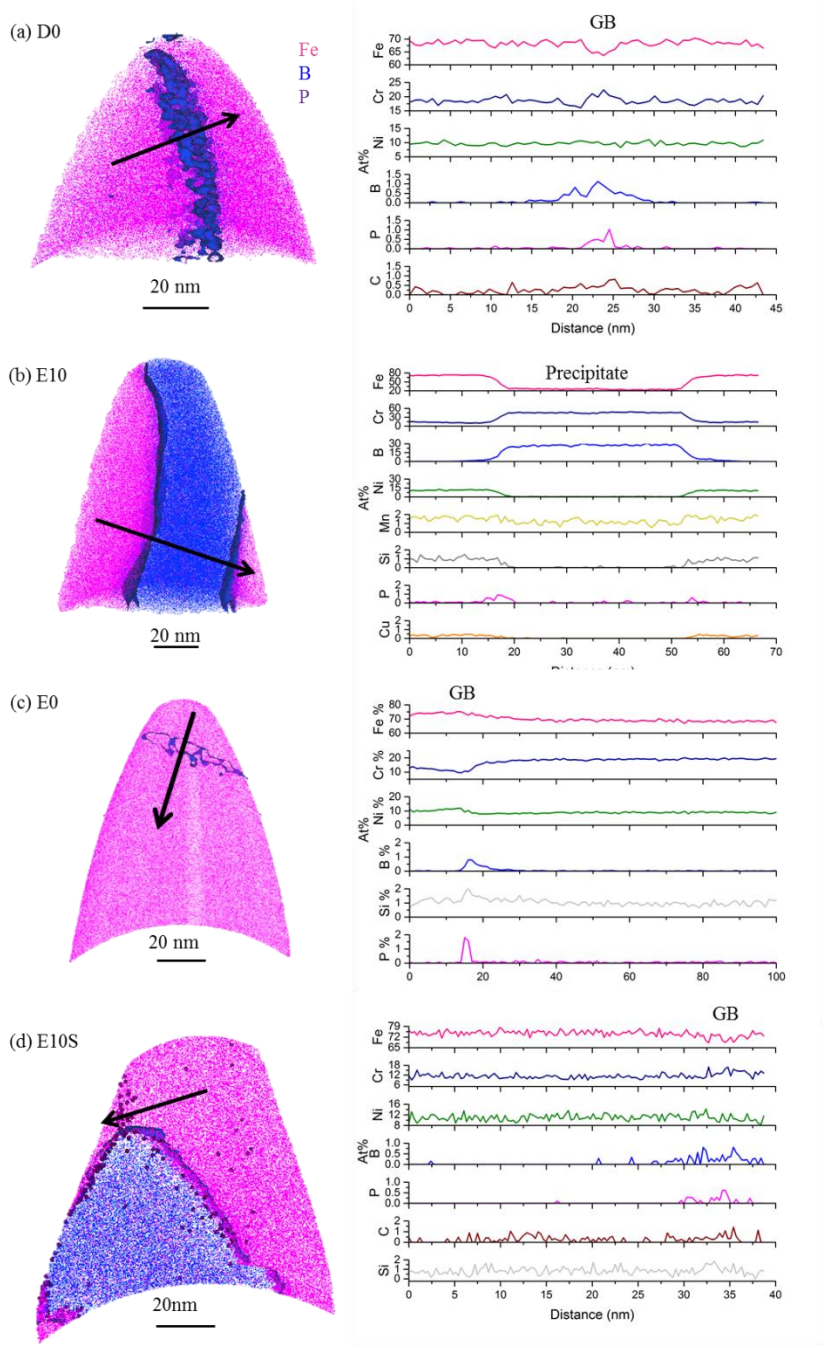

Figure 26: Example APT reconstructions of select GB samples along with 1-dimensional concentration profiles across the areas indicated by the black arrow. In reconstructions pink represents Fe, blue represents boron, and purple represents phosphorous. Grain boundaries and precipitates are outlined with a blue boron isoconcentration surface for visibility. (a) GB in D0 showing the baseline minor element composition. (b) Precipitate from a cracked GB in E10. (c) GB in E0 showing Cr depletion near a precipitate. (d) GB and precipitate along a cracked GB in E10S

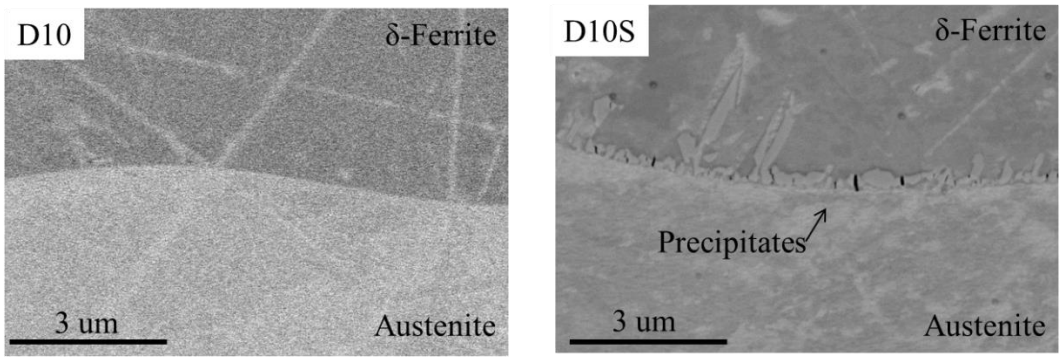

Figure 27: The delta ferrite/austenite interface in heat D before and after sensitization heat treatment.

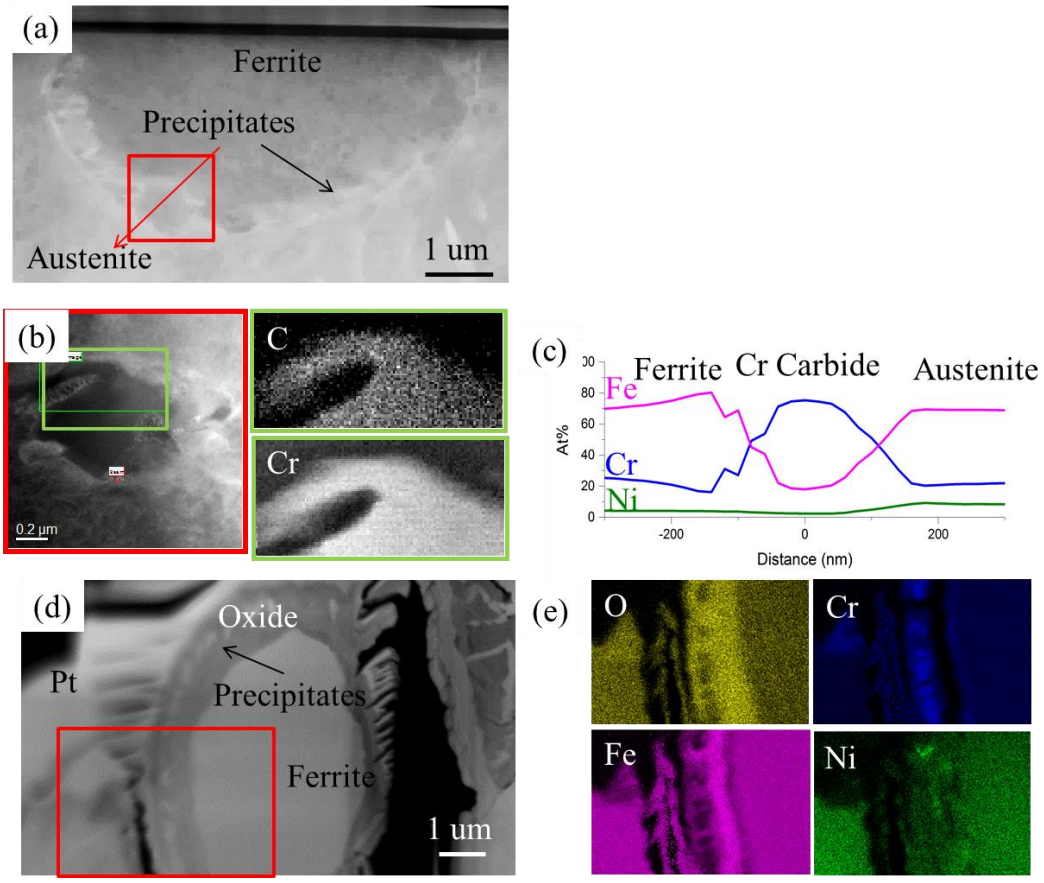

Figure 28: Characterization of the delta ferrite/austenite interface in specimen D10S. (a) TEM image of the cross section of the delta ferrite. (b) EELS maps for C and Cr from the region boxed in red in (a) showing the precipitate is a Cr-rich carbide. (c) EDS line scan of the region indicated by the red arrow in (a) showing the precipitate is rich in Cr and the ferrite is preferentially depleted in Cr. (d) TEM image of an oxidized delta ferrite from the fracture surface of D10S. (e) EDS map of the region boxed in red in (d) showing the oxide is Fe-rich and the Cr-rich precipitates are partially dissolved.

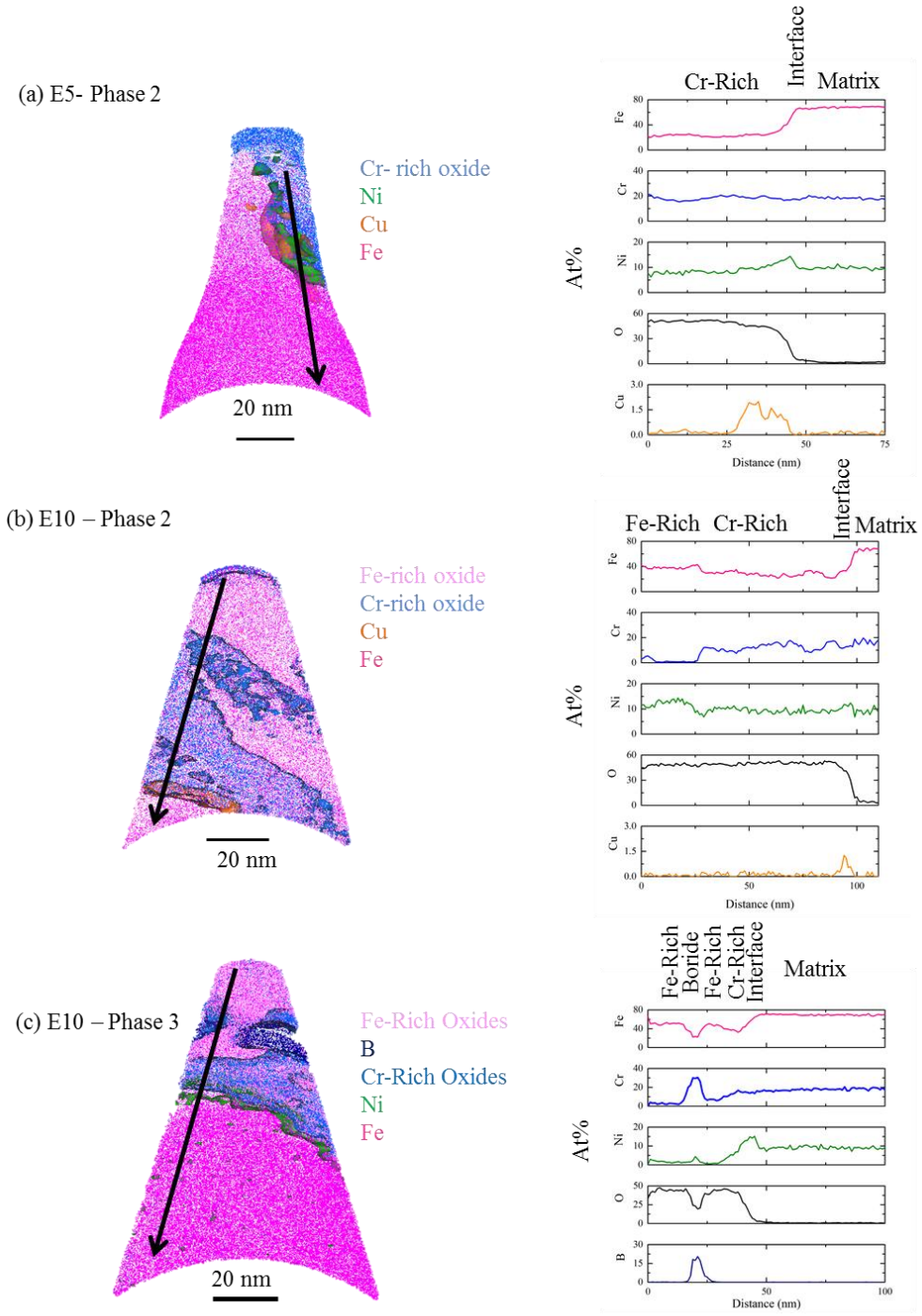

Figure 29: APT reconstructions of oxides from various cracked regions, along with 1-dimensional concentration profiles generated along the arrowed path. (a) An IG crack from a region of phase 2 from the polished cross section of E5. (b) An IG crack from a region of phase 2 from the polished cross section of E10. (c) An IG crack from a region of the phase 3 fracture surface of E10S exhibiting enhanced oxidation, correlating it to boride precipitation and Cr depletion.

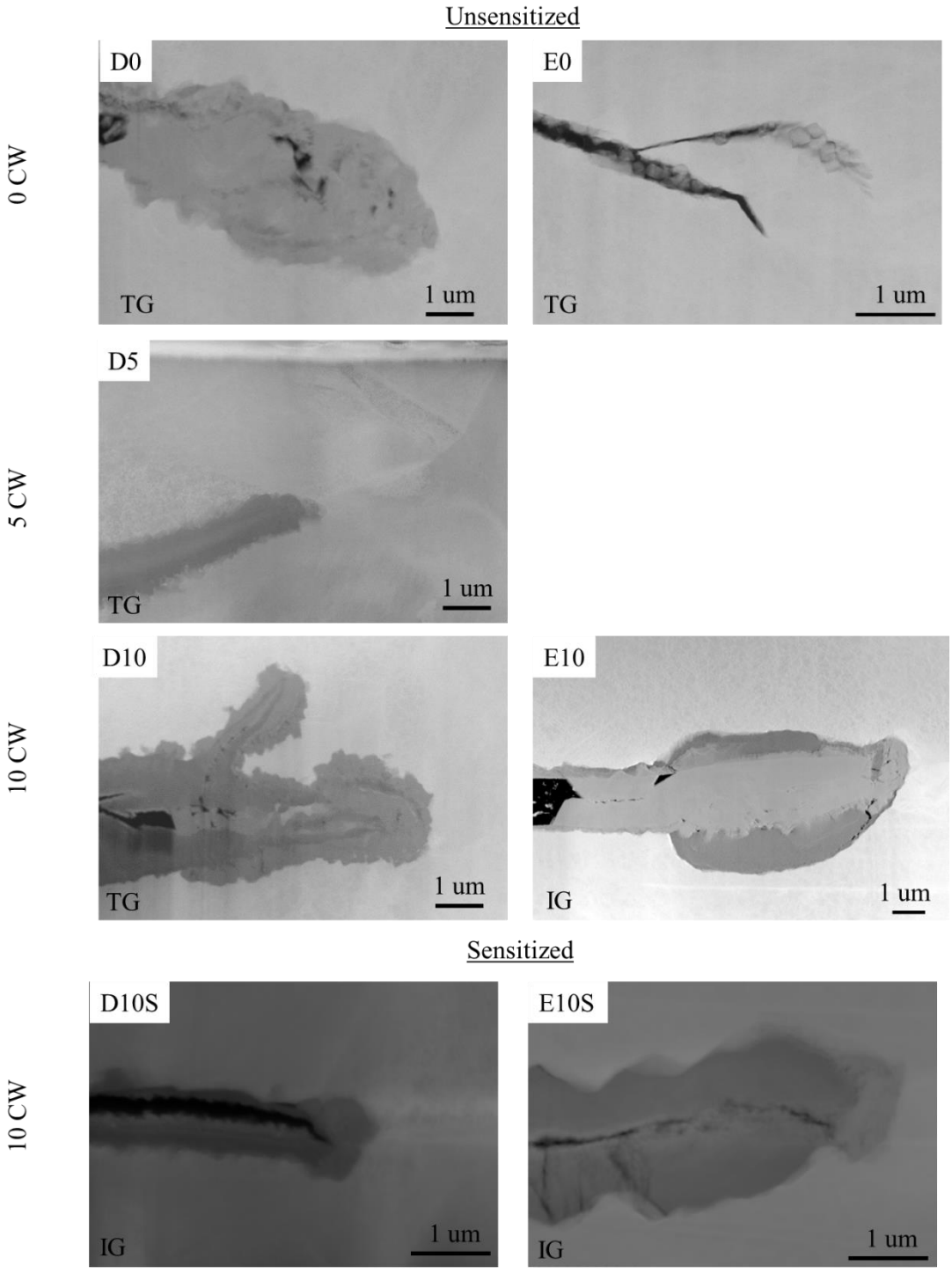

Figure 30: Plan-view TEM specimens from the crack tip of the polished cross section. All except E0 are expected to come from the aerated water test phase based on the thick oxide films observed. The crack mode is listed in the bottom left of each image.

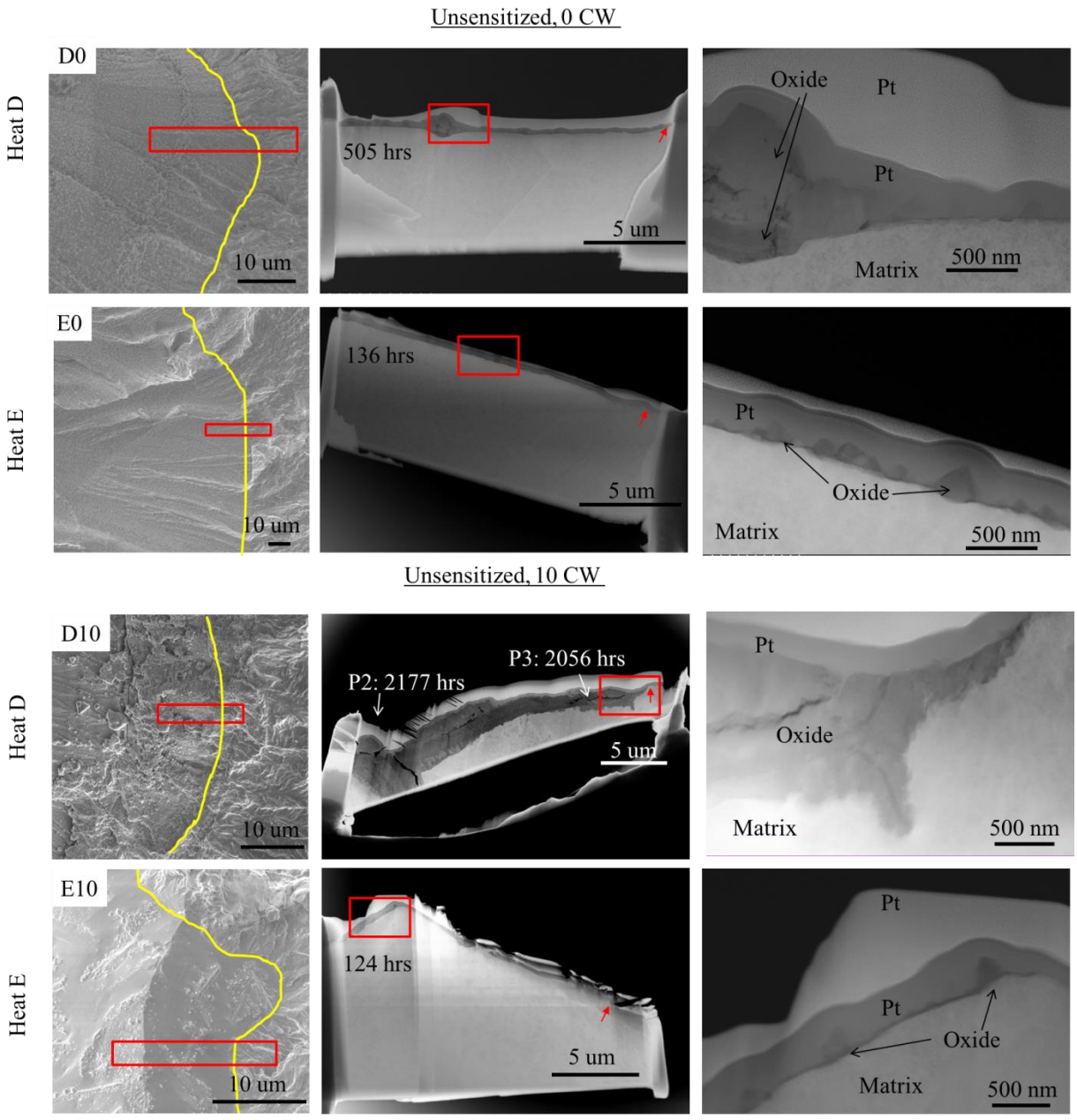
Unsensitized, 0 CW
Heat D
D0
10 um
505 hrs
5 um
Oxide
Pt
Pt
Matrix
500 nm
Heat E
E0
10 um
136 hrs
5 um
Pt
Oxide
Matrix
500 nm
Unsensitized, 10 CW
Heat D
D10
10 um
P2: 2177 hrs
P3: 2056 hrs
5 um
Pt
Oxide
Matrix
500 nm
Heat E
E10
10 um
124 hrs
5 um
Pt
Pt
Oxide
Matrix
500 nm

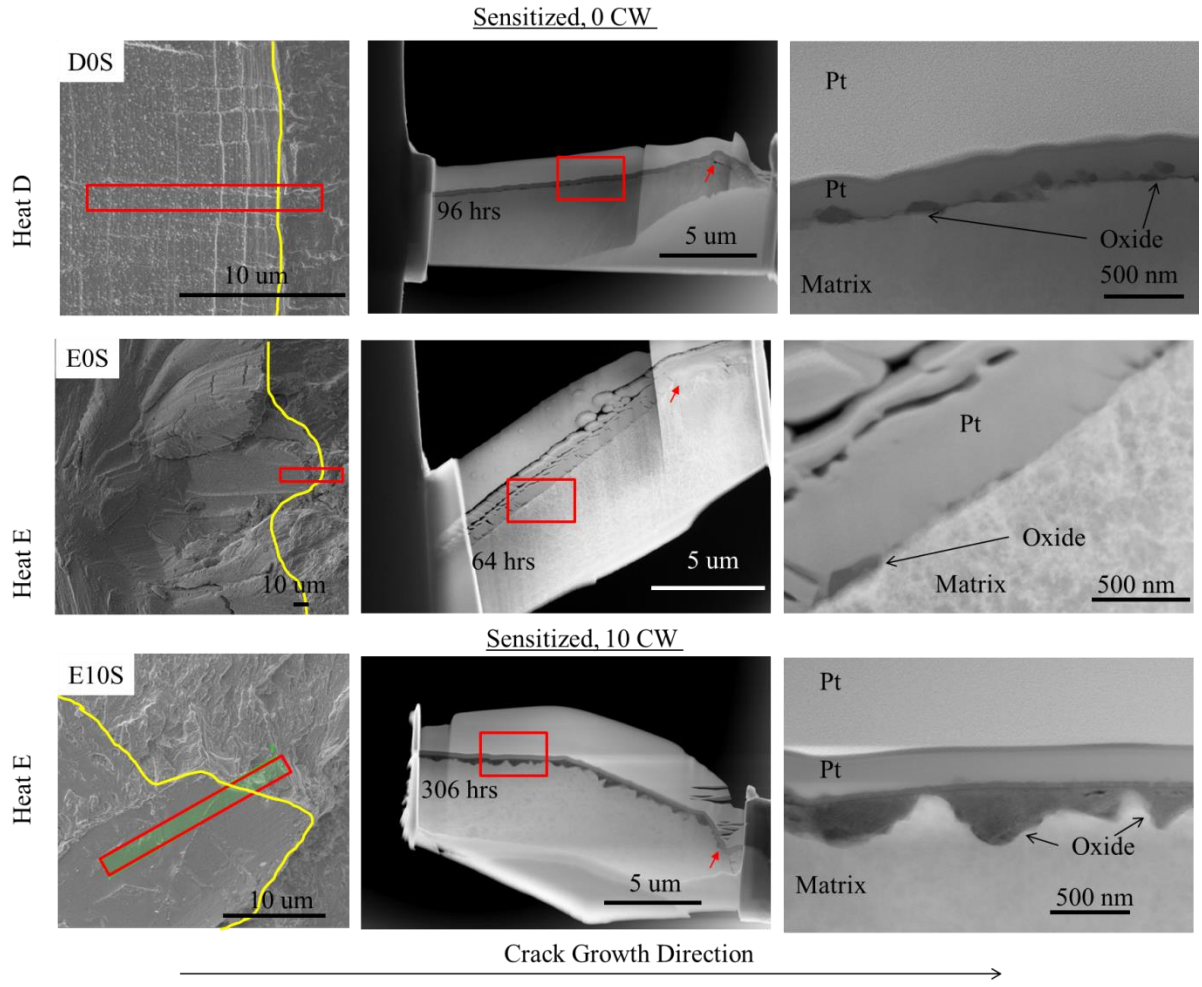

Figure 31: TEM lamella fabricated from one of the farthest extensions of the crack as observed from the fracture surface. The first column of images shows the fracture surface region the specimen was obtained from. The yellow line denotes the phase 3/fatigue apart boundary and the red box indicates the approximate region chosen for lift out. The second column is a low resolution image of the TEM lamella, and the third column is a close up from the red boxed region. All except D10 are expected to be from phase 3 deaerated water. D10 essentially stalled in phase 3, and thus is thought to mostly represent the crack tip from phase 2 aerated water.

CHAPTER 6:

The Effect of Rise Time and Deformation on the Corrosion Response During Corrosion Fatigue Cracking of 304 SS in High Temperature Water

6.1 Introduction

CFC of 304 SS in nuclear reactor components may result from cyclic loading conditions from thermal transients, or mechanical loading such as pump vibrations [100]. Typically, CFC is considered to occur at an enhanced rate compared to fatigue cracking in air [64, 100, 102]. A baseline for environmental enhancement is defined at a low rise time (~5 s), and increasing rise time usually results in increasing levels of enhancement. However, the corrosion fatigue CGR can also be suppressed or retarded [64]. In the case of moderate retardation, or less enhancement, the corrosion fatigue CGR plateaus at increasing rise time, while in complete retardation it falls below the short rise time rate and may even approach the CGR in air [64].

Retardation has been linked to accelerated corrosion that may result from a variety of different factors. High sulfur content in the material or environment, usually due to the presence of MnS that dissolve from the material, results in a thick oxide film due to destabilization of the passive oxide [64, 105]. Long rise and hold times, and increased temperature also allow for increased corrosion response and retardation effects [64, 105], as does high water flow rate [106]. Most of the conclusions relating the CGR to accelerated corrosion have been made based on fractographic examination, while only recently has the oxide and deformation structure been probed in more detail [99, 105].

As has been shown in the previous sections, deformation plays a role in the corrosion response of 304 SS in high temperature water, and thus may have an effect on the retardation of corrosion fatigue crack growth. The current work evaluates the role of deformation in the corrosion fatigue CGR and oxidation response of a heat of low sulfur 304 SS under rise time conditions otherwise expected to promote enhanced or retarded crack growth.

6.2 Materials and experimental details

Two compact tension (C(T)) specimens of a low sulfur heat of 304 SS with composition shown in Table 13 were used for this study. This heat is characterized by intermediate carbon content (0.04 wt%) and low sulfur content (0.001 wt%). Furthermore, this heat exhibits a microstructure consistent with low levels of underlying deformation [151].

Corrosion fatigue tests were run in a number of phases with different rise times on each of the two C(T) specimens. The overall load form was sawtooth in nature, with 85% of each cycling being the rise time and 15% being the fall time. While CGRs are available for each of the test conditions, crack tips are available for analysis only for the final two rise times. The short rise time crack tip specimen was generated at a stress ratio of R = 0.7 and a rise time of 51 s (and a fall time of 9 s). The long rise time crack tip specimen was generated at R = 0.7 and a rise time of 10,200 s (and fall time of 1,800 s), which was expected to potentially result in retardation due to the long rise time coupled with the deformed microstructure. The target stress intensity factor, ΔK, was 10 ksi$\sqrt{in}$ for both tests, and the test temperature was 550 °F (288 °C). Table 14 summarizes the test conditions and crack growth in terms of crack length, number of cycles, and exposure time.

Multiscale characterization of the crack tips was performed using a variety of microscopy techniques. EBSD grain orientation maps were gathered on a Philips XL30 scanning electron microscope (SEM) equipped with TSL OIM. Site specific liftouts of the areas of interest were made using either a Helios 650 Nanolab or Nova 200 Nanolab dual-beam SEM/ focused ion beam (FIB) equipped with an Omniprobe micromanipulator. STEM and energy dispersive x-ray spectroscopy (EDS) was performed on a Hitachi HD-2300A equipped with an Oxford Instruments EDS detector.

6.3 Results

6.3.1 Material properties and microstructure

The material used in this work was solution annealed, yet still exhibits some underlying deformation [151]. The measured material properties are reported in Table 15. The material is not known to have any second phase particles such as MnS or delta ferrites, and is not sensitized and therefore should be free from carbide precipitation.

6.3.2 Crack growth rate

Figure 32 shows the fatigue CGRs as a function of rise time for the different test conditions considered here. For comparison, the fatigue crack growth baselines in both air and deaerated water, and examples of fully retarded and fully enhanced crack growth obtained in other heats of material under similar test conditions, are also shown. The points circled in red correspond to the final test phase (crack tip) for the tests analyzed in these results. This heat of 304 SS exhibits a plateau in CGR at long rise times which is characterized as 'moderately retarded' or 'less enhanced' crack growth compared to full enhancement, in that CGR does not continue increasing dramatically with rise time. However, full retardation is not reached, as the CGR is still significantly higher than the short rise time baseline CGRs in deaerated water.

6.3.3 Multiscale characterization of crack tips and crack flanks

The crack path was characterized using EBSD, and determined to be entirely transgranular over the final test phase under both rise time conditions, as shown in Figure 33. The crack extension was significantly shorter for the long rise time experiment due to the extremely slow cycling rate, despite the extraordinarily longer exposure time. However, the CGR per cycle was higher.

The EBSD maps represent only a single, randomly chosen, cross section of the crack path, and thus cannot immediately be assumed to be representative of the overall crack path. For this reason, fracture surface images of a wider portion of the crack path were obtained from the Naval Nuclear Laboratory, despite the fact that the actual specimens were not available for analysis. The fracture surface images, shown in Figure 34, reveal that the cracking is indeed transgranular throughout. It also reveals details of the oxide structure as viewed from the top down. For 51 s rise time, the oxide particles observed on the surface are very fine and appear to be ordered along fatigue striations. They also diminish in size and number density as the crack tip is approached. A similar phenomenon is observed on the 10,200 s rise time specimen, although the oxide particles are typically more coarse and spaced further apart. These give only an indication of the outer oxide film, however.

Additional characterization of the oxide was performed by preparing a plan-view TEM specimen of the crack tip from each specimen. The crack tip generated under long rise time conditions is shown in Figure 35, along with annotations regarding the approximate crack growth time, an EDS map highlighting the oxide composition, and a transmission Kikuchi diffraction

(TKD) map highlighting potential regions of deformation ahead of the crack tip [153]. The TEM image reveals that the crack tip itself is very blunt with a diameter of ~0.9 um. Furthermore, in the final ~6 um of the crack tip there is essentially no oxide film present, with the exception of a single large oxide particle. Farther back along the crack path, with approximately 140 hours of exposure, an inner and outer oxide film was developed. The inner oxide (adjacent to the metal) is Cr-rich with varying Fe/Cr ratio (~30-50% Fe depending on measurement), and the outer oxide particles (filling the crack) are Fe-rich. Additional silicon dioxide particles are observed in the crack as a result of the mechanical polishing procedure used and should be ignored. No appreciable Ni or Cu enrichment was observed at the oxide/metal interface, but some Ni is incorporated into the inner oxide film and outer oxide particles. The TEM image and TKD map highlights the possibility of a deformation microstructure emanating from the crack tip at about a 45° angle. The measured misorientation from one side of the crack tip to the other is approximately 7°. It should be noted that the specimens were prepared using Ga^{+} ions in the FIB, which is known to impart damage into the specimen [154]. To minimize the damage low kV cleaning was performed. It cannot be conclusively determined if the damage structure is a byproduct of cracking or the FIB polishing. However, similar damage microstructures have been reported in FIB specimens cleaned using a NanoMill [105], providing evidence that the microstructure observed here is most likely also crack-induced.

The crack tip specimen gathered from the 51 s rise time specimen (Figure 36) is very different in appearance compared to the 10,200 s specimen. First, the crack itself was generated in a very short period of time, so the extent of the crack captured in the TEM lamella only represents about 0.7 hours of crack growth. Within this region essentially no oxide of any kind is observed. The crack tip diameter in this specimen is ~0.5 um, and still appears rather blunt. An additional TEM specimen, shown in Figure 37, was made approximately 450 um behind the crack tip, corresponding to near the beginning of the short rise time test and corresponding to approximately 50 hours of exposure. In this specimen, a dual layer oxide is observed, with an inner layer of about 150 nm in thickness, and a fine oxide particle of similar size, as shown in the close up in Figure 37b and the EDS line scan in Figure Figure 37c. The inner layer is enriched in Cr compared to the outer oxide, but still has a high Fe/Cr ratio, in contrast to the oxide chemistries measured in surface and SCC tests.

6.4 Discussion

Recently, corrosion fatigue retardation mechanisms in high temperature water have been associated with factors that promote accelerated corrosion, such as increased sulfur content and high water flow rates [64, 106]. When coupled with factors such as a long rise or hold times, which increase the time allowed for corrosion, full retardation to fatigue levels close to that of air may be reached [64].

The CGRs measured in this material over a range of rise times, as shown in Figure 32, correspond to only slightly less enhanced crack growth than the fully enhanced curve obtained from a different material. The CGR does, however, plateau, and even appears to start turning downward at the very long rise times, consistent with a moderately retarded, or less enhanced crack growth pattern. This level of retardation in this material was previously speculated to result from accelerated corrosion due to the underlying deformation level [151]. Oxidation results in Chapter 4 relating the oxide structure and thickness to surface deformation indicated a modest difference in thickness and growth rate depending on surface deformation level. Furthermore, the deliberate deformation of up to 10% CW imparted to SCC specimens in Chapter 5 did not yield any obvious correlation to increased oxidation response of the material. In these terms, with the relatively low levels of deformation in this material and modest oxide thicknesses, incomplete retardation due to deformation induced corrosion is not surprising.

Examination of the fracture surface revealed discrete outer oxide particles forming along fatigue striations. In the long rise time specimen the particles are larger and more spaced out, while in the short rise time specimen they are finer and more densely packed. However, examination of the crack tip of both specimens revealed very little inner oxide product in the crack tips (Figure 35 and Figure 36). In both specimens the inner oxide farther back on the crack flank had a thickness approximately commensurate with what would be expected based on the exposure time of that region (Figure 35 and Figure 37). The absence of inner oxide in the crack tip region, however, suggests that its growth occurs after the passage of the crack has occurred, and thus is not associated with the crack propagation mechanism.

These results are consistent with previous examination of the oxides formed in corrosion fatigue specimens under short and long rise time conditions of a different low sulfur material, where only outer oxide particles were observed in the crack tip region, and no inner oxide was observed until well behind the crack tip [99]. However, in that low sulfur material, no evidence

of slight retardation was observed [99]. The main difference appears to be in the crack tip morphology. In the specimens reported here, the crack tips are wide and blunted, while in previous work under fully enhanced conditions the crack tip remained sharp [99].

Blunting serves to reduce the effective ΔK driving force for fatigue crack growth, thereby reducing the fatigue CGR [105, 108]. Two mechanisms of crack tip blunting can be explored. One such mechanism is chemical blunting by enhanced dissolution of the crack tip [108, 155]. Enhanced dissolution would be expected to be accompanied by enhanced oxide product, at least in the form of re-precipitated Fe oxide particles. While some of these particles are observed ~6 um behind the crack tip in long rise time specimens, and from fracture surface examination, they appear less numerous than in previous investigations of fully enhanced cracks [99]. They also appear to be correlated to fatigue striations which may suggest they are a byproduct of outward solid state growth enhanced by the residual deformation in the crack flank leftover from the crack passage. However, this correlation could not be examined from the plan-view crack tip specimens.

The other mechanism for blunting is by a mechanical process. Newer work has correlated deformation ahead of retarded cracks with mechanically blunted crack tips, and speculated that hydrogen diffusion ahead of the crack tip plays a role [105]. In that work, a damage plume of increased dislocation structure was observed emanating ahead of the crack tip in specimens exhibiting fully enhanced and slightly retarded CGRs [105]. This appears similar to the region of damage highlighted in the TKD map of the long rise time (slightly retarded) specimen examined here (Figure 35c), although comparable high resolution dislocation analysis was not performed.

It was speculated that long rise times allow increased time for hydrogen diffusion to the crack tip region [105, 156]. As discussed previously, hydrogen may be present as a corrosion product, from the water itself, or from the material. Hydrogen acts to activate slip systems by reducing the stress required for activation, thereby causing mechanical blunting [105, 156]. Furthermore, hydrogen tends to concentration in highly stressed regions [156]. While previous work has attributed high hydrogen concentrations to corrosion byproduct in sulfur containing materials resulting in cracking [64, 105], the underlying deformation structure in the material tested here, even without crack induced deformation, may promote enhanced hydrogen uptake in the material [157]. While the long rise time crack tip appeared more blunted in this work, the CGR remained elevated compared to the base line, suggesting that such blunting was not as

effective at retarding crack growth as it was when accompanied by accelerated corrosion where CGR reduction below the baseline was observed [105]. However, the crack tip generated in short rise time experiments was also blunted, although to a lesser extent. This specimen would not have had increased time for hydrogen diffusion due to the short rise time and overall test duration, but still exhibited blunting and some level of retardation compared to fully enhanced crack growth curves. Thus, if a hydrogen mechanism is at play, this suggests that hydrogen trapping by the deformed microstructure is not highly dependent on time.

Hydrogen is extremely difficult to observe using currently available analytical microscopy techniques, so its role in CFC is currently mainly speculative. However, recent work has started to examine the damage structure of crack tips, instead of relying only on fracture surface examination where the crack tips are destroyed [105]. While high resolution characterization of the damage structure was not performed in this work, analysis of the crack tip allowed for an understanding of the role of corrosion in the possible mechanisms leading to mild retardation. While accelerated corrosion was expected to play an enhanced role due to the underlying deformation microstructure, the crack tip was devoid of corrosion products. Thus, the results were analyzed in terms of a potential hydrogen mechanism, but further work would clearly be necessary to justify the explicit role of hydrogen.

6.5 Conclusions

While usually corrosion fatigue CGRs of 304 SS are enhanced compared to CGRs in air, and continue to increase with rise time, certain conditions have been found to retard CGRs with increasing rise time. These conditions, thus far, have been linked to factors that accelerate corrosion mechanisms. The current work analyzed the role of underlying deformation in the corrosion mechanism and corrosion fatigue CGR of a heat of low sulfur 304 SS under various rise time conditions.

1. The corrosion fatigue CGR was accelerated with respect to the air and environmental baselines under all rise time conditions. However, at long rise times the CGR plateaued and even started to decrease slightly, while at shorter rise times it still exhibited lower CGR than fully enhanced materials. Thus, the material was determined to exhibit mildly retarded, or less enhanced crack growth over a wide range of rise times.

2. Initial hypotheses were that underlying deformation resulted in accelerated corrosion in the crack tip area during long rise time experiments. Analysis of the crack tip from the fracture surface, and from a plan-view specimen fabricated to capture the actual crack tip, failed to identify significant corrosion product. Instead, corrosion product was essentially commensurate with the expected amount based on the exposure time, and appeared to occur after the crack had already advanced.
3. Crack tip investigation did, however, reveal that under both rise time conditions the crack tip was blunted, with more extensive blunting occurring after long rise time. Blunting may occur due to chemical or mechanical factors, but chemical dissolution would be expected to result in additional corrosion product formation. Thus mechanical blunting seems more likely and may be associated with hydrogen uptake into the material.
4. It was speculated that the underlying deformation microstructure allowed for enhanced hydrogen uptake and resulted in mechanical crack tip blunting, although no direct evidence for this mechanism was gathered.

Table 13: Composition (wt%) of dual certified 304/304L SS used in this study

C	N	Mn	P	S	Si	Cr	Ni	Co	Cu	Mo
0.04	0.039	1.49	0.026	0.001	0.36	18.43	8.85	0.08	0.18	0.29

Table 14: Summary of test conditions for corrosion fatigue tests

	Short rise time	Long rise time
Temperature (°F)	550	
R	0.7	
ΔK (MPa√m)	11	
ΔK (ksi√in)	10	
Load form	Sawtooth	
Rise time (s)	51	10,200
Fall time (s)	9	1,800
Crack Growth Rate (in/cycle)	5.54E-6	9.77E-6
# cycles	3240	294
Total Crack Growth (um)	488	75
Total Exposure time * (hr)	54	980

*at region of longest exposure

Table 15: Material properties of dual certified 304/304L SS at 550 °F

Property	Value
Yield Stress (ksi)	22.5
Ultimate Stress (ksi)	60.5
Flow Stress (ksi)	41.5
Elastic Modulus	26

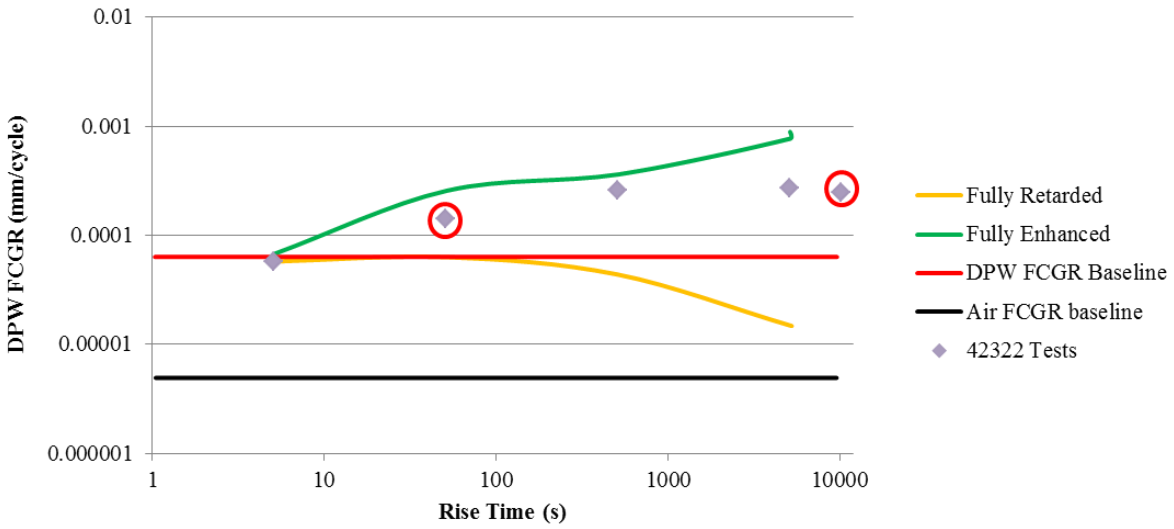

Figure 32: Corrosion fatigue crack growth rate for the material studied (blue squares) compared to typical fully enhanced (green) and fully retarded (yellow) corrosion fatigue crack growth curves obtained from other heats of material. The baseline curves equivalent to crack growth at short rise time for corrosion fatigue crack growth rate in air (black) and deaerated pressurized water (red) are also shown. This material exhibits 'slightly retarded' or 'less enhancement' compared to fully enhanced crack growth rate at long rise times.

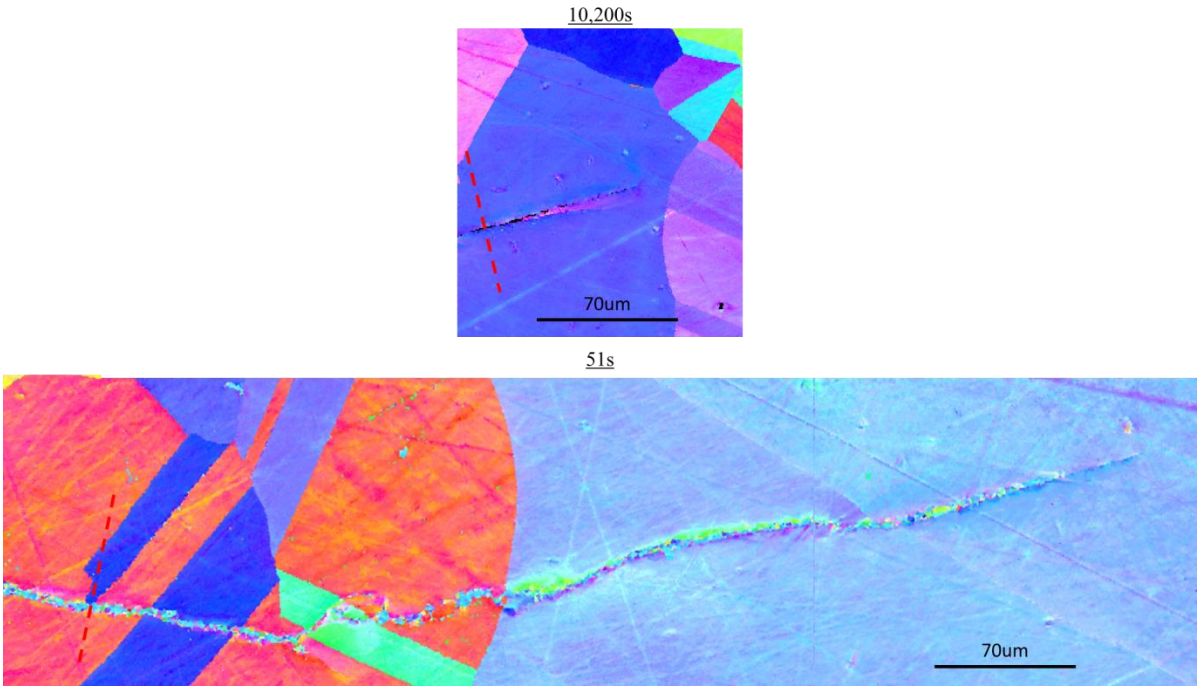

Figure 33: EBSD maps of the crack path in each specimen. The red dashed lines denote the approximate start of the test phase. Both cracks propagate completely transgranularly.

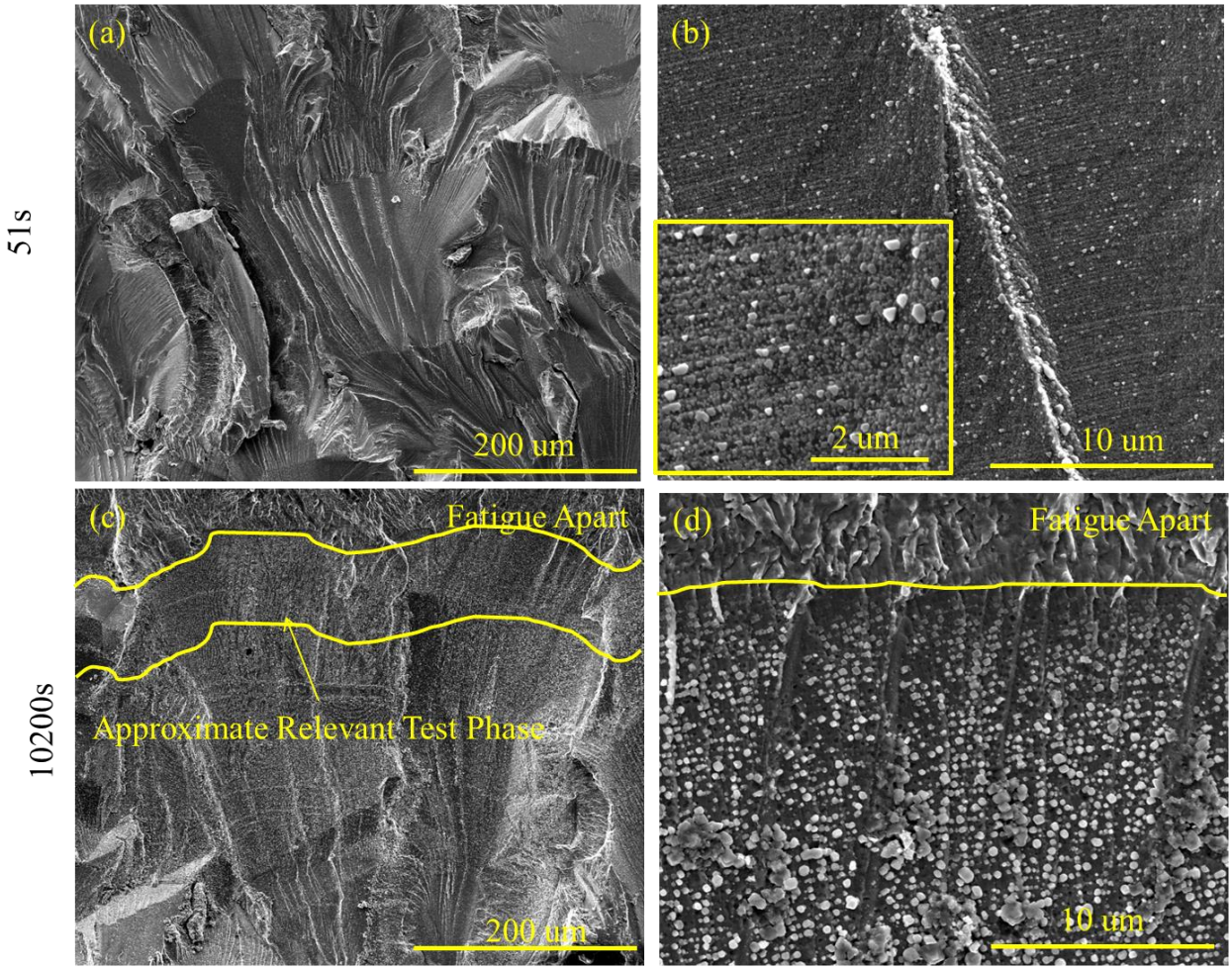

Figure 34: Fracture surface images from the short, 51 s rise time (a and b) and long, 10,200 s rise time (c and d) after the specimens were fatigued apart obtained by Bryan Miller at the Naval Nuclear Lab. Evidence of oxide particles is apparent in the higher magnification images of both specimens (b and d), but the morphology is different.

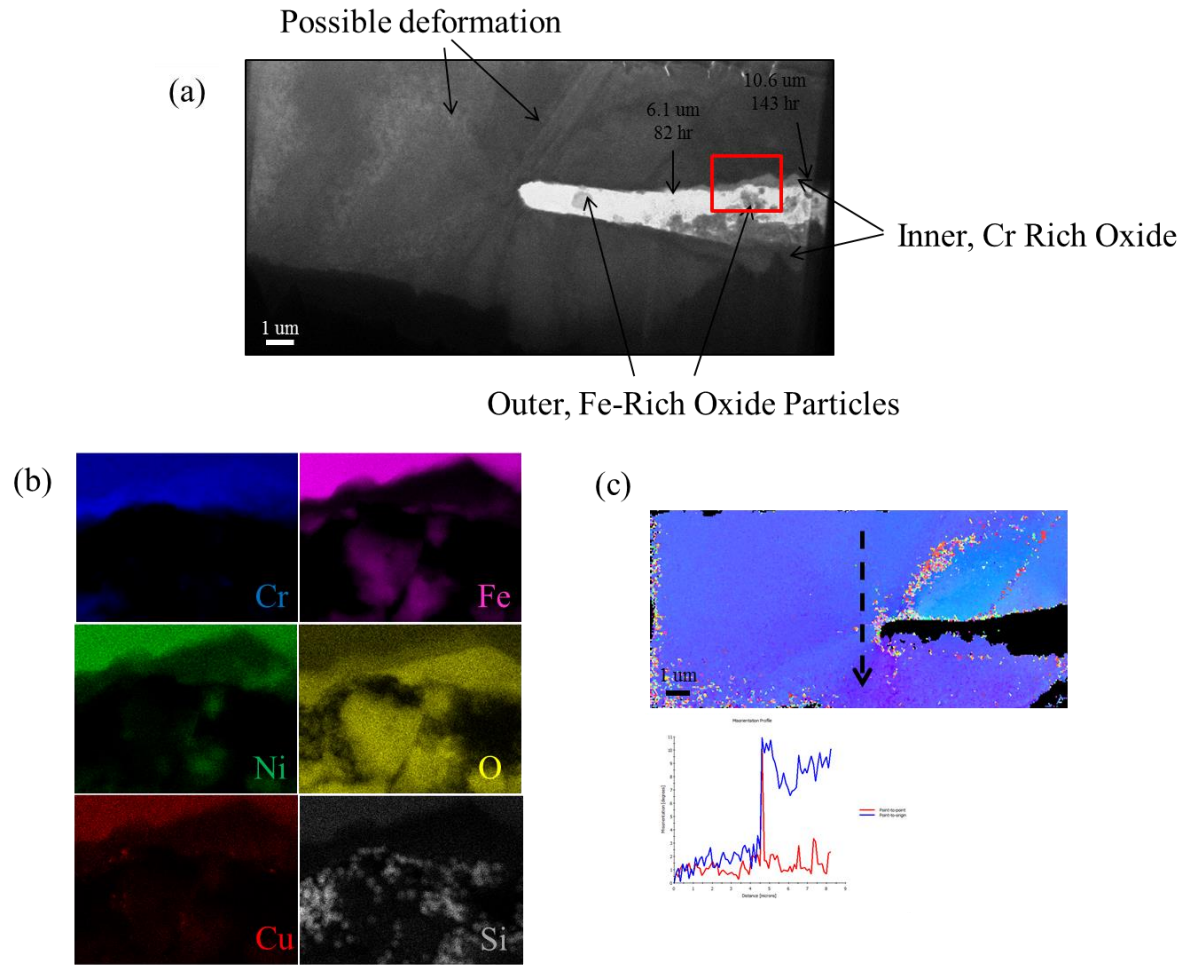

Figure 35: Analysis of the 10,200 s rise time specimen. (a) TEM image of the crack tip revealing the oxide morphology in the crack tip and possible deformation in the matrix. (b) EDS map from the region boxed in red in (a) revealing the oxide is composed of two layers, and inner, Cr-rich layer adjacent to the metal and outer, Fe-rich oxide particles. Oxide is only observed well behind the crack tip. (c) TKD map of the specimen indicating crack induced deformation. The misorientation measured along the dashed line is approximately 7° indicating underlying deformation structure.

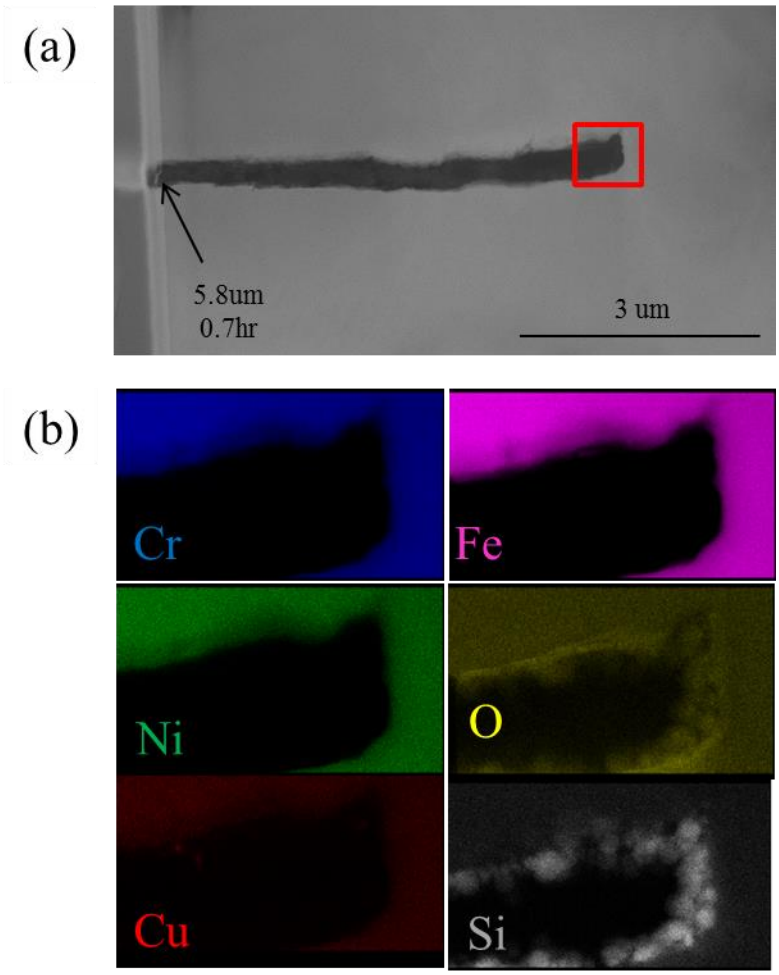

Figure 36: Analysis of the 51 s rise time specimen. (a) Image of the TEM specimen revealing essentially no oxide in the crack mouth. (b) EDS map of the region boxed in red in (a) confirming no real oxide is present in the crack tip.

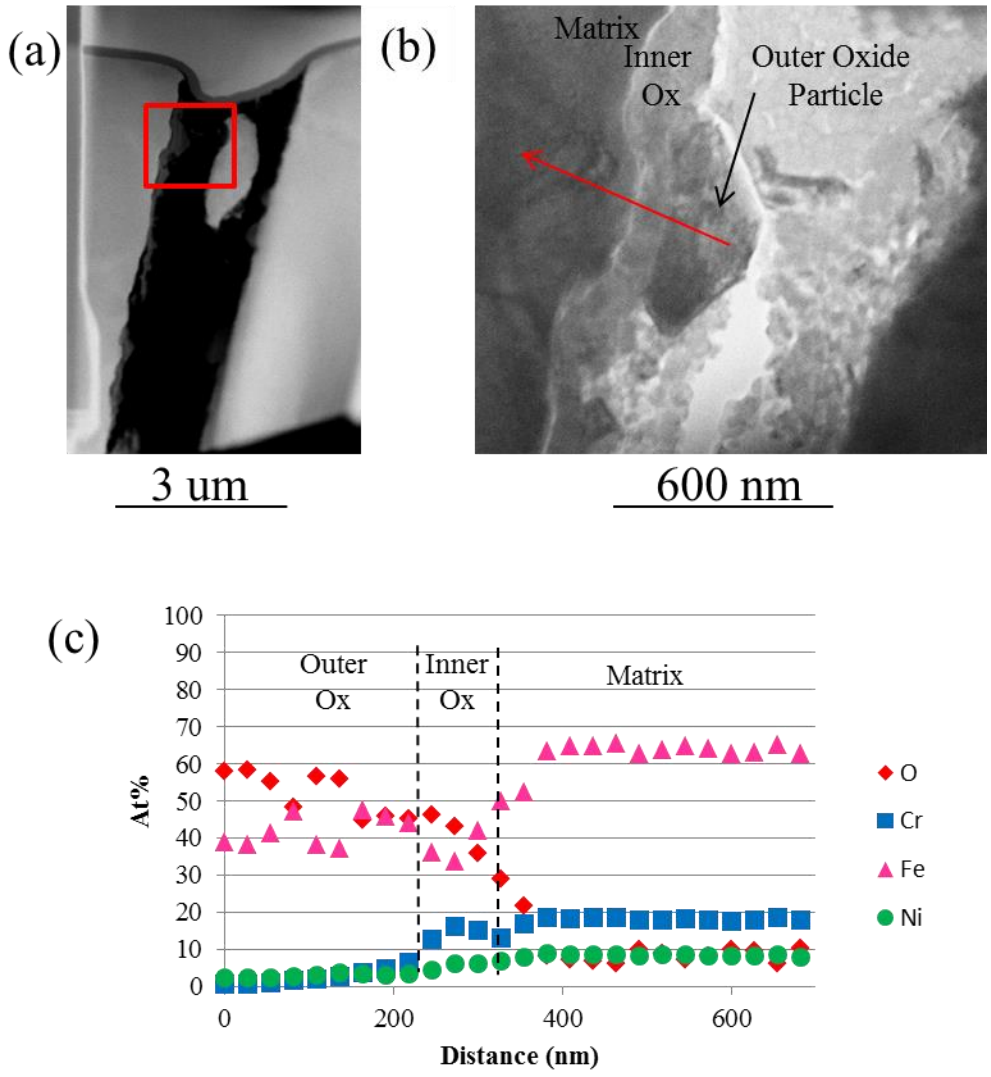

Figure 37: Analysis of the oxide of the 51 s rise time specimen from approximately 450 um behind the crack tip, corresponding to about 50 hours of exposure. (a) TEM image of the specimen. (b) Close up TEM image revealing a two layer oxide structure. (c) EDS line scan highlighting the chemistry of the oxide regions. The inner oxide is slightly enriched in Cr and depleted in Fe compared to the outer oxide, which is Fe rich.

CHAPTER 7:

Summary, conclusions, and future directions

7.1 Summary and conclusions

This work has focused on understanding the relationship between deformation and oxidation of various heats of 304 SS in a variety of corrosion processes that may occur in pressurized water nuclear reactors. The main findings are summarized below.

7.1.1 Atom probe tomography of oxides

APT was identified as a tool that could be used to characterize the oxide products at a very fine scale in order to contribute to the understanding of the oxidation processes. In order to effectively use APT, however, appropriate analysis conditions and reconstruction parameters for the materials of interest had to be identified. Pure oxides of types related to those expected to result from high temperature aqueous corrosion on 304 SS were obtained and studied systematically to understand the role of different analysis and reconstruction parameters on the measured results.

1. The analysis conditions can have a profound effect on the measured chemistry of some oxides. Conditions that promote more accurate composition measurements are typically high field conditions such as higher detection rate or lower pulse energy. This was attributed to the reduction of multihits, which were shown to correlate with oxygen deficiency.
2. Unfortunately the conditions that promote accurate stoichiometry were found to promote decreased yield, particularly in interface-containing specimens, and thus were not used in the current work.
3. Despite off-stoichiometric measurements, oxide phases could still be distinguished based on differences in the measured stoichiometries at the analysis conditions that were used.

7.1.2 Surface oxidation

The role of deformation in the high temperature aqueous oxidation response of 304 SS has not been adequately determined, despite the fact that deformation has been implicated in playing

a role in SCC and potentially CFC in similar environments. The early stages of oxidation on ground surfaces was studied and compared to electropolished surfaces using APT and TEM in order to better understand the explicit role of deformation in the oxidation response.

1. Consistent with previous literature, a dual layer oxide structure grows on 304 SS surfaces exposed to high temperature water.
    a. The outer oxide layer is composed of discrete particles identified as magnetite, with some Ni incorporated. They grow in size and number density with increasing exposure time, and are more prevalent on ground surfaces than electropolished surfaces.
    b. The inner layer is a nanocrystalline mixed Fe/Cr layer. This work shows that the inner oxide layer stoichiometry and microstructure develops according to the underlying deformation characteristics of the material.
        i. On electropolished surfaces, the oxide layer is homogeneous in thickness and chemistry. The stoichiometry develops from a chromium rich phase to a mixed Fe/Cr phase over time. Ni is incorporated into the oxide at nearly the original matrix levels.
        ii. On ground surfaces, the oxide layer varies widely in thickness in accordance with the underlying deformation. Furthermore, the oxide chemistry is highly non-uniform, with separate regions richer in Cr and adjacent regions of mixed Fe/Cr level.
2. Interfacial segregation differs according to the underlying deformation structure. On the ground surface, discontinuous pockets of Cu and Ni are sometimes found at the interface. Cu is thought to accumulate by rejection from the oxide due to its high electrochemical nobility, while Ni is either rejected or enriched by the selective oxidation of Cr. In the electropolished case, Ni was incorporated into the oxide layer, while Cu was observed at levels higher than expected based on the amount of Cu in the material. This suggests that Ni-enrichment occurs due to mechanisms related to the underlying deformation. A mechanism for Cu enrichment has been proposed, but future experiments to verify the source and role of Cu are suggested.
3. A mechanism taking into account the underlying surface deformation was proposed, and is an expansion of the previously proposed solid state growth mechanism. Sub-surface

oxidation and the different regions of oxides in the inner layer of ground specimens suggest a mechanism in which Cr is rapidly preferentially oxidized due to the presence of short circuit diffusion pathways. Fe and Ni are rejected from the rapidly formed oxide, but eventually oxidize in adjacent regions, leaving regions of distinct chemistries within the oxide layer. In the absence of deformation, the oxidation process is completely governed by the rate of diffusion of species through the oxide layer, without taking into account the role of fast diffusion pathways.

7.1.3 Stress corrosion cracking

SCC in 304 SS in high temperature water has previously been linked to GB Cr depletion during sensitizing heat treatment, and high levels of CW. In order to circumvent the issue of Cr depletion, low carbon heats of 304 SS have been adopted. Two heats of dual certified 304/304L SS were evaluated for their SCC response in mill annealed and sensitized conditions, aerated and deaerated water, and with varying levels of deformation.

1. Dual certified 304/304L SS, despite its low bulk carbon content, can be sensitized by different mechanisms depending on other microstructural and microchemical features.
    a. In materials with elevated boron, sensitization occurs by the precipitation of Cr-rich borides at the GB, which depletes the surrounding GB sufficiently to be susceptible to attack in oxygenating conditions.
    b. In materials with delta ferrite, sensitization occurs by Cr-rich carbide precipitation at the delta ferrite/austenite interface due to the faster diffusion coefficient of Cr in the delta ferrite phase. Cracking then primarily occurs along the Cr depleted region of the delta ferrite/austenite interface.
2. In both types of sensitization, the oxidation occurs readily in Cr depleted regions, whether in the delta ferrite phase or grain boundaries. Due to the underlying microchemistry, this oxide is deficient in Cr and rich in Fe, and thus does not have the protective nature usually associated with a Cr-rich oxide film. SCC is presumed to primarily occur according to a slip-dissolution mechanism previously used to describe IGSCC in sensitized 304 SS, where dissolution occurs readily due to the non-protective nature of the film, and cracking occurs through the oxide layer [87].

3. Sensitization, alone, however is not sufficient to promote IGSCC in these materials. Instead, it must be coupled with deformation to levels of at least 10% CW for accelerated IGSCC response, and even then primarily only in aerated water. The explicit role of deformation is still unclear, as deformation alone is also not sufficient to promote IGSCC. It therefore interacts with the sensitization and thus may play a role in accelerating the oxidation process, as observed on surface oxidation experiments.
4. The oxidation response observed in crack oxides does not exactly parallel that observed on surface oxides. In regions examined from aerated water the oxide is relatively uniform in composition without exhibiting features relating to the underlying deformation, yet Ni is apparent at the oxide/metal interface. In regions examined from deaerated water only a very thin oxide is observed even at longer exposure times, except in regions depleted in Cr in which accelerated oxidation was observed. Cu was observed at low levels at the oxide/metal interface of some specimens, consistent with the low levels observed at the interface of ground specimens.

7.1.4 Corrosion fatigue cracking

CFC of 304 SS in high temperature aqueous environments is a topic that has only recently garnered interest. It has been found that different heats of 304 SS may respond differently to corrosion fatigue, with some exhibiting enhanced cracking compared to a baseline value, and others exhibiting retardation. Some heats can even reach retardation down to CGRs comparable to those found in air. Up until now corrosion fatigue retardation has largely been associated with conditions that accelerate corrosion product formation within the crack, although no mechanism for retardation has been agreed upon. A heat of 304 SS that exhibited low levels of deformation was evaluated for its corrosion fatigue response with particular attention paid to its corrosion response.

1. The corrosion fatigue response of the material tested plateaued at long rise times, exhibiting less environmental enhancement than fully enhanced corrosion fatigue crack growth, but not as much as fully retarded corrosion fatigue crack growth.
2. The reduction in enhancement could not be linked to accelerated corrosion in the crack tip due to the underlying deformation in the material.

3. The reduction in enhancement was presumed to be linked to the severe crack tip blunting that was observed. A mechanism of blunting was speculated to relate to increased hydrogen uptake aided by the underlying deformation of the material, although no direct evidence of this mechanism was observed at this time.

These results highlight the complex nature of these corrosion processes. However, some conclusions on the role of deformation have become clear. First and foremost, deformation certainly can and does play a role in the general corrosion process, as outlined by the differences observed in the oxide product between electropolished and ground surfaces. Furthermore, this work has highlighted that the process, while consistent with the general mechanisms previously reported in the literature, is much more complex than the simple generation of a dual layered oxide. Indeed, the oxide structure and chemistry is a direct product of the underlying microstructure, with a single homogeneous phase growing when the microstructure is deformation free, and two distinct phases growing when deformation is prevalent. The interfacial segregation characteristics are also affected due to the role of deformation in allowing for elements to move through the microstructure.

These conclusions on the role of deformation in surface oxidation were applied to two additional corrosion processes that occur in pressurized water nuclear reactors: SCC and CFC. In SCC, CW is instrumental in promoting crack growth in highly resistant materials. However, at levels up to 10% CW, it is insufficient to promote SCC without additional microchemical factors. These microchemical factors manifest themselves in different ways in different heats of material, but ultimately lead to Cr depletion and subsequent enhanced oxidation. Deformation is expected to play a role in enhancing the oxidation response of sensitized materials. Finally, in corrosion fatigue, the low level of underlying deformation was not linked to an increase corrosion response and subsequent retardation in crack growth. Instead, a slight reduction in enhancement of the CGR in the tested material appears to be a result of crack tip blunting, which was hypothesized to be a result of the underlying deformation.

7.2 Future directions

In performing this work a number of questions were opened that could not be adequately addressed due to the availability of equipment or material for further testing. Further work in

these areas would help to determine the explicit mechanisms occurring in the corrosion or cracking processes.

7.2.1 Surface oxidation

As discussed in Chapter 3, the level of Cu measured at the oxide/metal interface of electropolished specimens was surprising, and has not been previously addressed in the literature. Effort was placed on determining the source of the Cu, and from the experiments that were performed it is thought to originate from the material itself. However, additional experiments would help to validate that claim and refine the mechanisms of surface corrosion, particularly with respect to the outer oxide layer, and interfacial enrichment.

1) Measurement of the weight gain/weight loss after corrosion for specimens that are entirely one type of surface finish. For electropolished specimens weight loss would provide evidence of the presumed dissolution that results in Cu enrichment at the surface. If such dissolution was confirmed to occur, and was not accompanied by significant outer oxide particle precipitation, the mechanism of outer oxide growth could also be clarified.
2) Use of a chemical marker on the surface during oxidation. This would help to elucidate the location of the original surface with respect to the oxidation process and could provide evidence of solid state outward growth of the outer oxide layer. It could also provide evidence of increased dissolution as above. Additionally, a thin Cu coating could be applied to the surface and compared to the current results to determine if Cu at the surface migrates to the oxide/metal interface or prevents oxidation entirely.
3) Determination of the oxide characteristics on a specimen carefully hand polished to a mirror finish under conditions minimizing surface deformation during grinding. This would be expected to result in an oxide structure identical to the electropolished specimen, and would remove the possibility of Cu being an artifact of the electropolishing procedure.
4) Longer term oxidation experiments of electropolished specimens to identify the role of Cu in possibility limiting the oxidation rate, as has been discussed in the low temperature acid corrosion literature [144].

7.2.2 Stress corrosion cracking

Sensitization and second phases, water chemistry, and deformation were all implicated in the SCC response of the tested materials. However, their roles were all synergistic, and could not be adequately decoupled due to the parameters of the current tests. The following proposed experiments would help to decouple the effects of sensitization, second phases, water chemistry, and deformation.

1) SCC testing in a single environment (water chemistry and loading conditions). The SCC response of these materials was pronounced in phases 1 and 2, and depressed in phase 3. However, active crack tips could only be analyzed from phase 3, making it difficult to elucidate the processes occurring at the crack tip responsible for accelerated cracking in phases 1 and 2. Furthermore, the test phase or exposure time of plan-view specimens could not be conclusively determined. Generation of crack tips from each test phase in unique specimens would help to solve these problems. Additionally, it would help to clarify the mechanisms of cracking in phase 3 where it was unclear if IG cracking would have occurred at all had it not started in the more aggressive phase 2 environment. This may also shed light on the factors promoting low, but different levels of transgranular cracking in low CW, sensitized and unsensitized materials under different water chemistries.
2) Determine the role of specimen orientation (with respect to second phase particles and working direction) in the SCC response. In the current work sensitized delta ferrites were implicated in the cracking response of the material. However, it is unlikely such pronounced cracking response would have occurred if the delta ferrites were orientated perpendicular to the cracking direction. While similar work has been performed previously for CW direction it neglects to take into account the role that second phase particles and sensitization may play [53].
3) Determine if SCC suppression under sensitized conditions is possible through model alloy fabrication. 304L SS was hypothesized to be resistant to sensitization and SCC due to its low carbon content, yet different material factors (boron and delta ferrites) were sufficient to promote sensitization anyway. Model 304L SS alloys could be fabricated to be free of all factors that are currently known to promote sensitization (boron, delta ferrites, carbon) in order to determine if additional factors can still promote SCC.

7.2.3 Corrosion fatigue cracking

It was hypothesized that accelerated corrosion due to underlying deformation was responsible for the reduction in enhancement of corrosion fatigue CGR of the material tested. While accelerated corrosion was not found, a hydrogen-based mechanism interacting with the deformation was proposed, but no evidence was provided. Additional experimentation is necessary to clarify the factors promoting reduction in enhancement of CFC response.

1) Corrosion fatigue tests were run under a variety of rise time conditions, with crack tips only available for the last rise time. However, the plateauing of the CGR starts at rise times lower than the specimen analyzed here. Additional analysis of crack tips grown under different rise time conditions would provide validation that the decrease in crack growth enhancement is caused by increased blunting of the crack tip.
2) Comparison of corrosion fatigue crack response of materials with a wide variety of deformation levels would help to identify the explicit role of deformation in the reduction of CGR at long rise times. In the current work, only two specimens, with the same low level of deformation, were studied, making it difficult to conclusively identify the role of deformation in the observed crack growth response.
3) Recent work has shown the possibility of directly imaging the deformation structure ahead of corrosion fatigue crack tips by careful preparation of TEM specimens first by focused ion beam milling, and then by additional polishing using a NanoMill [105]. This type of analysis could provide indirect evidence of the role of residual deformation in the blunting of the crack tip.
4) Hydrogen has been hypothesized to play a role in the mechanisms of corrosion fatigue crack growth, yet is nearly impossible to image directly. This has been the motivation for imaging of the deformation structure for indirect evidence of the role of hydrogen [105]. Additional improvement of the cryogenic liftout technique discussed in Appendix 1, coupled with corrosion fatigue testing in deuterated water, is one possible way to provide direct evidence of the role of hydrogen in crack growth mechanisms.

APPENDICES

APPENDIX I:
Cryogenic liftout and detection of deuterium using APT

I.1 Background

Hydrogen is of interest in the field of environmentally assisted cracking (EAC) as it is generated during the corrosion processes, and has the potential to affect the cracking process, as discussed in detail in Chapter 7. Indeed, several leading theories on crack propagation mechanisms, such as the hydrogen enhanced localized plasticity (HELP) model [90, 158] rely on hydrogen. However, hydrogen is nearly impossible to measure accurately with all of the characterization techniques currently available to us. While H is theoretically possible to measure using atom probe tomography (APT), its quantification is difficult due to its appearance in all mass spectrums as H, H_2, and H_3, resulting from residual H in the high vacuum chamber of the instrument. Furthermore, it can also be observed after other major peaks such as FeH and FeOH and is especially prevalent during laser evaporation of oxides. However, the study of deuterium using APT has been successfully demonstrated for some materials [159-164]. Deuterium charging has been accomplished by directly charging the atom probe tip from either a liquid or gaseous deuterium phase. However, charging of a bulk specimen, followed by APT needle preparation has not yet been achieved. Previous work has provided evidence that the vacuum in the Cameca local electrode atom probe (LEAP) system does not draw out deuterium if it is sufficiently trapped even over long vacuum exposure times [162], eliminating this concern. The goal of this work was twofold: to evaluate the feasibility of doing cryogenic liftouts at the Michigan Center for Materials Characterization ($(MC)^2$), and to determine whether precharged deuterium could be detected in APT specimens fabricated by the liftout procedure. The successful detection of deuterium in the microstructure under controlled conditions could drive future testing of SCC or CFC in deuterated water, after which APT could be performed to identify the role of hydrogen in the cracking mechanism.

I.2 Experimental

For this work a sample of 304 SS cold worked to 25% reduction of thickness was used to induce a large number of trapping sites (dislocations) in the matrix [165, 166]. The specimen was charged in 573 K high temperature deuterium gas at 138 MPa for 124 days. After charge the specimen was package and shipped in dry ice, and then stored in a freezer below 255 K until testing.

Cryogenic liftout was performed on a Helios 650 Nanolab using a Leica cryostage maintained at 258 K during the liftout procedure. The specimen was transferred into the Helios using a Leica EM VCT100 transfer shuttle. After the liftout was performed the specimen was removed and stored in a cold environment. A standard 36 post Si array (by Cameca) was transferred to the cryostage using the transfer shuttle and the liftout specimen was deposited on several posts and sharpened. The array was then transferred into the Cameca LEAP 4000X HR using the transfer shuttle and transferred to the analysis chamber in a matter of approximately 2 minutes. The limiting factor in keeping the specimen cold was the use of a room temperature Omniprobe needle. The liftout specimen (approximate volume of 200 um^3) was attached to the needle and not under cooling for approximately 55 minutes.

I.3 Results

A successful cryogenic liftout was performed from the bulk, deuterium charged sample, with the entire sample remaining at 258 K throughout the procedure. However some complications were noted. First, the reduced temperatures of the stage caused immediate condensation of the Pt gas precursor covering the entire surface with a thick layer (Figure 38). To mitigate this issue larger working distance between the Pt needle and cold sample were used, as suggested in Ref. [167]. This reduced the condensation to a level where Pt could be used effectively for the liftout procedure. Additionally, the cold stage limits the rotational freedom of the stage, so the liftout procedure was modified to avoid the necessary 180° rotation typically employed.

The sharpened APT tips were transferred into the LEAP and successfully run in both voltage mode and laser mode to 15,000,000 collected ions. In addition, one tip from an

uncharged sample of the same highly cold worked material was fabricated and run under the same laser conditions at the same time, to provide a mass spectrum for comparison.

Several analysis methods were used in an attempt to identify deuterium in the bulk, none of which turned up any significant level of deuterium above background levels. Two portions of the mass spectrums obtained from laser pulsed experiments on the charged an uncharged specimens are shown in Figure 39 after being normalized to the tallest peak in the respective spectrum. In the first portion (left side of Figure 39) from 1 to 2 Dalton (Da) it can be seen that the charged specimen had a slightly taller peak at both 1 and 2 Da. However, in the case of deuterium being present, the ratio of the 2 Da peak to the 1 Da peak would be expected to be much larger. The calculated ratio H_2/H for the charged specimen is 0.139, while it is 0.143 for the uncharged specimen, providing an excellent indication that no real deuterium was detected in the charged specimen. However, it is possible that a majority of the deuterium could evaporate with a metal atom, such as NiD^{1+}. In this case, it would be expected that the mass to charge ratio of the Ni^{+1} isotopes at 58 and 60 Da would be skewed in favor of ^{60}Ni for the deuterium charged specimen. Ni^{+1} was chosen for primary analysis to avoid peak convolution of Cr^{+2} with Fe^{+2} and Fe^{+2} with Ni^{+2}, and it's suggested affinity for co-evaporation with H atoms [168]. It can be seen from the second portion of the mass spectrum (right side of Figure 39) that the isotopic ratios appear to be similar for the charged and uncharged specimens. Indeed, calculating the $^{60}Ni/^{58}Ni$ ratio yields 0.392 for the charged specimen and 0.391 for the uncharged specimen, which is close to the expected isotopic ratio of 0.385.

I.4 Discussion

While successful cryogenic liftout, sharpening, transfer and analysis was achieved using the system available at the $(MC)^2$ at the time, several modifications would improve the process and are currently under development.

The limiting factors in keeping the specimen cryogenic was during the actual liftout when it was attached to the room temperature Omniprobe needle for approximately 1 hour, and during transfer from the load chamber (room temperature) to the analysis chamber (cryogenically cooled) of the LEAP 4000X HR, which took approximately 2 minutes. The diffusion coefficient of deuterium (um^2/s) in austenitic stainless steel can be approximated by the equation

$$D_{Deuterium} = 4.7 \times 10^{-3} e^{\left(\frac{-12900}{RT}\right)} \quad (15)$$

which was empirically obtained for temperatures from 150 – 425 °C [169]. The diffusion distance (cm) is determined by the equation:

$$x = \sqrt{D_{Deuterium} t} \quad (16)$$

Assuming equation (15) holds for lower temperatures, the diffusion coefficient at 25 °C (room temperature) is 1.62×10^{-12} cm^2/s . For the liftout process a bar of approximate dimensions of 2 x 2 x 20 um was attached to the room temperature Omniprobe for 1 hour, corresponding to a diffusion distance of 0.76 um. For the chamber transfer, tips of diameter ~ 50 nm were at room temperature for 2 minutes, corresponding to a diffusion distance of 140 nm. From these calculations, it can be seen that most, if not all, of the deuterium could easily be outgassed from the specimen during the room temperature portions of the cryogenic liftout.

To mitigate this issue, a cryogenically cooled Omniprobe needle could be employed [170, 171], and is under development and testing at $(MC)^2$. Additional factors include the relatively high temperature of the stage compared to true cryogenic temperatures. Modifications to the cooling system recently undertaken at $(MC)^2$ now allow for stage temperatures closer to 133 K. Finally, while the Pt injection system was successfully used by modifying the sample height, water injection and condensation to ice is potentially a more practical method for future liftout procedures [172], but is only practical in conjunction with a cryogenically cooled Omniprobe needle.

Additionally, the hydrogen trapping would be expected to be largest in regions of high defect density. However, due to heavy oxidation of the specimen during charging, a specific region of the sample (such as grain boundary) could not be targeted for the liftout. The specimen was also fabricated from near the surface of the sample, where outgassing even at cold temperatures would have been most prevalent over the time period from retrieving the sample to performing the experiment (~10 months). However, removal of the surface oxide and penetration to deeper parts of the sample would require cutting or grinding procedures which would significantly raise the temperature of the sample. A possible cryogenic grinding or fracture may

be employed in the future. Unfortunately, the experiment failed to yield deuterium detection under the circumstances of this particular test. However, it is believed with a few modifications the procedure could be more successful, and may prove possible in the future.

Beyond the detection of deuterium by employing cryogenic specimen preparation, the technique has possible implications for broadening the application space of APT to biological or organic samples that could not be analyzed in the atom probe under typical conditions. Indeed the fabrication of such nanobiological samples is an area of interest in the field [173]. Cryogenic liftout and transfer, with the modifications mentioned previously, may prove one method to achieve this.

I.5 Conclusions

1. Cryogenic liftout using the equipment available was a success, with the limiting factor being the room temperature Omniprobe
2. No deuterium was detected in the sample, likely due to the time at room temperature, the inability to target a high density of trapping sites, or the relative proximity to the surface the samples were fabricated from.
3. Cryogenic liftout and transfer has implications towards increasing the application space of APT for biological applications.

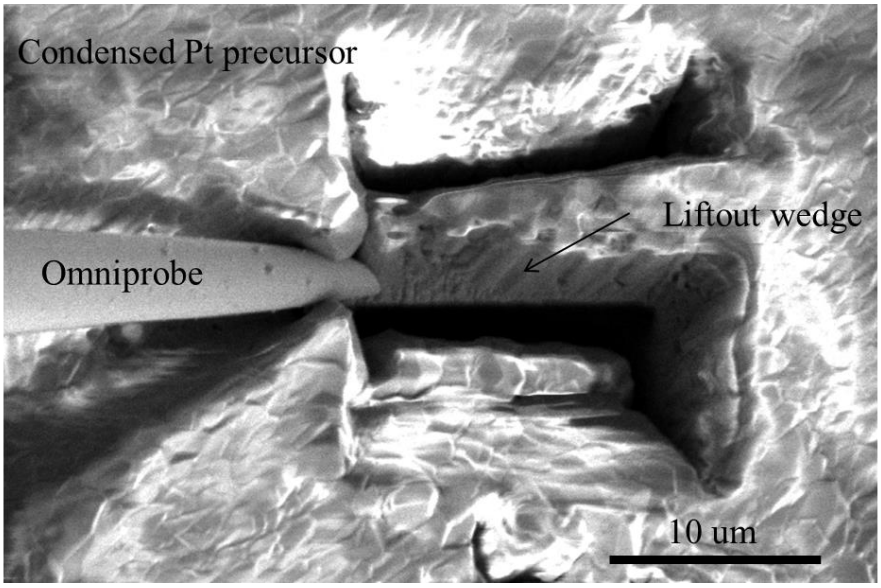

Figure 38: SEM image highlighting the difficulties of using Pt injection during cryogenic liftout procedures.

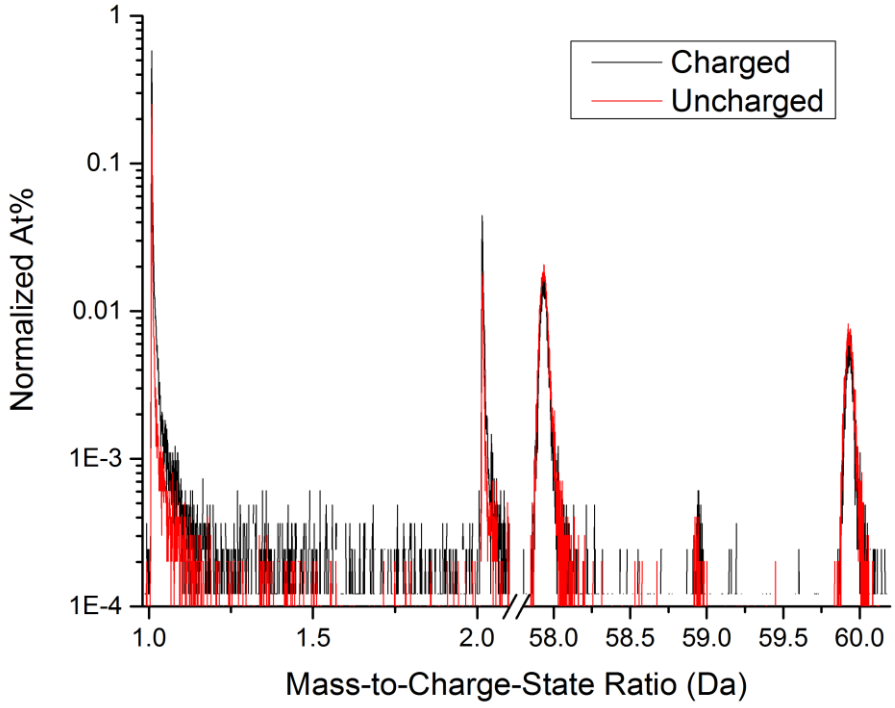

Figure 39: Portions of the APT mass spectrum obtained from bulk regions of deuterium charged and uncharged Type 304 SS with 25% CW. The deuterium peak at 2 Da is not taller for the charged specimen, nor is the Ni peak at 60 Da elevated compared to 58 Da, two indications that no deuterium was detected.

APPENDIX II:
Plasma-FIB APT specimen preparation[2]

II.1 Background

The site specific lift-out technique has become commonplace for the fabrication of atom probe tomography (APT) specimens from specific regions of interest such as interfaces and grain boundaries (GBs). This procedure typically utilizes a dual-beam scanning electron microscope (SEM) with a focused ion beam (FIB) of Ga^+ ions used for milling. While this procedure has been successfully used to prepare samples from a large variety of materials including metals, oxides, and ceramics, some materials are susceptible to significant Ga^+ ion implantation. Among these, aluminum is particularly susceptible to liquid metal embrittlement due to fast Ga diffusion and decoration of all grain boundaries and interfaces [174] . This phenomenon has been used to reveal the locations of grain boundaries in APT dataset prepared using Ga-FIB milling [175]. However it might also lead to erroneous chemical information. Recent advances in FIB technologies have resulted in the introduction of the plasma-FIB (P-FIB), which utilizes Xe^+ as the ion source. Typically touted for their higher milling speed compared to Ga^+ ions due to their increased mass, Xe^+ ions may also have the advantage of reduced implantation. However, due to their larger size, they also cause a decrease in resolution of the FIB imaging. The purpose of this project was twofold: to evaluate the feasibility of preparing atom probe specimens using a P-FIB, and to evaluate the role of Ga in changing the microchemical properties of the GB.

II.2 Experimental

In this study, a P-FIB was used to test the feasibility of preparing atom probe specimens that would otherwise be susceptible to Ga^+ implantation. Al-2Cu was chosen as one of the test materials based on the known issue of Ga^+ implantation in Al alloys. The sample was solution-treated at 540 °C for 4 hours and rapidly quenched in ice water, and then aged at 250 °C for 4 hours before being polished. GBs were easily identifiable by the channeling contrast of the secondary electrons in the SEM. One grain boundary (GB) was chosen for analysis, and two lift-outs were performed; the first on an FEI Helios P-FIB Dual Beam at Carnegie Mellon University, and the second on an FEI Helios 650 NanoLab Dual Beam using Ga^+ at the

[2] The content of this appendix is adapted from the following article which has been published:
Fisher, K. B. and Marquis, E. A., Comparing Plasma-FIB and Ga-FIB Preparation of Atom Probe Tomography Samples, Proceedings of Microscopy and Microanalysis, 2016, pp.692-693.

University of Michigan. The final atom probe specimens from each lift-out were prepared by a series of annular milling steps on the respective instrument. Specimens were field evaporated in a Cameca LEAP 4000X HR using voltage mode with 18% pulse fraction, 40 K base temperature, 200 kHz pulse rate, and a target detection rate of 2 ions/1000 pulses. Volumetric reconstructions and subsequent analyses were performed in IVAS 3.6.6 by Cameca using crystallographic information preserved in the detection histogram, as discussed in [115]. Additional simulations of ion implantation depth at conditions similar to those used for FIB sample preparation were conducted using the Stopping Range of Ions in Matter (SRIM) tool [176].

II.3 Results

Simulations using SRIM [176] were conducted for Ga and Xe ions incident on an Al substrate at 30 kV (liftout and annular milling conditions) and 5 kV (final low kV clean of APT specimen), and the results are shown in Figure 40. At 30 kV Xe implantation peaks at about 25 nm and stops at 40 nm, while Ga peaks at 25 nm and stops at 50 nm. The difference in implantation depth at 5 kV is negligible.

However, differences were observed in the actual specimens after reconstruction. Figure 41 shows a reconstruction of a specimen prepared using the P-FIB, along with a 1-dimensional concentration profile across the GB and the mass spectrum with peaks identified. Very slight Xe^{+3} peaks were observed in the mass spectrum, and are concentrated at the specimen apex in the reconstruction. Figure 42 shows the same sequence of images for the Ga^{+} prepared sample, which contained both a GB and a Cu rich precipitate. In this specimen Ga^{+} is clearly observed at the GB, as indicated in the concentration profile, and additionally at the matrix/precipitate interface, as seen in the Ga^{+} map. Despite Ga^{+} concentration at the GB the measured profiles for the Al and Cu species at the GB were very similar for both specimens after subtracting out the FIB ion.

II.4 Discussion

P-FIB fabrication of APT specimens was not only successful in terms of fabricating tips and capturing features of interest despite the slightly poorer resolution compared to a Ga^{+}-FIB, it mitigated the issue of Ga implantation in Al, one of the most susceptible materials. However, it was found that the presence of Ga in the GB did not significantly alter the measured GB

chemistry compared to the sample prepared using P-FIB. This analysis was complicated slightly by the presence of the GB precipitate in the Ga-FIB prepared specimen, which may have altered the nearby GB chemistry.

The successful use of P-FIB to prepare APT specimens, however, has the potential to increase the application space of the technique. Semiconductors are currently an area of intense research interest, and due to the ever decreasing sizes of interest for commercial application, APT is a logical means by which to study the role of chemistry in multilayered semiconductor structures. However, Ga-FIB preparation of APT specimens has caused complications in this industry, as Ga is often one of the elements of interest [177]. By employing a P-FIB, any doubt about the measured Ga concentration due to FIB induced Ga damage could be eliminated.

II.5 Conclusions

1. Successful APT specimen preparation, including the targeting of features such as GB, can be achieved with the P-FIB.
2. The calculated implantation of Ga and Xe during the low kV clean step employed during APT specimen fabrication is similar, suggesting little difference should be observed in the specimen
3. Due to the liquid metal embrittlement reaction of Al with Ga, significant Ga^+ is observed decorating interfaces. No similar reaction occurs with Xe, and very little Xe^+ was observed in the mass spectrum for the P-FIB prepared sample.
4. After subtracting out the Ga^+ at the GB the measured composition profiles at the GB between the Ga^+-FIB and P-FIB specimens are very similar. This suggests Ga^+-FIB can still be employed despite implantation.
5. The use of P-FIB has implications in increasing the application space of the technique towards use in sensitive and/or Ga containing materials.

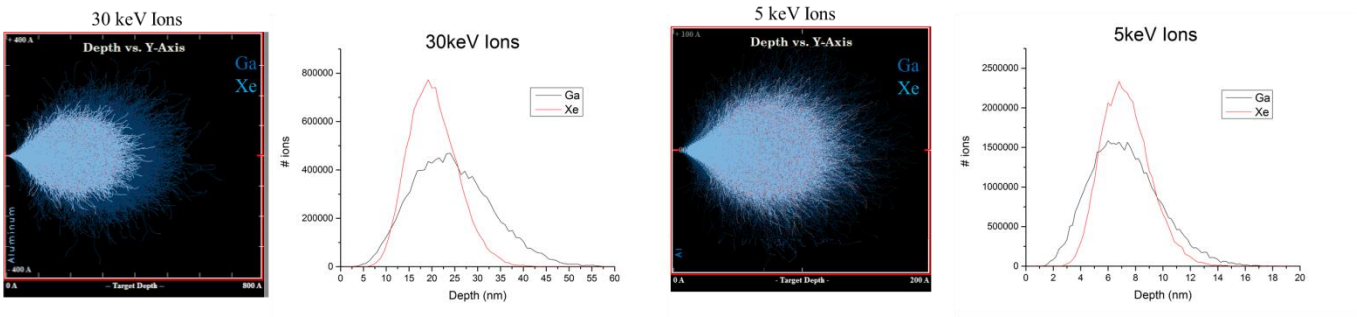

Figure 40: Simulations using SRIM [176] of Ga and Xe ions implanting in Al under conditions comparable to those used in the FIB.

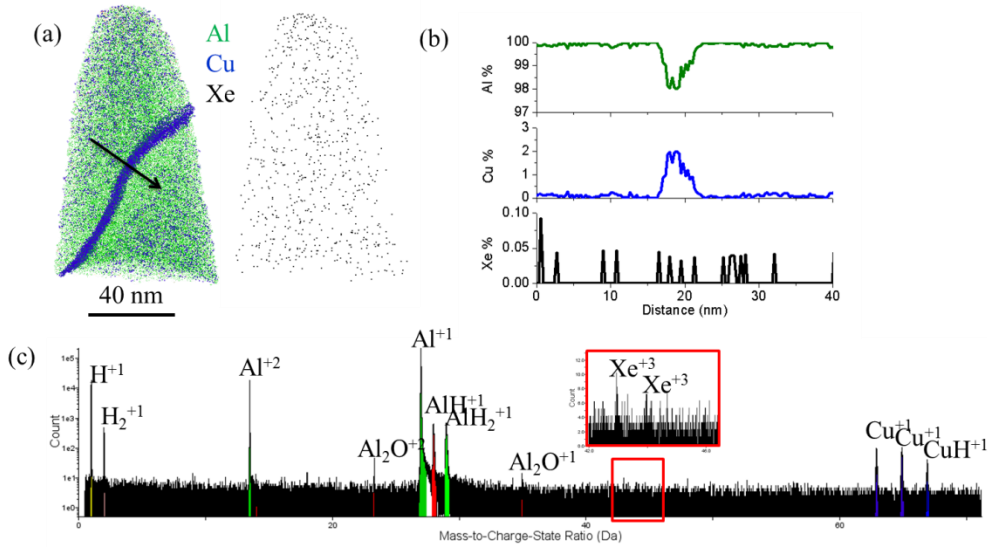

Figure 41: Al specimen containing a GB fabricated using the P-FIB. (a) Reconstruction, (b) 1-dimensional concentration profile across the GB, (c) Mass spectrum showing only very small Xe^{+3} peaks.

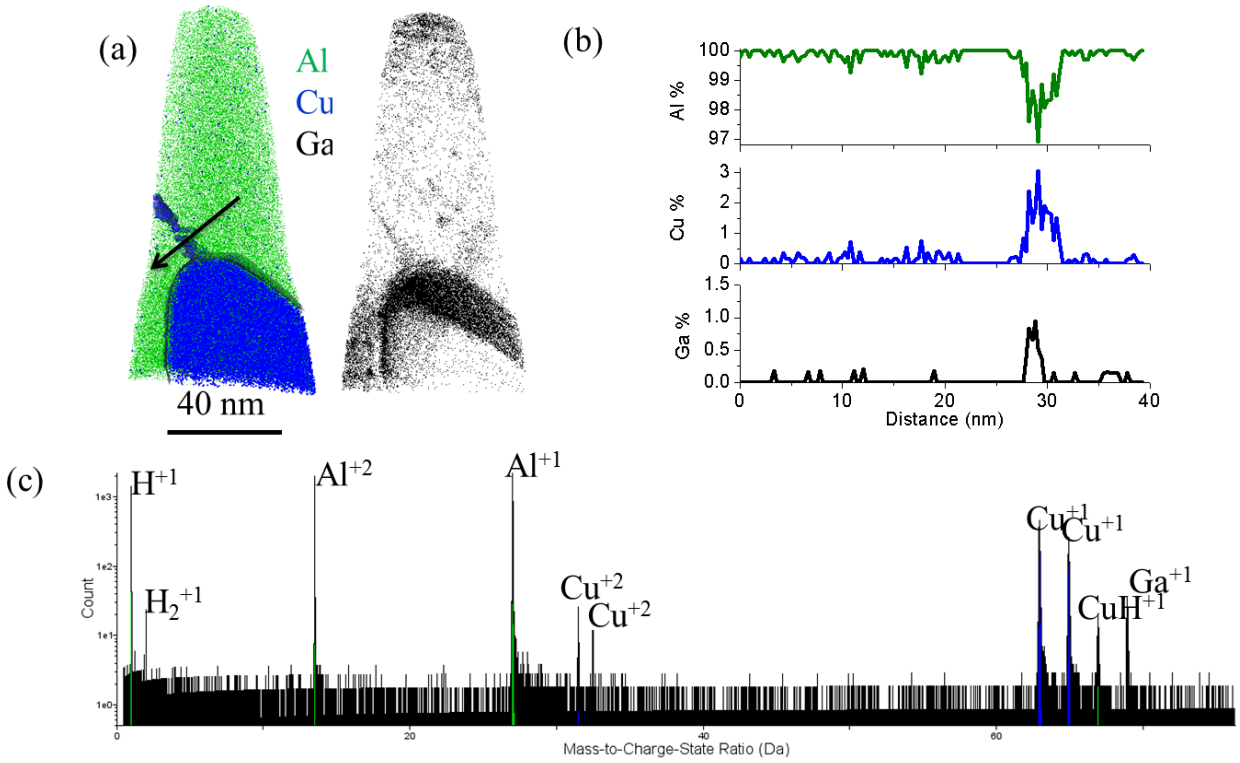

Figure 42: Al specimen containing a GB fabricated using the Ga-FIB. (a) Reconstruction, (b) 1-dimensional concentration profile across the GB showing Ga segregation, (c) Mass spectrum showing only a significant Ga^{+} peak.

APPENDIX III:
Oxidation of 304L SS in an air environment

III.1 Background

The oxidation of 304 SS in air differs from oxidation in water in that solution effects, such as precipitation of ions from solution, cannot occur. Thus the mechanisms of growth are always solid state processes. A thermodynamically controlled process is expected to result in a protective Cr_2O_3 layer. However, at higher temperatures the oxidation process is kinetically controlled and favors the fastest forming oxide rather than the thermodynamically stable one [141, 178].

At intermediate temperatures (200-350 °C) a duplex oxide film has been reported with an Fe-rich outer layer and a Cr-rich inner layer [141]. The outer layer has been reported to be FeO [178] or Fe_2O_3 [141], and the inner layer has been identified as a mixed Fe/Cr spinel [141]. Above ~ 600 °C the Cr content in the inner layer increases with increasing temperature up to ~900 °C, where a stable Cr_2O_3 film can form [178]. A variety of factors, including the oxygen partial pressure of the environment can certainly play a role in the resulting oxide [179], and was not carefully controlled in this experiment. Instead of a full characterization of the oxidation of 304 SS in air, these experiments were instead undertaken to provide direct comparisons of the oxide species measurements to those in water, validate the identification of different phases using atom probe tomography (APT), and in an attempt to further clarify the origin of Cu at the oxide/metal interface.

III.2 Experimental

The material used for this study was the same as heat E in Chapter 5, with composition shown in Table 9. The material surfaces were prepared the same as those studied in short term oxidation studies in Chapter 4, namely one side was ground with 300 grit sand paper, and the other side was electropolished. Two sets of oxidations were performed in laboratory air. The first was at the same temperature as short term aqueous exposures of chapter 4 – 288 °C for 72 hours. A very thin oxide formed on the electropolished side that was not easily characterized by APT. The ground side exhibited slightly more extensive oxidation that could be characterized. An additional exposure was conducted at 650 °C for 72 hours. This resulted in a much thicker

oxide layer that was characterized from the electropolished surface. The instruments and characterization procedures used in this work were the same as those reported in Chapter 4 for short term oxidation specimens.

III.3 Results

SEM images of the oxidized surfaces for both exposures are shown in Figure 43. For the 288 °C oxidation, the underlying grain structure clearly had an effect on the oxide growth, and enhanced oxidation occurred at the grain boundaries. However, the oxide proved too thin to capture meaningful data using APT. The ground surface had a thicker oxide layer and an APT reconstruction is shown Figure 44 along with a 1-dimensional concentration profile perpendicular to the oxide/metal interface. A dual layer oxide was observed. The outer oxide was rich in Fe and had some Ni and Cr. The inner oxide layer was rich in Cr and had very little Ni and a small Fe component. Both compositions are shown in Table 16. Ni rich fingers were observed discontinuously at the interface, while little to no Cu was observed.

A reconstruction of the specimen captured from the electropolished side after oxidation at 650 °C is shown in Figure 45 along with a 1-dimensional concentration profile across the oxide/metal interface. Only a small depth of the oxide near the oxide metal interface was captured because the overall oxide thickness (~450 nm) was much larger than what can reasonably captured in a single atom probe specimen. The oxide had significant Fe and Cr contributions, and the matrix adjacent was rich in Ni and deficient in Cr and Fe compared to the original matrix. No Cu was observed at the oxide metal interface of this specimen. The oxide composition is also shown in Table 16.

III.4 Discussion

In a kinetically grown oxide the diffusion rates in the metal and the oxide determine the oxide phases. The diffusion rates in the matrix at 275 °C were already reported in Chapter 4, and diffusion rates at 650 °C are reported in Table 17. The diffusion rate of metal cations in the oxide lattice is reported to substantially increase at temperatures above 600 °C [180], although the explicit diffusion coefficients in various Fe and Cr oxide structures could not be found. For a spinel structure the same diffusion rate shown in equation (7) in Chapter 4, but may be different for M_2O_3 or MO structures.

III.4.1 288 °C oxidation

Based on APT chemistry measurements the dual layer oxide observed after air oxidation was different than that observed after aqueous oxidation. The outer layer was an Fe-rich layer identified as wustite (FeO) based on the measured M:O ratio compared to pure phases in the Chapter 3 pure oxide studies. While not the most thermodynamically stable oxide at these temperatures (which would be Cr_2O_3), it has been shown to have the highest formation rate of Fe oxide species [178].

At similar temperatures some authors have reported an Cr-rich inner oxide [141], while others have noted only depletion of Fe in the underlying matrix [178]. It is possible that this discrepancy is a direct result of the resolution of the chemical analysis technique used. The current results clearly support the presence of a Cr-rich inner oxide layer. This phase is similar in measured stoichiometry to the Cr-rich oxide regions of deformed surfaces in Chapter 4, and it is unclear if it is a spinel or a chromia type layer based on the measured stoichiometry. Previously this layer has been identified as a spinel [141], which is consistent with the increased Fe and Ni in the outer oxide layer based on the diffusion rates of the metal species through a spinel structure. Discontinuous Ni-rich fingers are observed beneath the oxide/metal interface with both Fe and Cr depleted in this region, similar to what was observed on deformed surfaces in Chapter 4. They may result from rejection of Ni from the Cr-rich oxide layer or from selective oxidation of Cr due to the increased diffusion along deformed regions, as discussed previously. Very little Cu was observed at the interface.

These features are consistent with a dual layer structure in which the inner oxide grows by inward growth governed by oxygen diffusion to the oxide/metal interface and the outer oxide grows by outward growth by the diffusion of the faster diffusion species (Fe and Ni) through the inner oxide layer to react with oxygen at the surface. The mechanism is similar to what is observed during aqueous oxidation at the same temperature, except for the fact that outer oxide growth must occur by a solid state reaction due to the absence of solution effects. However the product is somewhat different due to environment (gaseous) and how it dictates oxide stability.

III.4.2 650 °C oxidation

The oxide film obtained after higher temperature air oxidation is much different in appearance than that obtained at lower temperatures. The oxide is much thicker, but based on cross sectional imaging it was unclear if the oxide was dual layered in nature. Some voids were

observed at the oxide/metal interface, but were avoided for APT analysis. The oxide surface is nodular, with the original specimen surface completely obscured.

The measured oxide composition is rich in Cr and has some Fe, closely matching that expected for $FeCr_2O_4$ besides the known oxygen deficiency. Previous results have shown that at temperatures near 700 °C Cr is started to be incorporated into the Fe-rich oxide formed at lower temperatures, with Cr content increasing with temperature and that at temperatures higher than 900 °C a Cr_2O_3 film forms [178]. However the precise phase expected at intermediate temperatures is unclear from the literature, and no additional work was performed to verify the phase observed here.

The increase in Cr in the oxide is due to the greater thermodynamic stability of the chromia film, coupled with the increased diffusion kinetics of Cr in the oxide [180]. The matrix adjacent to the oxide is devoid of Cr, consistent with the fact that Cr diffusion in the matrix is faster than that of Fe and Ni at these temperatures, and that there is a thermodynamic and kinetic driving force for Cr outward diffusion. Thus the oxide at higher temperatures likely grows by a dominant mechanism of outward growth by Cr cation diffusion.

While this oxide was grown on the electropolished surface that exhibited enhanced Cu when oxidized in water, the different mechanism of growth (outward versus inward) means the mechanism of potential Cu rejection to the interface may not be relevant. Indeed, no Cu was observed at the oxide/metal interface.

III.5 Results

1. Comparisons between the oxide films formed in air and under aqueous conditions suggest phase identification of oxides obtained by APT from non-pure specimens is still feasible, but should be accompanied by additional characterization methods such as TEM or Raman spectroscopy.
2. The oxides observed after air oxidation exhibit features consistent with the literature on the topic, and different than those observed after oxidation in aqueous conditions. For instance, depletion of the underlying matrix is obvious after high temperature air oxidation, consistent with an outward growth mechanism.
3. No definitive conclusions on the source of Cu could be made. This is because analysis of the oxide formed on electropolished surfaces at low temperatures was unsuccessful due to

the very thin layer, and at high temperatures the oxide growth mechanism is substantially different precluding the role of Cu during growth.

Table 16: APT measured oxide compositions (At%)

Specimen	Layer	Fe	Cr	Ni	O
Ground 288°C	Outer	46.2	8.1	8.0	36.0
	Inner	6.2	40.0	2.2	49.1
Electropolished 650°C	Inner	14.7	30.5	3.4	50.1

Table 17: Volume and GB diffusion coefficients for species of Fe-Cr-Ni alloys at 650 °C

	$D_{gb}(cm^2/s)$*	$D_v(cm^2/s)$
Fe	7.5E-10[147]	7.5E-17 [147]
Cr	1.6E-9 [147]	1.8E-16 [147]
Ni	3.9E-13[149]	4.7E-17 [149]

*GB width assumed to be 5E-8cm

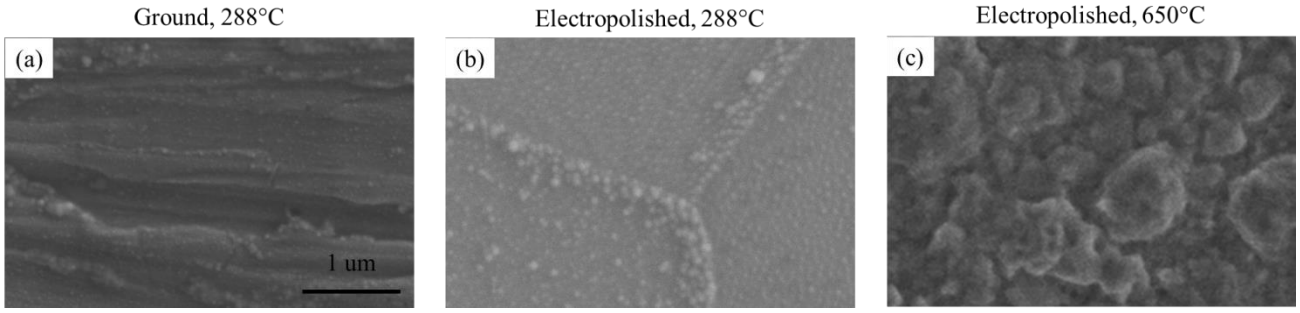

Figure 43: SEM images of the oxide films after air oxidation.

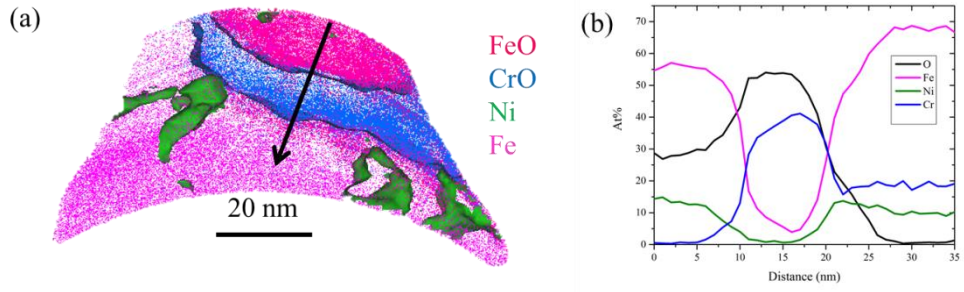

Figure 44: (a) 10 nm slice of a reconstruction obtained from the ground specimen oxidized in air for 72 hours at 288 °C with 20% CrO isosurface (blue) and 20% Ni isosurface

(green) highlighting the different regions. (b) 1-dimensional concentration profile down the arrow shown in (a).

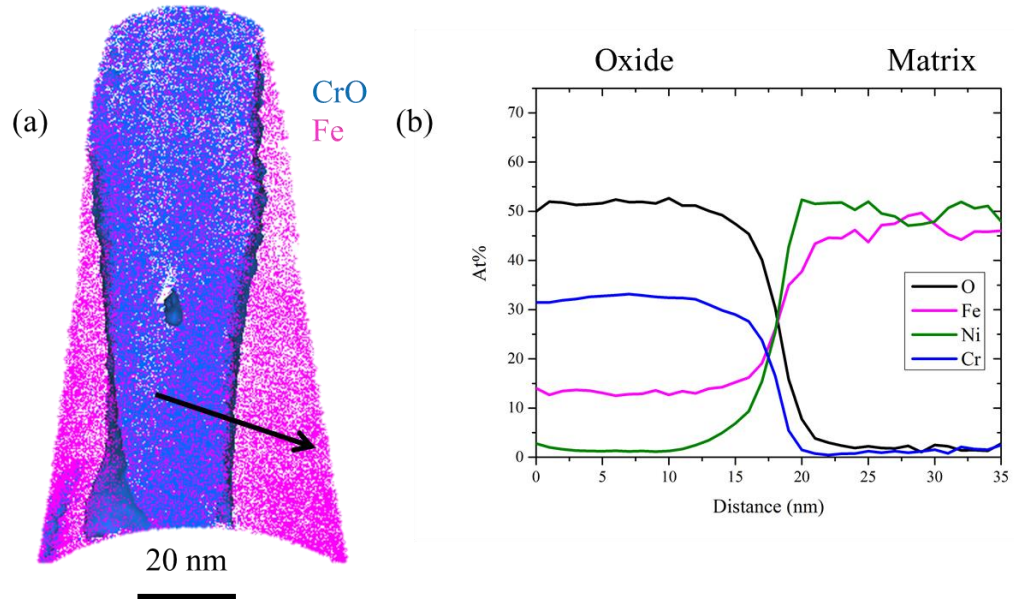

Figure 45: (a) 10 nm slice of a reconstruction obtained from the electropolished specimen oxidized in air for 72 hours at 650 °C with 15% CrO isosurface (blue). (b) 1-dimensional concentration profile down the arrow shown in (a).

REFERENCES

[1] "North American Stainless", http://www.northamericanstainless.com/, 2010.

[2] Hicks, J.H. "Nuclear Reactors, Water Chemistry of Lightwater Reactors", *Kirk-Othmer Encyclopedia of Chemical Technology,* 2000, pp. 1-12.

[3] Kuang, W., Han, E.-H., Wu, X., and Rao, J. "Microstructural characteristics of the oxide scale formed on 304 stainless steel in oxygenated high temperature water", *Corrosion Science,* Vol. 52, Iss. 11, 2010, pp. 3654-3660.

[4] Ljungberg, L.G., Cubicciotti, D., and Trolle, M. "Materials Behavior in Alternate (Hydrogen) Water Chemistry in the Ringhals-1 Boiling Water Reactor", *CORROSION,* Vol. 42, Iss. 5, 1986, pp. 263-271.

[5] Andresen, P.L. "Effects of Transients in Water Chemistry, Temperature, and Loading on Intergranular Stress Corrosion Cracking of AISI 304 Stainless Steel", *Corrosion (Houston, Tex.),* Vol. 42, Iss. 3, 1986, pp. 169-180.

[6] Andresen, P.L. "Effects of Impurities and Supporting Electrolytes On SCC of 304 Stainless Steel in High Temperature Aqueous Environments", *Corrosion (Houston, Tex.),* Vol. 38, Iss. 10, 1982, pp. 531-541.

[7] Ruther, W.E., Soppet, W.K., and Kassner, T.F. "Effect of Temperature and Ionic Impurities at Very Low Concentrations on Stress Corrosion Cracking of AISI 304 Stainless Steel", *Corrosion,* Vol. 44, Iss. 11, 1988, pp. 791-799.

[8] Kim, Y.-J. "Characterization of the oxide film formed on type 316 stainless steel in 288 C water in cyclic normal and hydrogen water chemistries", *Corrosion,* Vol. 51, Iss. 11, 1995, pp. 849-860.

[9] Maekawa, T., Kagawa, M., and Nakajima, N. "Corrosion Behaviors of Stainless Steel in High-Temperature Water and Superheated Steam", *Transactions of the Japan Institute of Metals*, Vol. 9, Iss. 2, 1968, pp. 130-136.

[10] Kim, Y.J. "In-situ electrochemical impedance measurement of oxide film formed on type 304 stainless steel in high-temperature water", *Corrosion,* Vol. 56, Iss. 4, 2000, pp. 389-394.

[11] Kuang, W., Wu, X., and Han, E.-H. "The oxidation behaviour of 304 stainless steel in oxygenated high temperature water", *Corrosion Science*, Vol. 52, Iss. 12, 2010, pp. 4081-4087.

[12] Kuang, W., Wu, X., and Han, E.-H. "Influence of dissolved oxygen concentration on the oxide film formed on 304 stainless steel in high temperature water", *Corrosion Science*, Vol. 63, Iss. 2012, pp. 259-266.

[13] Wada, Y., Watanabe, A., Tachibana, M., Ishida, K., Uetake, N., Uchida, S., Akamine, K., Sambongi, M., Suzuki, S., and Ishigure, K. "Effects Of Hydrogen Peroxide On Intergranular Stress Corrosion Cracking Of Stainless Steel in High Temperature Water, (IV)", *Journal of Nuclear Science and Technology,* Vol. 38, Iss. 3, 2001, pp. 183-192.

[14] Ming, H.L., Zhang, Z.M., Wang, S.Y., Wang, J.Q., Han, E.H., and Ke, W. "Short time oxidation behavior of 308L weld metal and 316L stainless steel with different surface

state in simulated primary water with 0.1 mg/L dissolved oxygen", *Materials and Corrosion,* Vol. 66, Iss. 9, 2015, pp. 869-881.

[15] Sun, H., Wu, X., Han, E.-H., and Wei, Y. "Effects of pH and dissolved oxygen on electrochemical behavior and oxide films of 304SS in borated and lithiated high temperature water", *Corrosion Science,* Vol. 59, Iss. 2012, pp. 334-342.

[16] Kuang, W., Wu, X., Han, E.-H., and Rao, J. "Effect of alternately changing the dissolved Ni ion concentration on the oxidation of 304 stainless steel in oxygenated high temperature water", *Corrosion Science,* Vol. 53, Iss. 8, 2011, pp. 2582-2591.

[17] Ziemniak, S.E. and Hanson, M. "Corrosion behavior of 304 stainless steel in high temperature, hydrogenated water", *Corrosion Science,* Vol. 44, Iss. 10, 2002, pp. 2209-2230.

[18] Ziemniak, S.E., Hanson, M., and Sander, P.C. "Electropolishing effects on corrosion behavior of 304 stainless steel in high temperature, hydrogenated water", *Corrosion Science,* Vol. 50, Iss. 9, 2008, pp. 2465-2477.

[19] da Cunha Belo, M., Walls, M., Hakiki, N.E., Corset, J., Picquenard, E., Sagon, G., and Noël, D. "Composition, structure and properties of the oxide films formed on the stainless steel 316L in a primary type PWR environment", *Corrosion Science,* Vol. 40, Iss. 2–3, 1998, pp. 447-463.

[20] Lister, D.H., Davidson, R.D., and McAlpine, E. "The mechanism and kinetics of corrosion product release from stainless steel in lithiated high temperature water", *Corrosion Science,* Vol. 27, Iss. 2, 1987, pp. 113-140.

[21] Morrison, J., Johnson, N., Hutchinson, T., Caswell, T., Connolly, B., and Banks, A. "Effect of surface finish on the corrosion behaviour of grade 316L stainless steels in pressurized, high temperature, lithiated water", 17th International Conference on Environmental Degradation of Materials in Nuclear Power Systems – Water Reactors Ottawa, Ontario, Canada, 2015.

[22] Terachi, T., Yamada, T., Miyamoto, T., Arioka, K., and Fukuya, K. "Corrosion Behavior of Stainless Steels in Simulated PWR Primary Water—Effect of Chromium Content in Alloys and Dissolved Hydrogen—", *Journal of Nuclear Science and Technology,* Vol. 45, Iss. 10, 2008, pp. 975-984.

[23] Bauch, R., Cambini, M., Weisgerber, P., DeAsmundis, C., and Plog, C. "Investigations on oxide formed in high-temperature water on austenitic steel", *Journal of Nuclear Materials,* Vol. 92, Iss. 2–3, 1980, pp. 334-344.

[24] Xu, J., Wu, X.Q., and Han, E.H. "The evolution of electrochemical behaviour and oxide film properties of 304 stainless steel in high temperature aqueous environment", *Electrochimica acta,* Vol. 71, Iss. 2012, pp. 219-226.

[25] Kruska, K., Saxey, D.W., Terachi, T., Yamada, T., Chou, P., Calonne, O., Fournier, L., Smith, G.D., and Lozano-Perez, S. "Atom-probe tomography of surface oxides and oxidized grain boundaries in alloys from nuclear reactors", MRS Online Proceedings Library, 2013.

[26] Massoud, T., Maurice, V., Klein, L.H., Seyeux, A., and Marcus, P. "Nanostructure and local properties of oxide layers grown on stainless steel in simulated pressurized water reactor environment", *Corrosion Science,* Vol. 84, Iss. 1, 2014, pp. 198-203.

[27] Szklarska-Smialowska, Z., Chou, K.-c., and Xia, Z. "The composition and properties of oxide films on type 304 stainless steel on exposure to lithiated water at 100–350°C", *Corrosion Science,* Vol. 32, Iss. 5–6, 1991, pp. 609-619.

[28] Tapping, R.L., Davidson, R.D., McAlpine, E., and Lister, D.H. "The composition and morphology of oxide films formed on type 304 stainless steel in lithiated high temperature water", *Corrosion Science,* Vol. 26, Iss. 8, 1986, pp. 563-576.
[29] Robertson, J. "The mechanism of high temperature aqueous corrosion of stainless steels", *Corrosion Science,* Vol. 32, Iss. 4, 1991, pp. 443-465.
[30] Ziemniak, S.E. and Castelli, R.A. "Immiscibility in the Fe3O4–FeCr2O4 spinel binary", *Journal of Physics and Chemistry of Solids,* Vol. 64, Iss. 11, 2003, pp. 2081-2091.
[31] Winkler, R. "Studies on anticorrosion layers on steels typical for power stations", *Kernenergie,* Vol. 32, Iss. 5, 1989, pp. 188-193.
[32] Stellwag, B. "The mechanism of oxide film formation on austenitic stainless steels in high temperature water", *Corrosion Science,* Vol. 40, Iss. 2–3, 1998, pp. 337-370.
[33] Douglas, L. and Zyzes, F.C. "The Corrosion of Iron in High-Temperature Water (Part 1—Corrosion Rate Measurements)", *Corrosion,* Vol. 13, Iss. 6, 1957, pp. 19-32.
[34] Lozano-Perez, S., Saxey, D.W., Yamada, T., and Terachi, T. "Atom-probe tomography characterization of the oxidation of stainless steel", *Scripta Materialia,* Vol. 62, Iss. 11, 2010, pp. 855-858.
[35] Lozano-Perez, S., Saxey, D., Marquis, E., Terachi, T., and Yamada, T. "Atom-probe Tomography of Surface Oxides in a 20% Cold Worked Stainless Steel Tested Under PWR Primary Water Conditions", *Microscopy and Microanalysis,* Vol. 15, Iss. Supplement 2, 2009, pp. 304-305.
[36] Lozano-Perez, S. "Novel characterization of stress corrosion cracks", Electron Microscopy and Analysis Group Conference, 2007.
[37] Lozano-Perez, S., Rodrigo, P., and Gontard, L.C. "Three-dimensional characterization of stress corrosion cracks", *Journal of Nuclear Materials,* Vol. 408, Iss. 3, 2011, pp. 289-295.
[38] Terachi, T., Fujii, K., and Arioka, K. "Microstructural characterization of SCC crack tip and oxide film for SUS 316 stainless steel in simulated PWR primary water at 320°C", *Journal of Nuclear Science and Technology,* Vol. 42, Iss. 2, 2005, pp. 225-232.
[39] Arioka, K., Yamada, T., Terachi, T., and Chiba, G. "Cold work and temperature dependence of stress corrosion crack growth of austenitic stainless steels in hydrogenated and oxygenated high-temperature water", *Corrosion,* Vol. 63, Iss. 12, 2007, pp. 1114-1123.
[40] Agency, I.A.E. "Stress Corrosion Cracking in Light Water Reactors: Good Practices and Lessons Learned", *Vienna, Austria,* 2011.
[41] Kim, Y.-J. "Evaluation of Alternate Reductants for Application in Light Water Reactors", *Corrosion,* Vol. 62, Iss. 9, 2006, pp. 795-800.
[42] Indig, M.E. and McIlree, A.R. "High Temperature Electrochemical Studies of the Stress Corrosion of Type 304 Stainless Steel", *Corrosion,* Vol. 35, Iss. 7, 1979, pp. 288-295.
[43] Szklarksa-Smialowska, S. and Cragnolino, G. "Stress Corrosion Cracking of Sensitized Type 304 Stainless Steel in Oxygenated Pure Water at Elevated Temperatures (Review)", *Corrosion,* Vol. 36, Iss. 12, 1980, pp. 653-665.
[44] Andresen, P. "Effects of temperature on crack growth rate in sensitized type 304 stainless steel and alloy 600", *Corrosion,* Vol. 49, Iss. 9, 1993, pp. 714-725.
[45] Meisnar, M., Vilalta-Clemente, A., Moody, M., Arioka, K., and Lozano-Perez, S. "A mechanistic study of the temperature dependence of the stress corrosion crack growth

rate in SUS316 stainless steels exposed to PWR primary water", *Acta Materialia,* Vol. 114, Iss. 1, 2016, pp. 15-24.
[46] Arioka, K., Yamada, T., Terachi, T., and Miyamoto, T. "Dependence of Stress Corrosion Cracking for Cold-Worked Stainless Steel on Temperature and Potential, and Role of Diffusion of Vacancies at Crack Tips", *Corrosion,* Vol. 64, Iss. 9, 2008, pp. 691-706.
[47] Terachi, T., Yamada, T., Miyamoto, T., and Arioka, K. "SCC growth behaviors of austenitic stainless steels in simulated PWR primary water", *Journal of Nuclear Materials,* Vol. 426, Iss. 1–3, 2012, pp. 59-70.
[48] Congleton, J., Berrisford, R.A., and Yang, W. "Stress Corrosion Cracking of Sensitized Type 304 Stainless Steel in Doped High-Temperature Water", *Corrosion,* Vol. 51, Iss. 12, 1995, pp. 901-910.
[49] Sedriks, A.J. "Corrosion of Stainless Steels", 1996.
[50] Bain, E., Aborn, R., and Rutherford, J. "The nature and prevention of intergranular corrosion in austenitic stainless steels", *Transactions of the American Soceity for Steel Treating,* Vol. 21, Iss. 1, 1933, pp. 481-509.
[51] Bruemmer, S.M., Arey, B.W., and Charlot, L.A. "Influence of chromium depletion on intergranular stress corrosion cracking of 304 stainless steel", *Corrosion,* Vol. 48, Iss. 1, 1992, pp. 42-49.
[52] Berry, W.E., White, E.L., and Boyd, W.K. "Stress corrosion cracking of sensitized stainless steel in oxygenated high temperature water", *Corrosion,* Vol. 29, Iss. 12, 1973, pp. 451-469.
[53] Arioka, K., Yamada, T., Terachi, T., and Chiba, G. "Influence of carbide precipitation and rolling direction on intergranular stress corrosion cracking of austenitic stainless steels in hydrogenated high-temperature water", *Corrosion,* Vol. 62, Iss. 7, 2006, pp. 568-575.
[54] Arioka, K., Yamada, T., Terachi, T., and Staehle, R. "Intergranular stress corrosion cracking behavior of austenitic stainless steels in hydrogenated high-temperature water", *Corrosion,* Vol. 62, Iss. 1, 2006, pp. 74-83.
[55] ASTM, *Standard practices for detecting susceptibility to intergranular attack in austenitic stainless steels,* in *A262*, 2014, pp. 1-20.
[56] Majidi, A.P. and Streicher, M.A. "The Double Loop Reactivation Method for Detecting Sensitization in AISI 304 Stainless Steels", *Corrosion,* Vol. 40, Iss. 11, 1984, pp. 584-593.
[57] Miller, B.D. and Burke, M.G. "Characterization of type 304L stainless steel: comparison of ASTM A262 Practice A and analytical electron microscopy techniques", 15th International Conference on Environmental Degradation of Materials in Nuclear Power Systems-Water Reactors, 2012.
[58] Horn, R.M., Gordon, G.M., Ford, F.P., and Cowan, R.L. "Experience and assessment of stress corrosion cracking in L-grade stainless steel BWR internals", *Nuclear Engineering and Design,* Vol. 174, Iss. 3, 1997, pp. 313-325.
[59] Otterberg, R. and Roberts, W. "Intergranular Precipitation in Type 304 L Austenitic Stainless Steels Containing Small Amounts of Boron", *Processing of Stainless Steel,* 1985, pp. 229-239.
[60] Bruemmer, S.M. and Was, G.S. "Microstructural and microchemical mechanisms controlling intergranular stress corrosion cracking in light-water-reactor systems", *Journal of Nuclear Materials,* Vol. 216, Iss. 1, 1994, pp. 348-363.

[61] Jacobs, A.J. "Grain-Boundary Segregation and IGSCC in Cold-Worked Type 304 SS", *Corrosion,* Vol. 46, Iss. 1, 1990, pp. 30-37.
[62] Latanision, R., Kurkela, M., and Lee, F. "The Role of Grain Boundary Chemistry and the Environment on Intergranular Fracture", 1980.
[63] Brossia, C.S. and Kelly, R.G. "Occluded solution chemistry control and the role of alloy sulfur on the initiation of crevice corrosion in type 304ss", *Corrosion Science,* Vol. 40, Iss. 11, 1998, pp. 1851-1871.
[64] Mills, W. "Corrosion Fatigue Behavior for 304 Stainless Steel in 288C Deaerated Water - Retarded Crack Growth at Long Hold Times and Long Rise Times", 2013.
[65] Padilha, A.F., Tavares, C.F., and Martorano, M.A. "Delta Ferrite Formation in Austenitic Stainless Steel Castings", *Materials Science Forum,* Vol. 730-732, Iss. 2013, pp. 733-738.
[66] Brough, L.A. "The effects of processing on delta ferrite measurement", *Journal of Materials for Energy Systems,* Vol. 5, Iss. 1, 1983, pp. 36-42.
[67] Ahmed, I.I., Fonseca, J.Q.d., and Sherry, A.H. "Effect of strain paths and residual delta ferrite on the failure of cold rolled austenitic stainless steels, type 304L", *The Journal of Strain Analysis for Engineering Design,* Vol. 48, Iss. 7, 2013, pp. 410-419.
[68] Miller, B. "Precipitation Behavior of M23C6 Carbides in Type 304 Stainless Steel Containing Delta Ferrite", *Microscopy and Microanalysis,* Vol. 18, Iss. S2, 2012, pp. 1352-1353.
[69] Stickler, R. and Vinckier, A. "Morphology of Grain Boundary Carbides and its Influence on Intergranul Corrosion of 304 Stainless Steel", *Transactions of the American Society for Metals,* Vol. 54, Iss. 1961, pp. 362-380.
[70] Devine, T. "Mechanism of intergranular corrosion and pitting corrosion of austenitic and duplex 308 stainless steel", *Journal of The Electrochemical Society,* Vol. 126, Iss. 3, 1979, pp. 374-385.
[71] Nakao, Y., Nishimoto, K., and Ishizaki, M. "Effects of delta-ferrite on sensitisation of austenitic stainless steel weld metal", *Welding international,* Vol. 6, Iss. 7, 1992, pp. 523-530.
[72] Wilde, B.E. "Influence of Silicon on the Intergranular Corrosion Behavior of 18Cr-8Ni Stainless Steels", *Corrosion,* Vol. 44, Iss. 10, 1988, pp. 699-704.
[73] Wilde, B.E. and Weber, J.E. "Intergranular Stress-Corrosion Resistance of Austenitic Stainless Steels in Water/Oxygen Environment: Accelerated Test Procedure", *British Corrosion Journal,* Vol. 4, Iss. 1, 1969, pp. 42-46.
[74] Sui, G., Charles, E.A., and Congleton, J. "The effect of delta-ferrite content on the stress corrosion cracking of austenitic stainless steels in a sulphate solution", *Corrosion Science,* Vol. 38, Iss. 5, 1996, pp. 687-703.
[75] Kuniya, J., Masaoka, I., and Sasaki, R. "Effect of Cold Work on the Stress Corrosion Cracking of Nonsensitized AISI 304 Stainless Steel in High-Temperature Oxygenated Water", *Corrosion,* Vol. 44, Iss. 1, 1988, pp. 21-28.
[76] Terachi, T., Yamada, T., Chiba, G., and Arioka, K. "Influence of cold work on IGSCC of 316 stainless steel in hydrogenated high-temperature water", NACE Corrosion, 2007, pp. 1-9.
[77] Andresen, P.A., Martin, M.M., and Catlin, W.R. "Effects of yield strength, corrosion potential, composition and stress intensity factor in SCC of stainless steels", NACE Corrosion-04678, Houston, TX, 2004.

[78] Raquet, O., Herms, E., Vaillant, F., Couvant, T., and Boursier, J.M. "SCC of cold-worked austenitic stainless steels in PWR conditions", 12th International Symposium on Environmental Degradation of Materials in Nuclear Power Reactors, Salt Lake City, UT, 2005.

[79] Singh, R. "Influence of cold rolling on sensitization and intergranular stress corrosion cracking of AISI 304 aged at 500 °C", *Journal of Materials Processing Technology*, Vol. 206, Iss. 1–3, 2008, pp. 286-293.

[80] Bose, A. and De, P.K. "An EPR Study on the Influence of Prior Cold Work on the Degree of Sensitization of AISI 304 Stainless Steel", *Corrosion*, Vol. 43, Iss. 10, 1987, pp. 624-631.

[81] Beavers, J.A. and Koch, G.H. "Limitations of the Slow Strain Rate Test Technique", ASTM International,1993.

[82] Andresen, P.L. "SCC testing and data quality considerations", Ninth International Symposium on Environmental Degradation of Materials in Nuclear Power Systems-Water Reactors, 1999.

[83] Logan, H.L. "Film-rupture mechanism of stress corrosion", *Journal of Research of the National Bureau of Standards*, Vol. 48, Iss. 2, 1952, pp. 99-105.

[84] Mears, R.B., Brown, R.H., and Dix, E.H. "A generalized theory of stress corrosion of alloys", Symposium on Stress Corrosion Cracking of Metals, West Conshohocken, PA, 1945.

[85] Vermilyea, D.A. "A Theory for the Propagation of Stress Corrosion Cracks in Metals", *Journal of The Electrochemical Society*, Vol. 119, Iss. 4, 1972, pp. 405-407.

[86] Andresen, P.L. and Peter Ford, F. "Life prediction by mechanistic modeling and system monitoring of environmental cracking of iron and nickel alloys in aqueous systems", *Materials Science and Engineering: A*, Vol. 103, Iss. 1, 1988, pp. 167-184.

[87] Andresen, P.L. and Ford, F.P. "Fundamental modeling of environmental cracking for improved design and lifetime evaluation in BWRs", *International Journal of Pressure Vessels and Piping*, Vol. 59, Iss. 1, 1994, pp. 61-70.

[88] Louthan, M.R., Caskey, G.R., Donovan, J.A., and Rawl, D.E. "Hydrogen embrittlement of metals", *Materials Science and Engineering*, Vol. 10, Iss. 1972, pp. 357-368.

[89] Beachem, C.D. "A new model for hydrogen-assisted cracking (hydrogen "embrittlement")", *Metallurgical Transactions*, Vol. 3, Iss. 2, 1972, pp. 441-455.

[90] Birnbaum, H.K. and Sofronis, P. "Hydrogen-enhanced localized plasticity—a mechanism for hydrogen-related fracture", *Materials Science and Engineering: A*, Vol. 176, Iss. 1, 1994, pp. 191-202.

[91] Andresen, P.L. and Morra, M.M. "IGSCC of non-sensitized stainless steels in high temperature water", *Journal of Nuclear Materials*, Vol. 383, Iss. 1–2, 2008, pp. 97-111.

[92] Lozano-Perez, S., Dohr, J., Meisnar, M., and Kruska, K. "SCC in PWRs: Learning from a Bottom-Up Approach", *Metallurgical and Materials Transactions E*, Vol. 1, Iss. 2, 2014, pp. 194-210.

[93] Lozano-Perez, S., Titchmarsh, J., and Jenkins, M. "TEM characterization of stress corrosion cracks in 304SS", CONFERENCE SERIES-INSTITUTE OF PHYSICS, 2004.

[94] Lozano-Perez, S., Kilburn, M.R., Yamada, T., Terachi, T., English, C.A., and Grovenor, C.R.M. "High-resolution imaging of complex crack chemistry in reactor steels by NanoSIMS", *Journal of Nuclear Materials*, Vol. 374, Iss. 1–2, 2008, pp. 61-68.

[95] Meisnar, M., Moody, M., and Lozano-Perez, S. "Atom probe tomography of stress corrosion crack tips in SUS316 stainless steels", *Corrosion Science,* Vol. 98, Iss. 2015, pp. 661-671.
[96] Lu, Y.H., Peng, Q.J., Sato, T., and Shoji, T. "An ATEM study of oxidation behavior of SCC crack tips in 304L stainless steel in high temperature oxygenated water", *Journal of Nuclear Materials,* Vol. 347, Iss. 1-2, 2005, pp. 52-68.
[97] Huang, Y.Z. and Titchmarsh, J.M. "TEM investigation of intergranular stress corrosion cracking for 316 stainless steel in PWR environment", *Acta Materialia,* Vol. 54, Iss. 3, 2006, pp. 635-641.
[98] Lozano-Perez, S., Yamada, T., Terachi, T., Schröder, M., English, C.A., Smith, G.D.W., Grovenor, C.R.M., and Eyre, B.L. "Multi-scale characterization of stress corrosion cracking of cold-worked stainless steels and the influence of Cr content", *Acta Materialia,* Vol. 57, Iss. 18, 2009, pp. 5361-5381.
[99] Miller, B.D. and Paraventi, D.J. "Evaluation of oxide/metal interfaces formed in type 304/304L stainless steel during environmentally enhanced and retarded fatigue crack growth in deaerated pressurized water using high resolution analytical electron microscopy", 17th international conference on environmental degradation of materials in nuclear power systems - water reactors, 2015, pp. 1-19.
[100] Seifert, H.P., Ritter, S., and Leber, H.J. "Corrosion fatigue crack growth behaviour of austenitic stainless steels under light water reactor conditions", *Corrosion Science,* Vol. 55, Iss. 2012, pp. 61-75.
[101] Chopra, O. "Mechanism and estimation of fatigue crack initiation in austenitic stainless steels in LWR environments", 2002.
[102] Chopra, O.K. and Shack, W.J. "The Effect of LWR Coolant Environments on the Fatigue Life of Reactor Materials", ASME 2006 Pressure Vessels and Piping/ICPVT-11 Conference, 2006.
[103] O'Brien, L.B., Ballinger, R.G., Paraventi, D.J., Yu, L., Maruno, Y., and Stahle, P.W. "The effect of environment, chemistry, and microstructure on the corrosion fatigue behavior of austenitic stainless steels in high temperature water", 17th International Conference on Environmental Degradation of Materials in Nuclear Power Systems – Water Reactors Ottawa, Ontario, Canada 2015.
[104] Chen, Y.Y., Shih, H.C., Wang, L.H., and Oung, J.C. "Fatigue Crack Growth Behavior of Sensitized Type 304 Stainless Steel Under Boiling Water Reactor Conditions", *Corrosion,* Vol. 63, Iss. 11, 2007, pp. 997-1008.
[105] Miller, B.D., Paraventi, D.J., Geller, C.B., and Webb, T.W. "The influence of Hydrogen on Corrosion Fatigue Crack Growth Behavior in Type 304/304L Stainless Steel in Elevated Temperature Deaerated Pressurized Water", International Hydrogen Conference, 2016, pp. 1-11.
[106] Tice, D., Platts, N., Rigby, K., and Stairmand, J. "Influence of temperature and flow rate on the corrosion fatigue crack growth of austenitic stainless steel in a PWR primary coolant environment", 13th International conference on environmental degradation of materials in nuclear power systems, Whistler, British Columbia, Canada, 2007.
[107] West, E.A., Tackes, C., Newsome, G., and Lewis, N. "Influence of Sulfur and Ferrite on SCC and Corrosion Fatigue Behavior of Model Heats of Stainless Steel", 17th International Conference on Environmental Degradation of Materials in Nuclear Power Systems - Water Reactors, Ottawa, Ontario, Canada, 2015.

[108] Radon, J.C., Branco, C.M., and Culver, L.E. "Crack blunting and arrest in corrosion fatigue of mild steel", *International Journal of Fracture,* Vol. 12, Iss. 3, 1976, pp. 467-469.
[109] Gault, B., Moody, M.P., Cairney, J.M., and Ringer, S.P. "Atom probe microscopy", 160, 2012.
[110] Tsong, T. "Measurement of the field evaporation rate of several transition metals", *Journal of Physics F: Metal Physics,* Vol. 8, Iss. 7, 1978, pp. 1349.
[111] Yao, L., Withrow, T., Restrepo, O.D., Windl, W., and Marquis, E.A. "Effects of the local structure dependence of evaporation fields on field evaporation behavior", *Applied Physics Letters,* Vol. 107, Iss. 24, 2015, pp. 241602.
[112] Bas, P., Bostel, A., Deconihout, B., and Blavette, D. "A general protocol for the reconstruction of 3D atom probe data", *Applied Surface Science,* Vol. 87, Iss. 1995, pp. 298-304.
[113] Rolland, N., Vurpillot, F., Duguay, S., Mazumder, B., Speck, J., and Blavette, D. "New Atom Probe Tomography Reconstruction Algorithm for Multilayered Samples: Beyond the Hemispherical Constraint", *Microscopy and microanalysis: the official journal of Microscopy Society of America, Microbeam Analysis Society, Microscopical Society of Canada,* Vol. Iss. 2017, pp. 1.
[114] Marquis, E., Geiser, B., Prosa, T., and Larson, D. "Evolution of tip shape during field evaporation of complex multilayer structures", *Journal of microscopy,* Vol. 241, Iss. 3, 2011, pp. 225-233.
[115] Gault, B., de Geuser, F., Stephenson, L.T., Moody, M.P., Muddle, B.C., and Ringer, S.P. "Estimation of the Reconstruction Parameters for Atom Probe Tomography", *Microscopy and Microanalysis,* Vol. 14, Iss. 4, 2008, pp. 296-305.
[116] Herbig, M., Choi, P., and Raabe, D. "Combining structural and chemical information at the nanometer scale by correlative transmission electron microscopy and atom probe tomography", *Ultramicroscopy,* Vol. 153, Iss. 2015, pp. 32-39.
[117] Baik, S.-I., Yin, X., and Seidman, D.N. "Correlative atom-probe tomography and transmission electron microscope study of a chemical transition in a spinel on an oxidized nickel-based superalloy", *Scripta Materialia,* Vol. 68, Iss. 11, 2013, pp. 909-912.
[118] Haley, D. and Ceguerra, A.V. "3Depict - Visualziation & Analysis for Atom Probe", 2010.
[119] Gault, B., Loi, S.T., Araullo-Peters, V.J., Stephenson, L.T., Moody, M.P., Shrestha, S.L., Marceau, R.K.W., Yao, L., Cairney, J.M., and Ringer, S.P. "Dynamic reconstruction for atom probe tomography", *Ultramicroscopy,* Vol. 111, Iss. 11, 2011, pp. 1619-1624.
[120] De Geuser, F. and Gault, B. "Reflections on the Projection of Ions in Atom Probe Tomography", *Microscopy and Microanalysis,* Vol. Iss. 2017, pp. 1-9.
[121] Miller, M.K. and Forbes, R.G. "Atom probe tomography", *Materials Characterization,* Vol. 60, Iss. 6, 2009, pp. 461-469.
[122] Kirchhofer, R., Teague, M.C., and Gorman, B.P. "Thermal effects on mass and spatial resolution during laser pulse atom probe tomography of cerium oxide", *Journal of Nuclear Materials,* Vol. 436, Iss. 1–3, 2013, pp. 23-28.
[123] Devaraj, A., Colby, R., Hess, W.P., Perea, D.E., and Thevuthasan, S. "Role of Photoexcitation and Field Ionization in the Measurement of Accurate Oxide Stoichiometry by Laser-Assisted Atom Probe Tomography", *The Journal of Physical Chemistry Letters,* Vol. 4, Iss. 6, 2013, pp. 993-998.

[124] Bachhav, M., "Analysis of iron oxides by laser assisted atom probe tomography", Universite de Rouen, Doctor of Philosophy, 2012.
[125] Müller, M., Saxey, D.W., Smith, G.D.W., and Gault, B. "Some aspects of the field evaporation behaviour of GaSb", *Ultramicroscopy,* Vol. 111, Iss. 6, 2011, pp. 487-492.
[126] Blum, I., Zanuttini, D., Rigutti, L., Vurpillot, F., Douady, J., Jacquet, E., Anglade, P.-M., Gervais, B., Vella, A., and Gaillard, A. "Dissociation of Molecular Ions During the DC Field Evaporation ZnO in Atom Probe Tomography", *Microscopy and Microanalysis,* Vol. 22, Iss. S3, 2016, pp. 662-663.
[127] Gault, B., Saxey, D.W., Ashton, M.W., Sinnott, S.B., Chiaramonti, A.N., Moody, M.P., and Schreiber, D.K. "Behavior of molecules and molecular ions near a field emitter", *New Journal of Physics,* Vol. 18, Iss. 3, 2016, pp. 033031.
[128] Saxey, D.W. "Correlated ion analysis and the interpretation of atom probe mass spectra", *Ultramicroscopy,* Vol. 111, Iss. 6, 2011, pp. 473-479.
[129] Meisenkothen, F., Steel, E.B., Prosa, T.J., Henry, K.T., and Prakash Kolli, R. "Effects of detector dead-time on quantitative analyses involving boron and multi-hit detection events in atom probe tomography", *Ultramicroscopy,* Vol. 159, Iss. 1, 2015, pp. 101-11.
[130] Pedrazzini, S., London, A.J., Gault, B., Saxey, D., Speller, S., Grovenor, C.R., Danaie, M., Moody, M.P., Edmondson, P.D., and Bagot, P.A. "Nanoscale Stoichiometric Analysis of a High-Temperature Superconductor by Atom Probe Tomography", *Microscopy and Microanalysis,* Vol. Iss. 2017, pp. 1-11.
[131] Seol, J.-B., Kim, Y.-T., Kim, B.-H., and Park, C.-G. "Novel approach for observing the asymmetrical evolution and the compositional nonuniformity of laser pulsed atom probe tomography of a single ZnO nanowire", *Metals and Materials International,* Vol. 22, Iss. 1, 2016, pp. 34-40.
[132] Seol, J.-B., Kwak, C.-M., Kim, Y.T., and Park, C.-G. "Understanding of the field evaporation of surface modified oxide materials through transmission electron microscopy and atom probe tomography", *Applied Surface Science,* Vol. 368, Iss. 2016, pp. 368-377.
[133] La Fontaine, A., Gault, B., Breen, A., Stephenson, L., Ceguerra, A.V., Yang, L., Dinh Nguyen, T., Zhang, J., Young, D.J., and Cairney, J.M. "Interpreting atom probe data from chromium oxide scales", *Ultramicroscopy,* Vol. 159, Part 2, Iss. 2015, pp. 354-359.
[134] Santhanagopalan, D., Schreiber, D.K., Perea, D.E., Martens, R.L., Janssen, Y., Khalifah, P., and Meng, Y.S. "Effects of laser energy and wavelength on the analysis of LiFePO4 using laser assisted atom probe tomography", *Ultramicroscopy,* Vol. 148, Iss. 2015, pp. 57-66.
[135] Thompson, K., Lawrence, D., Larson, D.J., Olson, J.D., Kelly, T.F., and Gorman, B. "In situ site-specific specimen preparation for atom probe tomography", *Ultramicroscopy,* Vol. 107, Iss. 2–3, 2007, pp. 131-139.
[136] Cissé, S., Laffont, L., Tanguy, B., Lafont, M.-C., and Andrieu, E. "Effect of surface preparation on the corrosion of austenitic stainless steel 304L in high temperature steam and simulated PWR primary water", *Corrosion Science,* Vol. 56, Iss. 2012, pp. 209-216.
[137] Lozano-Perez, S., Kruska, K., Iyengar, I., Terachi, T., and Yamada, T. "The role of cold work and applied stress on surface oxidation of 304 stainless steel", *Corrosion Science,* Vol. 56, Iss. 0, 2012, pp. 78-85.

[138] Kuang, W., Wu, X., Han, E.-H., and Ruan, L. "Effect of nickel ion from autoclave material on oxidation behaviour of 304 stainless steel in oxygenated high temperature water", *Corrosion Science,* Vol. 53, Iss. 3, 2011, pp. 1107-1114.
[139] Ghosh, S., Kumar, M.K., and Kain, V. "High temperature oxidation behavior of AISI 304L stainless steel—Effect of surface working operations", *Applied Surface Science,* Vol. 264, Iss. 2013, pp. 312-319.
[140] Hellman, O.C., Vandenbroucke, J.A., Rüsing, J., Isheim, D., and Seidman, D.N. "Analysis of three-dimensional atom-probe data by the proximity histogram", *Microscopy and Microanalysis,* Vol. 6, Iss. 05, 2000, pp. 437-444.
[141] Allen, G.C., Dyke, J.M., Harris, S.J., and Morris, A. "A surface study of the oxidation of type 304L stainless steel at 600 K in air", *Oxidation of Metals,* Vol. 29, Iss. 5-6, 1988, pp. 391-408.
[142] Singh, R., Chattoraj, I., Kumar, A., Ravikumar, B., and Dey, P.K. "The effects of cold working on sensitization and intergranular corrosion behavior of AISI 304 stainless steel", *Metallurgical and Materials Transactions A,* Vol. 34, Iss. 11, 2003, pp. 2441-2447.
[143] Caplan, D. and Cohen, M. "Effect of cold work on the oxidation of iron from 400–650 °C", *Corrosion Science,* Vol. 6, Iss. 7, 1966, pp. 321-335.
[144] Hermas, A., Ogura, K., and Adachi, T. "Accumulation of copper layer on a surface in the anodic polarization of stainless steel containing Cu at different temperatures", *Electrochimica acta,* Vol. 40, Iss. 7, 1995, pp. 837-844.
[145] Kruska, K., Lozano-Perez, S., Saxey, D.W., Terachi, T., Yamada, T., and Smith, G.D.W. "Nanoscale characterisation of grain boundary oxidation in cold-worked stainless steels", *Corrosion Science,* Vol. 63, Iss. 0, 2012, pp. 225-233.
[146] Wagner, C. "Diffusion and high temperature oxidation of metals", *Atom movements,* Vol. Iss. 1951, pp. 153-173.
[147] Perkins, R., Padgett, R., and Tunali, N. "Tracer diffusion of59Fe and51Cr in Fe-17 Wt Pet Cr-12 Wt Pet Ni austenitic alloy", *Metallurgical transactions,* Vol. 4, Iss. 11, 1973, pp. 2535-2540.
[148] Mizouchi, M., Yamazaki, Y., Iijima, Y., and Arioka, K. "Low temperature grain boundary diffusion of chromium in SUS316 and 316L stainless steels", *Materials transactions,* Vol. 45, Iss. 10, 2004, pp. 2945-2950.
[149] Perkins, R. "Tracer diffusion of63Ni in Fe-17 wt pct Cr-12 wt pct Ni", *Metallurgical Transactions,* Vol. 4, Iss. 7, 1973, pp. 1665-1669.
[150] Johns, E.C. and Miller, B.D. "Effects of boron and mechanical processing on intergranular attack in dual certified type 304 stainless steel determined using DL-EPR", 16th International Conference on Environmental Degradation of Materials in Nuclear Power Systems - Water Reactors, Asheville, NC, 2013.
[151] Miller, B.D. "Personal communication", 2016

[152] Meisenkothen, F., Prosa, T.J., Steel, E.B., and Kolli, R.P. "The role of multi-hit detection events on the accurate measurement off boron in atom probe tomography", *Microsc. Microanal,* Vol. 20, Iss. Supplement 3, 2014, pp. 1962-1963.
[153] Meisnar, M., Vilalta-Clemente, A., Gholinia, A., Moody, M., Wilkinson, A.J., Huin, N., and Lozano-Perez, S. "Using transmission Kikuchi diffraction to study intergranular

stress corrosion cracking in type 316 stainless steels", *Micron,* Vol. 75, Iss. 1, 2015, pp. 1-10.
[154] Sugiyama, M. and Sigesato, G. "A review of focused ion beam technology and its applications in transmission electron microscopy", *Journal of Electron Microscopy,* Vol. 53, Iss. 5, 2004, pp. 527-536.
[155] Creager, M. and Paris, P.C. "Elastic field equations for blunt cracks with reference to stress corrosion cracking", *International Journal of Fracture Mechanics,* Vol. 3, Iss. 4, 1967, pp. 247-252.
[156] Gangloff, R.P. and Somerday, B.P. "Gaseous hydrogen emrbittlement of materials in energy technologies", 1, 2012.
[157] Michler, T., Naumann, J., Hock, M., Berreth, K., Balogh, M.P., and Sattler, E. "Microstructural properties controlling hydrogen environment embrittlement of cold worked 316 type austenitic stainless steels", *Materials Science and Engineering: A,* Vol. 628, Iss. 2015, pp. 252-261.
[158] Sofronis, P. and Birnbaum, H.K. "Mechanics of the hydrogen-dislocation-impurity interactions—I. Increasing shear modulus", *Journal of the Mechanics and Physics of Solids,* Vol. 43, Iss. 1, 1995, pp. 49-90.
[159] Gemma, R., Al-Kassab, T., Kirchheim, R., and Pundt, A. "APT analyses of deuterium-loaded Fe/V multi-layered films", *Ultramicroscopy,* Vol. 109, Iss. 5, 2009, pp. 631-636.
[160] Takahashi, J., Kawakami, K., Kobayashi, Y., and Tarui, T. "The first direct observation of hydrogen trapping sites in TiC precipitation-hardening steel through atom probe tomography", *Scripta Materialia,* Vol. 63, Iss. 3, 2010, pp. 261-264.
[161] Takamizawa, H., Hoshi, K., Shimizu, Y., Yano, F., Inoue, K., Nagata, S., Shikama, T., and Nagai, Y. "Three-dimensional characterization of deuterium implanted in silicon using atom probe tomography", *Applied Physics Express,* Vol. 6, Iss. 6, 2013, pp. 066602.
[162] Karnesky Jr, R.A., Bartlet, N., Huang, D., Teslich, N., and Kumar, M. "Imaging and quantification of hydrogen isotope trapping", *Sandia National Laboratories,* 2012.
[163] Haley, D., Bagot, P.A., and Moody, M.P. "Atom Probe Analysis of Ex Situ Gas-Charged Stable Hydrides", *Microscopy and Microanalysis,* Vol. Iss. 2017, pp. 1-7.
[164] Haley, D., Merzlikin, S.V., Choi, P., and Raabe, D. "Atom probe tomography observation of hydrogen in high-Mn steel and silver charged via an electrolytic route", *International Journal of Hydrogen Energy,* Vol. 39, Iss. 23, 2014, pp. 12221-12229.
[165] Berkowitz, B. and Heubaum, F. "Dislocation Transport of Hydrogen in Steel", *Atomistics of Fracture,* 1983, pp. 823-827.
[166] Kurkela, M., Frankel, G.S., Latanision, R.M., Suresh, S., and Ritchie, R.O. "Influence of plastic deformation on hydrogen transport in 2 14 Cr-1Mo steel", *Scripta Metallurgica,* Vol. 16, Iss. 4, 1982, pp. 455-459.
[167] Hayles, M., Stokes, D., Phifer, D., and Findlay, K. "A technique for improved focused ion beam milling of cryo-prepared life science specimens", *Journal of microscopy,* Vol. 226, Iss. 3, 2007, pp. 263-269.
[168] Kruska, K., Lozano-Perez, S., Saxey, D.W., Terachi, T., Yamada, T., and Smith, G.D.W. "3D Atom-Probe Characterization of Stress and Cold-Work in Stress Corrosion Cracking of 304 Stainless Steel", 15th International Conference on Environmental Degradation of Materials in Nuclear Power Systems-Water Reactors, 2012.

[169] Louthan, M.R. and Derrick, R.G. "Hydrogen transport in austenitic stainless steel", *Corrosion Science*, Vol. 15, Iss. 6, 1975, pp. 565-577.
[170] Parmenter, C.D., Fay, M.W., Hartfield, C., and Eltaher, H.M. "Making the practically impossible "Merely difficult"—Cryogenic FIB lift-out for "Damage free" soft matter imaging", *Microscopy research and technique*, Vol. 79, Iss. 4, 2016, pp. 298-303.
[171] Rubino, S., Akhtar, S., Melin, P., Searle, A., Spellward, P., and Leifer, K. "A site-specific focused-ion-beam lift-out method for cryo Transmission Electron Microscopy", *Journal of structural biology*, Vol. 180, Iss. 3, 2012, pp. 572-576.
[172] Antoniou, N., Graham, A., Hartfield, C., and Amador, G. "Failure analysis of electronic material using cryogenic FIB-SEM", Conf. Proc. 38th Int. Symp. Testing and Failure Analysis, Phoenix, AZ, 2012.
[173] Kelly, T.F., Nishikawa, O., Panitz, J.A., and Prosa, T.J. "Prospects for nanobiology with atom-probe tomography", *MRS bulletin*, Vol. 34, Iss. 10, 2009, pp. 744-750.
[174] Hugo, R. and Hoagland, R. "In-situ TEM observation of aluminum embrittlement by liquid gallium", *Scripta materialia*, Vol. 38, Iss. 3, 1998, pp. 523-529.
[175] Tang, F., Gianola, D.S., Moody, M.P., Hemker, K.J., and Cairney, J.M. "Observations of grain boundary impurities in nanocrystalline Al and their influence on microstructural stability and mechanical behaviour", *Acta Materialia*, Vol. 60, Iss. 3, 2012, pp. 1038-1047.
[176] Zeigler, J.F. "Stopping Range of Ions in Matter", www.srim.org, 1978.
[177] Tang, F., Moody, M.P., Martin, T.L., Bagot, P.A., Kappers, M.J., and Oliver, R.A. "Practical issues for atom probe tomography analysis of III-nitride semiconductor materials", *Microscopy and Microanalysis*, Vol. 21, Iss. 03, 2015, pp. 544-556.
[178] Betz, G., Wehner, G., Toth, L., and Joshi, A. "Composition-vs-depth profiles obtained with Auger electron spectroscopy of air-oxidized stainless-steel surfaces", *Journal of Applied Physics*, Vol. 45, Iss. 12, 1974, pp. 5312-5316.
[179] Baer, D.R. "Protective and non-protective oxide formation on 304 stainless steel", *Applications of Surface Science*, Vol. 7, Iss. 1, 1981, pp. 69-82.
[180] Tanabe, T. and Imoto, S. "Surface oxidation of type 316 stainless steel", *Transactions of the Japan Institute of Metals*, Vol. 20, Iss. 9, 1979, pp. 507-515.